Astrophysical impacts on habitable planetary systems

Kokaia, Giorgi

2020

Astrophysical impacts on habitable planetary systems

Astrophysical impacts on habitable planetary systems

Giorgi Kokaia

LUND
UNIVERSITY

Thesis for the degree of Doctor of Philosophy
Thesis advisors: Prof. Melvyn B. Davies, Dr. Alexander J. Mustill
Faculty opponent: Dr. Alessandro Sozzetti

To be presented, with the permission of the Faculty of Science of Lund University, for public criticism in the Lundmark lecture hall (Lundmarksalen) at the Department of Astronomy and Theoretical Physics on Friday, 4th of December 2020 at 13:00.

LUND UNIVERSITY
Dept. of Astronomy & Theoretical Physics
Lund Observatory
Box 43
SE-221 00, Lund, Sweden

Document name
DOCTORAL DISSERTATION

Date of issue
04 December 2020

Author(s)
Giorgi Kokaia

Sponsoring organization

Title and subtitle

Astrophysical impacts on habitable planetary systems

Abstract

Finding life on a planet other than the Earth would easily be one of the greatest discoveries of all time, particularly so if it is found outside our Solar System. To do so, we must understand the conditions required for life to emerge and develop. Whilst an enormous amount of research has gone into understanding the requirements for life on Earth to have spontaneously arisen and then evolved, much less focus has been put on how factors outside the Earth and even outside the Solar System may affect the so-called habitability of the Earth.

This thesis summarizes three papers in which I have studied different astrophysical effects that can impact the habitability of planets.

In Paper I, I investigate how the habitability of planets is affected by the Galactic orbit of their host star by considering how often they encounter giant molecular clouds. Paper I shows that for the Sun these encounters and potential extinction events due to core-collapse supernovae happen roughly once per billion years.

In Paper II, I consider how planet-planet scattering between gas giants following an orbital instability can wipe out habitable planets in a system. Paper II shows that in any exoplanet system where there is an observed close-in eccentric giant, it will be very unlikely to find any habitable planet.

In Paper III, I examine how a system can be made uninhabitable if the host star picks up an additional planet during a close encounter with another star in its birth cluster. Paper III shows that this can happen either by the new planet ending up on an orbit that destabilizes the existing planets in the system, or more interestingly, by significantly increasing the impact rate of large asteroids for billions of years.

Key words
astrobiology; Sun: general; planetary systems; planets and satellites: dynamical evolution and stability

Classification system and/or index terms (if any)

Supplementary bibliographical information

Language
English

ISSN and key title

ISBN
978-91-7895-690-6 (print)
978-91-7895-691-3 (pdf)

Recipient's notes

Number of pages
145

Price

Security classification

Signature

Date
2020-10-23

Astrophysical impacts on habitable planetary systems

Giorgi Kokaia

LUND
UNIVERSITY

Faculty Opponent

Dr. Alessandro Sozzetti
University of Turin
Turin, Italy

Evaluation Committee

Prof. Anja Andersen
University of Copenhagen
Copenhagen, Denmark

Prof. Markus Janson
Stockholm University
Stockholm, Sweden

Dr. Grant Kennedy
University of Warwick
Coventry, United Kingdom

Cover – Image of NGC1333: a molecular cloud part of the Perseus complex, within it are embedded several young star clusters. Taken with a QSI 660wsg-8 camera mounted on a Takahashi FSQ106EDXIII refractor telescope from Abastumani, Georgia.
Image credit: Reproduced with permission of David Dvali
https://www.facebook.com/geoastro.net/

Faculty of Science, Department of Astronomy and Theoretical Physics
ISBN: 978-91-7895-690-6 (print)
ISBN: 978-91-7895-691-3 (pdf)

Printed in Sweden by Media-Tryck, Lund University, Lund 2020

Dedicated to my wife, Noemi Schaffer
For being supportive and caring every evening and weekend I spent finishing this thesis

Contents

List of publications

The following papers have been published as a result of my PhD work:

I **Stellar encounters with Giant Molecular Clouds**

G. Kokaia, M.B. Davies (2019)
Monthly Notices of the Royal Astronomical Society, Volume 498, Issue 1, p.5165-5180

II **Resilient habitability of nearby exoplanet systems**
G. Kokaia, M.B. Davies, A.J. Mustill (2020)
Monthly Notices of the Royal Astronomical Society, Volume 492, Issue 1, p. 352-368

III **Effects of capturing a wide-orbit planet on planetary systems: system stability and Habitable Zone bombardment rates**

G. Kokaia, M.B. Davies, A.J. Mustill (2020)
Submitted to Monthly Notices of the Royal Astronomical Society

Not included in thesis:

IV **Oumuamuas passing through molecular clouds**
S. Pfalzner, M.B. Davies, **G. Kokaia**, M. Bannister (2020)
Accepted, arXiv:2009.08773

Popular summary

In this thesis the science in three of my published papers is presented. Each of the papers touches upon how astrophysical different phenomena can affect life on habitable planets in the Galaxy, where each paper addresses the question at a different scale. Going from largest to smallest, the work can be summarized as follows:

On a Galactic scale, I investigated how often stars on different orbits cross through the spiral arms of the Galaxy where they can encounter large and dense gas clouds and supernovae. I found that its a very sensitive function of how old the star is and where in the Galaxy the star is located. With a star like the Sun encountering these things roughly once per billion years whereas younger stars located closer to the center of the Galaxy can have encounter rates more than 100 times larger.

On the scale of stellar clusters, I examined the effects on habitable planets in a system whose host star picks up an additional planet during a close encounter with another star in its birth cluster. I found that in 60% of cases it will have a significantly negative effect on the habitable planet, either by completely destroying it through dynamical interactions or by significantly enhancing the impact rate of large bodies on the planet.

On the scale of a planetary system, I examined systems known to host gas giants and considered how dynamical instabilities and scattering between the observed giant planet and hitherto undetected / previously ejected gas giants in the systems' past would have affected a planet in the habitable zone. I found that in most known systems a potential instability in the past would have wiped out a large fraction of planets in the habitable zone; in a small subset of systems this is not the case and they are presented as good candidates for future observations in the paper.

Populärvetenskaplig sammanfattning

I den här avhandlingen är forskningen utförd i tre av mina publicerade artiklar beskriven. Var och en av artiklarna berör hur olika astrofysiska fenomen kan påverka liv på beboliga planeter i Galaxen. Tre olika problem, på tre olika skalor behandlas i respektive artikel. Från störst till minst skala kan arbetet summeras så här:

På Galaktisk skala undersökte jag hur ofta stjärnors omloppsbanor tar dem genom Galaxens spiralarmar där de kan stöta på stora, tjocka gasmoln samt supernovor. Hur ofta detta sker visade jag vara en väldigt känslig funktion av stjärnans plats i Galaxen samt dess ålder. En stjärna som Solen kommer efter en miljard år ha drabbats av detta cirka en gång medan andra, yngre stjärnor som befinner sig något närmre Galaxens mittpunkt kan göra det mer än 100 gånger.

På stjärnhops-nivå undersökte jag effekterna av att ett stjärn-system stjäl en planet när den far förbi en annan stjärna med planeter i sitt födelsekluster. Där fann jag att i 60% av fallen så kommer det ha en väldigt negativ inverkan, där det antingen helt förstör beboliga planeter i systemet eller leder till en konstant bombardering av asteroider.

På skalan av ett planet-system så tittade jag på system med kända gas-jättar och undersökte hur starka gravitationella interaktioner mellan gas-jätterna i systemens förflutna kan ha förstört beboliga planeter som fanns där en gång i tiden. Där visade jag att det troligtvis är fallet för de flesta system men samtidigt presenterade jag ett par goda kandidater där detta troligtvis inte har hänt.

Acknowledgements

Before anything else, I have to acknowledge my parents, brother and extended family living in Sweden. If they had not nurtured my curiosity from a young age I would never have become a scientist, and I find this a remarkable feat as I know how annoying a little know-it-all of a child that I was.

My supervisor, Melvyn B. Davies. First for the obvious scientific guidance and training he gave me and although I am outside of academia as I type this I will always look back to his mentorship moving forward. The second, not so obvious acknowledgement is for a lecture he gave in 2010 titled "Extreme Astrophysics". Listening to this lecture is what made me make the switch from theoretical physics to astronomy.

My co-supervisor Alexander Mustill is hard to describe with anything short of *awesome!* On more occasions than I care to admit did he swiftly solve a problem I was stuck on or made something incomprehensible easily understandable and my biggest regret as a PhD-student might be that he wasn't more involved in my first project.

To every PhD student with whom I shared time in the trenches, thank you! Be it the people I started out with like Simona Pirani and Matthäus Schulik or the friends I met along the way like Eric Andersson or Daniel Mikkola, you are all stars. Of course, Dr. Schulik gets a special thanks as we shared an office for four years and in that time we shared many a late night with great discussions, laughs and sometimes [often] curses at our non-functional computers or code.

And of course, my wife Noemi Schaffer and son Jason Kokaia. There is so much to thank them for but I'll leave it at this: there is no way I could have finished this thesis whilst working a full-time job in the midst of a pandemic if it wasn't for them. And, our beloved dog Ted who always provided a head to scratch when I was stressing out.

Part I

Research context

Preface

The main question this thesis deals with is: how do astrophysical phenomena affect the habitability of planetary systems? I have examined the effects of the host stars' motion through the Galaxy, the effects of a gravitational instability in the outer planets also orbiting the host star and the effects of the host star picking up a planet from another star in its birth cluster.

This thesis summarizes the work which has been published in three papers, here follows brief descriptions of each paper to give the reader an overview of the thesis.

1. *Paper I: Stellar encounters with Giant Molecular Clouds* – In this paper I examine how often stars on different orbits throughout our Galaxy encounter giant molecular clouds (GMCs). We were interested in determining the GMC encounter rate for two reasons. First of all the GMCs act as a proxy for the locations of the spiral arms, therefore by determining how often stars encounter GMCs we can actually also determine how often stars cross through the spiral arms. Given that arguments have been made linking spiral arm crossings to mass extinctions on Earth our work allows us to address this question. Second, we show and argue throughout the paper that crossing through a GMC can be very detrimental and potentially cause a mass-extinction for a habitable planet orbiting the star; both by the significant risk of nearby supernovae and the accretion of gas during a GMC passage. In the paper we show that the GMC encounter rate depends very strongly on the Galactocentric radius (R) and the velocity away from the mid-plane ($V_{\rm z}$ – the velocity in the $|z|$-direction at $z = 0$). We show that young stars ($V_{\rm z}$ of 2-3 km/s) at relatively small R (~ 5 kpc) will encounter hundreds of GMCs per Gyr whereas a star on an orbit similar to that of the Sun ($R \sim 8$ kpc, $V_{\rm z} \sim 9$ km/s) will have one or two encounters per Gyr; with even more distant and older stars having vanishingly small encounter rates. As for the Sun and the Earth it means that it is quite unlikely for any of the mass extinctions observed in the geological archive (the oldest of which is $\sim$500 Myr old) to be the consequence of a GMC passage. However, recent studies have shown that the Sun might have originated at ~ 5 kpc, rather than its current location (Schönrich & Binney 2009; Frankel et al. 2018). At that location in the Galaxy it is inevitable that the Sun would have had GMC encounters that would have had a noticeable effect on the Earth, whether they had a significant effect on the evolution of the

life on Earth or caused any of the known mass extinctions will be wholly dependant on when the migration occurred. Therefore, any study that further elucidates the dynamical history of the Sun will also shed light on the development of life on Earth.

2. *Paper II: Resilient habitability of nearby exoplanet systems* – The core idea of this paper was to look at stellar systems known to host giant planets and simulate them in order to constrain the likelihood of finding additional, smaller, planets in the system's habitable zone (HZ) and to suggest them as candidates for future observational studies that will look for these types of planets. We look at systems with known giant planets because there appears to be a correlation in the occurrence rates of gas giants and smaller rocky planets, but also because systems with known giant planets are the ones in which the existence of habitable planets *can* be constrained. We determine which systems are the most suitable for observations by simulating the gas giant in its current orbit and by doing a set of simulations corresponding to potential dynamical histories of the system. We postulate and show it to be reasonable that the eccentricity of all of the observed giant planets arose as a consequence of planet–planet scattering and the dynamical past of the systems that we simulate are scattering simulations of its possible initial state that produces a system consistent with the system in its present state. We call the fraction of orbits in the HZ that survive the scattering phase the **resilient habitability** (as defined in Carrera et al. 2016) and find a very strong connection between the pericentre of the system and its resilient habitability. If the giant planet is close to the HZ due to having a small semi-major axis, any type of scattering process will have a significant effect on the stability of orbits in the HZ. Whereas if the pericentre is close to the HZ due to the planet having a large eccentricity it means that the scattering process was violent and that the ejected planet had a large mass which much more easily destabilizes orbits in the HZ as it is being ejected. Taking these things into account we produce a list of systems most suitable for future observations.

3. *Paper III: Consequences for terrestrial planets following planet capture* – In this paper we take a closer look at what happens to planets in a planetary system that encounters another star and captures an additional planet, which has been shown to be possible in the dense birth environments of stars (Malm-

berg et al. 2011; Li et al. 2019). We consider the potential consequences for a system hosting both an Earth-like planet in the HZ as well as a more distant, Jupiter-mass giant planet in the event that another Jupiter-mass planet is captured into the system. The scenarios we examine are mostly ones in which the captured planet ends up on a distant orbit and cannot directly interact with the planets already in the system as such orbits would either directly destabilise the entire system, or lead to a scenario identical to that of Paper II. In the scenarios that we do look at the captured planet affects the internal planets by destabilising asteroids in the outer system and sending them inwards on trajectories that can collide with the planets. We find that in $\sim$40% of cases when a Jupiter-mass planet is captured, the planet in the HZ ends up being destroyed and of the remaining 60% of encounters the outcome is either an intense bombardment of asteroids lasting on the order of tens to a few hundred Myr or a slow and steady inflow of asteroids that can last for more than a Gyr. This slow and steady inflow would result in an impact rate an order of magnitude larger than what is seen on Earth and this constant barrage of large impacts would be devastating to complex life on a planet in the HZ of such a system.

Given that the thesis contains two papers on planetary systems and one on the Galaxy, the thesis has been structured accordingly. Chapter 1 discusses planetary systems and relevant background for papers II and III. Chapters 2 and 3 then summarizes each paper, respectively. Chapter 4 is structured like a long summary of Paper I. Since the paper touches on a wide range of different fields, interspersing the relevant theoretical background amongst what is in the paper itself results in a much more cohesive narrative.

NOTE: Throughout the thesis there are grey boxes like the one below. These boxes indicate that the specifics of a simulation is being discussed.

Simulation box

Chapter 1

Planetary systems

1.1 Habitability

Both Paper II and Paper III concern the habitability of planets, therefore it stands to reason that we start off by defining what we mean by a habitable planet. The only planet that we know to host life is the Earth, which gives us a natural template for our definition. We use a common and convenient definition used throughout astronomy (e.g. Kasting et al. 1993): a roughly **Earth-sized planet** orbiting a star at such a distance that the planet can have **liquid water on its surface**.

This might at first seem like a very broad definition, but it is in fact the opposite. Just looking at the Earth we find life in the most unexpected places, from fungi growing in extremely deep, hyper-acidic mine-shafts to anhydrobiotic shrimp living in lakes of brine (Rothschild & Mancinelli 2001). To put it in the words of Dr. Ian Malcolm depicted by Jeff Goldblum in Jurassic Park (1993): "Life... uh... finds a way". Then, considering the vastness of the cosmos it is nearly inevitable that there will be forms of life that we can't even imagine.

But we need to somehow limit the parameter space in which we work. Whilst the presence of water might be a narrow definition, there are at least two very good reasons to use it. Firstly, experiments have been able to create conditions in which the building blocks of life (such as RNA) form spontaneously. Although it is unclear how life arose following the formation of its components, the processes all appear to take place in water (Dyson 1999; Patel et al. 2015). Second, water-ice (specifically, I_{h}-ice) has a lower density than liquid water, except at extremely high

pressures. The solid state of a substance having a lower density than it has a liquid is quite rare, but water does and it has a very important implication. In the winter when it freezes, the sheets of ice form on top of the water rather than freezing the ocean bottom up and creating an ice ball. This means that whatever life forms in the lakes or oceans of a planet can survive when it gets cold.

1.1.1 The Habitable Zone

With the requirement of having liquid water on the surface of the planet we can now for each star define a habitable zone. The habitable zone of a star is the separation at which a planet with a realistic atmosphere has a surface temperature such that there is liquid water on the surface. The atmospheric conditions are of critical importance because of greenhouse effects, which can drastically affect the temperature of the planet through the trapping of heat (first quantified by Svante Arrenhius in 1867 – Rodhe et al. 1997). This explains how Venus can be warmer than Mercury even though it is roughly twice the separation from the Sun and therefore only receives $\sim 1/4$ of the flux (Bottema et al. 1965; Sagan & Pollack 1967).

The location and width of the habitable zone is set by the luminosity and surface temperature of the star along with the atmospheric conditions of the planet. The habitable zone is mostly discussed in Paper II and we utilize one of the most commonly used models, that of Kopparapu et al. (2014) to define it. The edges of the habitable zone are determined using the equation below:

$$r = \left(\frac{L/L_{\odot}}{S_{\text{eff}}} \right)^{0.5} \text{ au} \tag{1.1}$$

where $L_{\odot}$ is the Solar luminosity and

$$S_{\text{eff}} = S_{\text{eff}\odot} + aT_{\star} + bT_{\star}^2 + cT_{\star}^3 + dT_{\star}^4 \tag{1.2}$$

is a measure of the flux received by the planet with $T_{\star} = T - T_{\odot}$ ($T_{\odot} = 5780\ K$), i.e. the difference between the surface temperature of a star and the Sun. The reason for the many different powers of the temperature is to capture the fact that different types of planetary atmospheres will be heated differently by different types of stars, with the different atmospheres defined by the parameters (a, b, c and d). Table 1.1 shows the values which give the widest possible habitable zone.

Table 1.1: Parameters used in equation 1.2 for determining the boundaries of the habitable zone as given by Kopparapu et al. (2014)

	Inner edge	Outer edge
Parameter	Runaway Greenhouse	Maximum Greenhouse
$S_{\text{eff}\odot}$	1.107	0.356
a	1.332×10^{-4}	6.171×10^{-5}
b	1.58×10^{-8}	1.698×10^{-9}
c	-8.308×10^{-12}	-3.198×10^{-12}
d	-1.931×10^{-15}	-5.575×10^{-16}

We show the habitable zone as a function of zero age main sequence stellar mass in figure 1.1, i.e. we show the habitable zone for a star that has not undergone any evolution and has the surface temperature and luminosity it starts its main sequence with. The inner edge of the habitable zone is set using the model parameters for runaway greenhouse habitability, the limit at which the temperature of the planet, under any realistic atmospheric conditions, inevitably becomes too high. The outer edge is set using the maximum greenhouse parameters, which is the limit at which an atmosphere optimally constructed to maximise the greenhouse effect can no longer prevent all the water from freezing.

As a star evolves through its main sequence its luminosity will go up and its surface temperature will change (Tout et al. 1996) which will shift the location of the habitable zone. However, most planets formed near the center of the habitable zone will remain within it throughout the main sequence of most stars. This means that unless something either affects the atmosphere of the planet or changes its orbit it will remain habitable during this time.

1.2 Exoplanet observations

At present, the detection of exoplanets is largely limited to two types of planets: gas giants and super-Earths. The gas giants are planets between roughly 0.1 and 10 Jupiter-masses found most often at separations between 1 and 10 au; although a subset of them, Hot Jupiters, are found very close to their hosts at separations of less than 0.1 au. Super-Earths are primarily rocky planets ranging in masses from a few to tens of Earth-masses (where the more massive ones are often called sub-Neptunes as they have been shown to have gas envelopes) and with most of

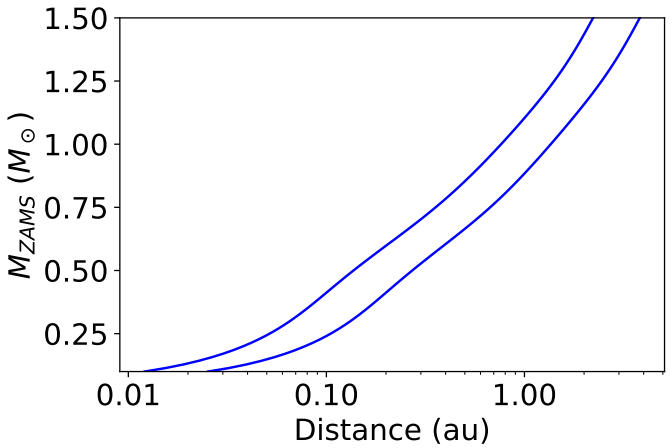

Figure 1.1: The extent of the habitable zone using the zero age main sequence (Tout et al. 1996) parameters for stars of a given mass and Solar metallicity. The edges are set by using equation 1.1 with the inner edge set using the "Runaway Greenhouse" parameters from table 1.1 and the outer edge set using "Maximum Greenhouse".

them found close to their hosts between 0.1 and 0.7 au.

The distant gas giants are detected using the so-called radial velocity method. The radial velocity method relies on the Doppler effect, i.e. the shift in the wavelength of the stellar spectrum due to a relative velocity between the star and observer. As the star orbits its common centre of mass with the planets in the system the motion can be detected and the existence of an exoplanet inferred if the velocity is high enough to produce a signal that is both measurable and seen as periodic. The velocity and therefore signal strength increases with planetary mass and decreases with orbital separation, meaning that the more massive and the closer in a planet is, the easier it should be to detect. However, given the mass of these gas giants they are typically not at separations large enough for the signal to get too small to be detected. In fact, the orbital timescale is usually the limiting factor for detecting distant giants; as one has to observe at least one full orbit to confirm that the observed signal is from an exoplanet.

Hot Jupiters and super-Earths are primarily detected using the so-called transit

method, in which one looks for periodic dips in stellar luminosity as the planet passes between star and observer, blocking out a fraction of the light. The probability of a planet's orbit crossing the stellar disk with respect to the observer scales as the stellar radius over the semi-major axis of the planet, and the change in brightness scales as the square of the star–planet radius ratio. Taking the Sun and the Earth as an example we see that it gives a $\sim 0.5\%$ probability of producing a $\sim 10^{-4}$ change in brightness. So it comes as no surprise that the transit method heavily favors detecting large planets at small separations from their host stars.

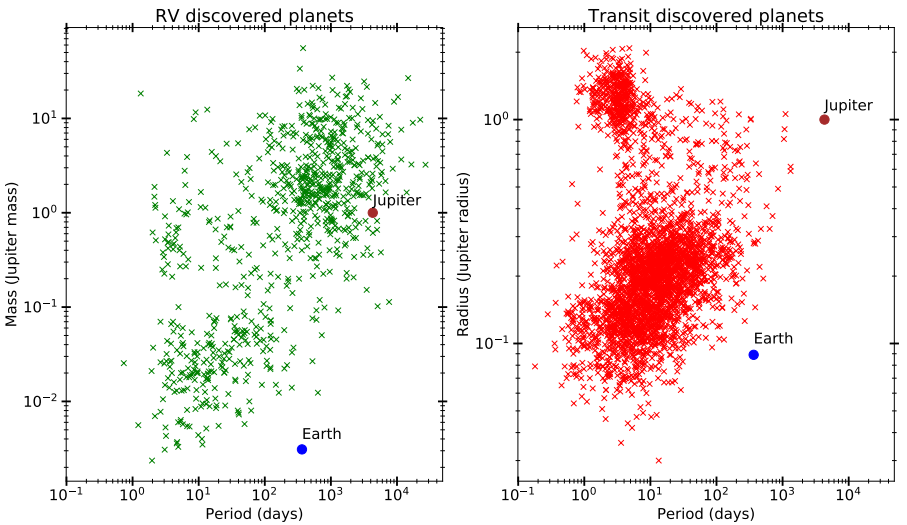

Figure 1.2: The left panel shows all[1] detected exoplanets through the transit method, which is why they all have an estimated radius. The right hand panel shows all[1] exoplanets detected through the RV-method, which results in the exoplanet also having a mass ($M \sin i$) estimate.
[1] as of Oct 8th 2020

Figure 1.2 shows all the detected exoplanets that have been found through transits (left) or through the RV-method (right). The figure clearly shows the three distinct populations described in the previous paragraphs but given the fact that the transit probability of the distant gas giants is so small there are very few of them that have determined radii. Conversely, many of the transit detected planets give such weak RV signals or around too faint stars (primarily the *Kepler* systems) to have had their mass determined.

What is also apparent from the figure is that there are no detected planets that have the same orbital period and radius/mass as the Earth. Even though the distribution of planets detected through transits grazes the parameter space for an Earth-like planet, the possibility of detecting one is distant as such transits can only be captured by space telescopes as detecting such small variations ($\sim 10^{-4}$) from the surface is prohibited by the atmosphere. The first detection of an Earth-like planet through transits (around a Sun-like star) will probably be made by PLATO. PLATO is a space telescope that will look for planetary transit signals from stars just like *Kepler* did, however unlike *Kepler* rather than observing a single small patch it will observe multiple much larger fields of view (Rauer et al. 2014). The first detection of an Earth-like planet will therefore likely not occur for another decade as PLATO is planned to be launched in 2026 and any such detection is bound to happen after the telescope has been observing for quite some time. However, there are already instruments that when at full capacity should be able to detect Earth-like planets through RV, namely the spectrographs ESPRESSO mounted on the VLT (Pepe et al. 2010; Leite et al. 2018) and HARPS-3 (i.e. the "Terra-Hunting experiment" Thompson et al. 2016) on the 2.5m Issac Newton telescope on La Palma. On the same timescale as PLATO, the E-ELT should be finished and using an instrument such as HIRES (Marconi et al. 2016) it will certainly have the capacity of finding Earth-like planets; as it has been shown to be able to reach sensitivities of $\lesssim 4$ cm/s (Milaković et al. 2020). It should be noted that the fact that these RV-instruments have the capacity of detecting these planets doesn't mean that they actually will do so: the RV-signal from an Earth-like star is on the same order of magnitude (~ 10 cm/s) as the convective flows on the stellar surface and distinguishing the signal from the noise will be nearly as hard as measuring the signal itself (see e.g. Cegla 2019).

1.3 Planetary dynamics

The orbits of planets can easily be considered the most well-known problem in all of astrophysics. Johannes Kepler was the first person to give it a mathematical description. Not long after that Isaac Newton published his *Principa Mathematica* in which he laid the foundations for calculus and classical mechanics in order to solve this problem. And he did solve it, at least in part as he presented the solution to the two body problem. The solution is a full analytical description of the orbits

of two bodies interacting with each other gravitationally. General analytical solutions for more than two massive bodies have not been found despite considerable effort having gone into it over the past 350 years.

Even without an analytical solution to the problem, we understand how planetary systems evolve very well and in this section I will describe two key processes that drive the evolution. **Secular** processes which allow planets to exchange angular momentum at large separations and planet–planet **scattering** which leads to an energy exchange between the planets. But before proceeding we consider a few useful definitions. A planet's orbit can be characterized by its energy (E) and its angular momentum (J). The total energy of a planet with mass m_p orbiting a star with mass M_* at a semi-major axis a is given as:

$$E = -\frac{GM_* m_p}{2a}, \tag{1.3}$$

where G is the gravitational constant. The eccentricity can be written as

$$e^2 = 1 + \frac{2EJ^2}{G^2\mu^3 M_*^2}, \tag{1.4}$$

and the total z-angular momentum

$$J_{\mathrm{z,tot}} = \sum_{p=1}^{N_p} \mu \sqrt{G(M_* + m_p)a_p}\sqrt{1 - {e_p}^2}\cos i_p \tag{1.5}$$

where μ is the reduced mass and p denoting the planets in a system. Another useful quantity to keep in mind is the mutual Hill radius of two planets, defined as:

$$R_{\mathrm{MHill}} = \left(\frac{m_1 + m_2}{3M_*}\right)^{1/3} \frac{a_1 + a_2}{2}. \tag{1.6}$$

The separation between two planets in terms of mutual Hill radius can be seen as a simple measure of the dynamical coupling strength between the two planets. Whereas the Hill radius for a single planet is the region in which that planet's gravitational tidal field is stronger than that of the host star.

1.3.1 Orbital evolution

Secular interactions redistribute angular momentum in the system whilst keeping the total angular momentum in the system constant. Laskar (1997) showed that

the system's behaviour can be well understood by considering how much lower the angular momentum is than its maximum possible value. The maximum angular momentum is achieved when all the planets are on circular and co-planar orbits, i.e. when $e_p = i_p = 0$ in equation 1.5. The Angular Momentum Deficit (AMD) can therefore be quantified by considering the eccentricity and inclination of all the planets in the system and subtracting it from the maximum possible value:

$$\mathrm{AMD} \equiv \sum_{p=1}^{N_p} \mu_p \sqrt{G(M_* + m_p)a_p} \left(1 - \sqrt{1 - {e_p}^2} \cos i_p\right). \tag{1.7}$$

AMD can through secular interactions re-arrange itself freely between the planets, resulting in oscillations in eccentricity and inclination.

On longer timescales than the AMD exchange mentioned above, three-body resonances in multiple planet systems can lead to exchange of energy. Given equation 1.4, a change in energy is likely to lead to an increase in eccentricity which increases AMD (Quillen 2011). This diffusion of energy in the system will eventually put it in an AMD-unstable regime, the timescale on which this occurs is a strong function of the initial separation of the planets in terms of their mutual Hill's radii. An AMD-unstable regime means that certain distributions of AMD amongst the planets will result in their orbits crossing. At that point planet–planet scattering will lead to one or more planets being ejected (e.g. Petit et al. 2020).

The ejection usually occurs after a number of direct scatterings between the planets. As they are undergoing this scattering, their angular momentum and energy will keep changing which results in large changes in both the semi-major axes and eccentricities of the planets. At the end of the scattering the less massive planet(s) will be ejected and the more massive one, having done work to eject it, will be left on a more eccentric orbit with a smaller semi-major axis (see equations 1.3 and 1.4). The final eccentricity of the remaining planet will be dependent on the mass ratio between it and the ejected planet with the average final eccentricity increasing as the mass ratio approaches one.

Outcomes

Most of the exoplanet systems that we observe today have already undergone the majority of the orbital evolution that they ever will, throughout the main sequence of their host star. From their orbital parameters we can therefore make inferences

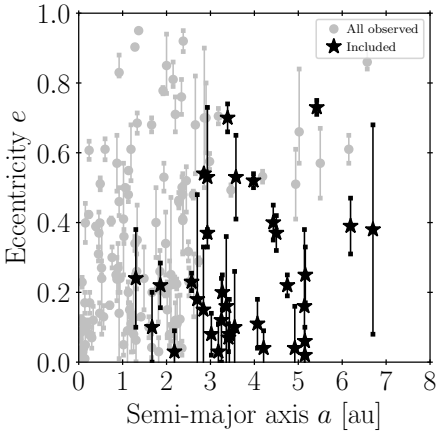

Figure 1.3: The eccentricity and semi-major axis of observed giant planets orbiting main sequence stars at semi-major axes greater than 1 au. The black markers indicate the planets that were simulated in Paper II

about how planetary systems tend to evolve. Looking at the eccentricities of observed gas giants we see that they are on average far higher than what we see in the Solar system; in fact, the gas giants in the Solar system appear to have unusually low eccentricity. Figure 1.3 shows the semi-major axis and eccentricity of observed giant planets (mass greater or equal to Saturn's mass) orbiting main sequence stars with a semi-major axis of 1 au or greater.

There are only two ways in which these planets could reliably have been made this eccentric, either through planet–planet scattering or through the Kozai-Lidov mechanism (described in the next section) induced by a stellar binary. However, it has been shown by e.g. Jurić & Tremaine (2008); Ford & Rasio (2008) that these observations can best be explained by the majority of these eccentric planets having being made so through planet–planet scattering, rather than Kozai-Lidov. This is further supported by the fact that both simulations (Thommes et al. 2008; Mordasini et al. 2009) and observations (Buchhave et al. 2018) that systems hosting giant planets are likely to host more than just the one, i.e. if the conditions for giant planet formation are right more than one giant planet tends to form. Furthermore, figure 1.4 shows the outcome of an experiment performed in Paper II where we show that we can reproduce the observed eccentricity distribution of these planets by assuming that **all** of the eccentricities were a result of planet–planet

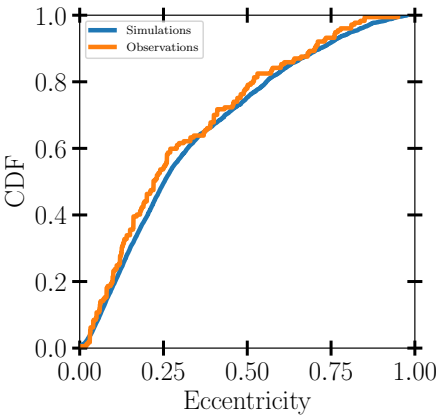

Figure 1.4: The eccentricity distribution of the observed giants shown in figure 1.3, plotted together with the resulting eccentricity distribution planet–planet scattering simulations done in Paper II.

scattering.

1.3.2 The Kozai mechanism

There is a special secular regime in which a highly inclined outer body can drive the inner bodies to very large eccentricities and inclinations through what is known as the Kozai(-Lidov) mechanism (Kozai 1962; Lidov 1962)[1]. When the criteria below are met, the system is in the quadrupolar test-particle limit and can be described rather straightforwardly with the system of equations 1.8. In this limit, for an outer companion (C) to change the orbit of an inner body (A) through the Kozai mechanism (Innanen et al. 1997; Malmberg et al. 2007a):

- $a_{\mathrm{C}} \gg a_{\mathrm{A}}$: The semi-major axis of C needs to be much larger than the semi-major axis of A.
- $m_{\mathrm{C}} \gg m_{\mathrm{A}}$: The mass of C needs to be much larger than the mass of A.
- $\theta > \theta_{\mathrm{crit}}$: The mutual inclination (θ) between A and C need be larger than the critical angle θ_{crit}. Where $\theta_{\mathrm{crit}} = \arcsin\sqrt{2/5} \approx 39.23°$.

[1]In their literature review Ito & Ohtsuka (2019) find that this was first shown by Swedish astronomer Hugo von Zeipel in 1910 (von Zeipel 1910)

Parameter	Definition
i	mutual inclination between A and C
e	eccentricity
ω	argument of pericentre
Ω	longitude of ascending node
τ	rescaled time as per eq. 1.10

Table 1.2: The parameters for the system of equations (1.8)

The change in the eccentricity (e) and inclination (i) of A are determined by the set of differential equations shown below as given in Valtonen & Karttunen (2006):

$$\begin{aligned}
\frac{di}{d\tau} &= -\frac{15}{8}\frac{e^2}{\sqrt{1-e^2}}\sin 2\omega \sin i \cos i, \\
\frac{de}{d\tau} &= \frac{15}{8} e\sqrt{1-e^2}\sin 2\omega \sin^2 i, \\
\frac{d\omega}{d\tau} &= \frac{3}{4}\frac{1}{\sqrt{1-e^2}}\left[2(1-e^2)+5\sin^2\omega(e^2-\sin^2 i)\right], \\
\frac{d\Omega}{d\tau} &= -\frac{\cos i}{4\sqrt{1-e^2}}(3+12e^2-15e^2\cos^2\omega).
\end{aligned} \tag{1.8}$$

With

$$l = \sqrt{1-e^2}\cos i \tag{1.9}$$

as a conserved quantity, which is a measure of how much angular momentum can be redistributed in the system. Each variable in the system of equations above is defined in table 1.2. The rescaling of time, τ, can for C with semi-minor axis $b_{\rm C}$ is given as:

$$\tau = \frac{a_{\rm A}^{1.5}}{b_{\rm C}^3}\frac{m_{\rm A}}{\sqrt{GM_\star}}t. \tag{1.10}$$

From this we can determine the Kozai timescale as a function of the period of A ($P_{\rm A}$) as:

$$T_{\rm Kozai} \sim P_{\rm A}\left(\frac{a_{\rm C}}{a_{\rm A}}\right)^3\left(\frac{M_\star}{m_{\rm C}}\right)(1-e_{\rm C}^2)^{3/2} \tag{1.11}$$

Figure 1.5 shows the solution to the set of differential equations (1.8); in it we see the oscillations as a function of the time parameter τ. The maximum eccentricity is

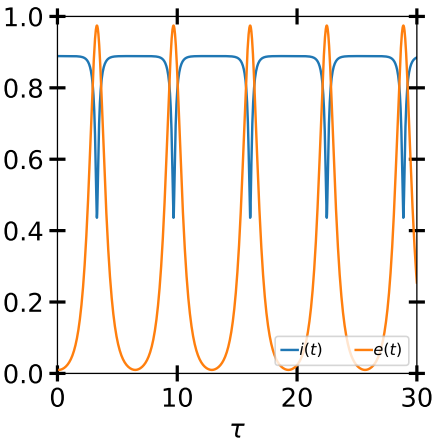

Figure 1.5: The eccentricity and inclination evolution as given by equation 1.8 with initial values of $e_0 = 0.01$ and $i_0 = 80°$. The inclination has been re-normalized such that $90° = 1$, the maximum eccentricity reached is $e = 0.97$ and is given by equation 1.12.

reached when the inclination is at its minimum and vice versa, which makes sense given the conserved quantity, l in equation 1.9. The minimum inclination that can be reached is θ_c and using this we can determine the maximum eccentricity.

$$e_{\max} = \sqrt{1 - (5/3)(1 - e_0^2)\cos^2\theta_0} \tag{1.12}$$

where e_0 and θ_0 are the initial values for the eccentricity of the inner body and mutual inclination between inner and outer body.

1.3.3 Stellar fly-bys

We have just shown how a system can become unstable through internal processes over relatively long timescales. The part of the process that takes the majority of the time is to build up enough AMD to put the system in an AMD-unstable regime. However, AMD can be built up in the system on a much shorter timescale by having a stellar fly-by. This happens when another star gets close enough to the system for its gravitational field to have a significant differential effect on the host star and the planets orbiting it.

Stellar fly-bys will happen almost exclusively in the birth clusters of stars. These are the clusters in which nearly all of the stars are born and they have stellar densities 10^2–10^3 times higher than the Galactic field. During the lifetime of such a cluster ($\sim$ 100 Myr) 10–20% of Sun-like stars are likely to experience a close encounter within 100 au (Malmberg et al. 2011). Such a close encounter encounter can in many cases excite the eccentricities of planets in the system (Malmberg et al. 2011; Cai et al. 2017) which introduces AMD potentially leading to planet–planet scattering.

The whole process of eccentricity excitation, scattering and eventual ejection can in many cases occur on very short timescales, often on a par with the timescale of the close encounter itself. Li et al. (2019) showed that in many such cases the ejected planet can actually be captured by the star flying by and end up on a bound orbit. The captured planets tend to end up on wide and eccentric orbits with the eccentricity following a thermal distribution. This gives a cumulative distribution of the eccentricity that is proportional to the eccentricity squared and has a mean of $1/\sqrt{2}$. They also showed that the orbital plane of the captured planet will be uncorrelated with the orbital plane of the other planets in either system.

Chapter 2

Paper II

2.1 Introduction

The aim of Paper II was to determine which systems are best to observe in order to find an Earth-like planet[1]. We do this because, even though the next generation of instruments will be able to detect Earth-like planets, doing so will still require a large investment in both time and effort; knowing where to look will therefore be very useful.

We determine the list of best systems by considering systems known to contain giant planets (roughly Saturn mass or greater). The reason for using these systems will be discussed in detail in the following section, but suffice it to say that they make good candidates. They do however have one drawback: the gravity from the giant planets can destabilize a large fraction if not all possible orbits in the habitable zone (HZ). The potential danger to Earth-like planets is however not limited to what the giant planet can do in its current orbit, as we know that the orbit can have changed through the dynamical history of the system. For giant planets that have a measured eccentricity we can say that the orbit must have changed with a rather high degree of certainty as they form on initially circular orbits.

In Paper II we simulated the systems as they are observed today and also how they might have looked in the past, i.e. before and while they were undergoing scattering. We measure the habitability of the system by filling the HZ with test particles to determine what fraction of the test-particle orbits remain stable throughout the

[1]A roughly Earth-mass planet orbiting a roughly Sun-like star at approximately one au.

simulations and use the fractions as metrics for how habitable the system is. More specifically, the two metrics are:

> **Present day habitability** - The fraction of test particles that remain in the habitable zone after the system is simulated in its present day configuration for 10^7 years. We denote this as $f_{\mathrm{hab,1P}}$.
>
> **Resilient habitability** - The fraction of test particles that remain in the habitable zone when the past dynamical evolution of the system is simulated, i.e. following the planet–planet scattering phase and after planets have been ejected from the system. We denote this as f_{rhab}.

2.2 Sample used in Paper II

We focus our attention on systems in which giant planets have been detected. Although using these systems have some drawbacks the advantages of using them outweigh them. We argue that these systems are the best ones to look at both from a theoretical perspective by pointing to works that show that giant planets are required to have formed to make Earth-like planets (see e.g. Batygin & Laughlin 2015; Lambrechts et al. 2019) and that for water to exist on the surface injection of comets by the giant planet can be critical (see e.g. Chyba 1990; Morbidelli et al. 2000; Raymond et al. 2006). From an observational perspective there has been work that has shown very large conditional probabilities for the existence of lower mass, rocky planets in systems containing giant planets (Zhu & Wu 2018). Additionally, a nearby system with a gas giant could have its orbital inclination constrained by Gaia (Sozzetti et al. 2008); given that most multi-planet systems have been found to be relatively flat (Lissauer et al. 2011; Johansen et al. 2012) a system in which the gas giant has a low inclination would mean that a potential Earth-like planet would also have a low inclination. A low inclination would make said planet easier to detect as the radial component of the velocity induced by the planet on the star increases with lower inclination making the RV-signal stronger.

But on a more fundamental level, the reason we look at systems with giant planets is that they are the only systems on which we can apply any constraints at all. The first constraint is as follows: *Any system in which the orbit of the giant planet crosses, ventures into or is internal to the habitable zone cannot host an Earth-like planet*. Applying this to all known giant planet systems with main sequence stars leaves us with the systems in figure 2.1. These are the systems that we examine the

habitability of by simulating them in two different ways: we simulate the system in its current configuration to determine what we call the present day habitability and we simulate the potential past of the system to determine the resilient habitability, both defined above. In either case we quantify the habitability by considering what fraction of test particle orbits that we initially place within the habitable zone in our simulations that remain there throughout.

2.3 Initial testing

In figure 2.1 we see that all the systems in our sample show some sign of eccentricity. Planets form on mostly circular orbits (Bitsch et al. 2013; Ragusa et al. 2018) so the eccentricity must have arisen after the planets were formed. Although there are a handful of mechanisms that can make the planets more eccentric, studies looking at the observed eccentricity distributions have found that they are consistent with the vast majority ($\gtrsim$80%) of the systems having undergone giant planet scattering (Ford & Rasio 2008; Jurić & Tremaine 2008). This is further supported by both observations and theoretical studies which show that systems tend to form more than one giant planet if they form any at all (Thommes et al. 2008; Mordasini et al. 2009; Buchhave et al. 2018).

Throughout Paper II we worked under the assumption that *all* of the systems had undergone a giant planet scattering phase. Throughout the instability and subsequent evolution we tracked what fraction of orbits in the habitable zone remained stable, this fraction is the so-called resilient habitability.

In order to examine the history of the observed systems shown in figure 2.1 we must assume something about the initial configuration of the systems. Given the description of the planet-planet scattering one can rather easily conclude that there is a near infinite set of initial conditions that can produce any given observed system.

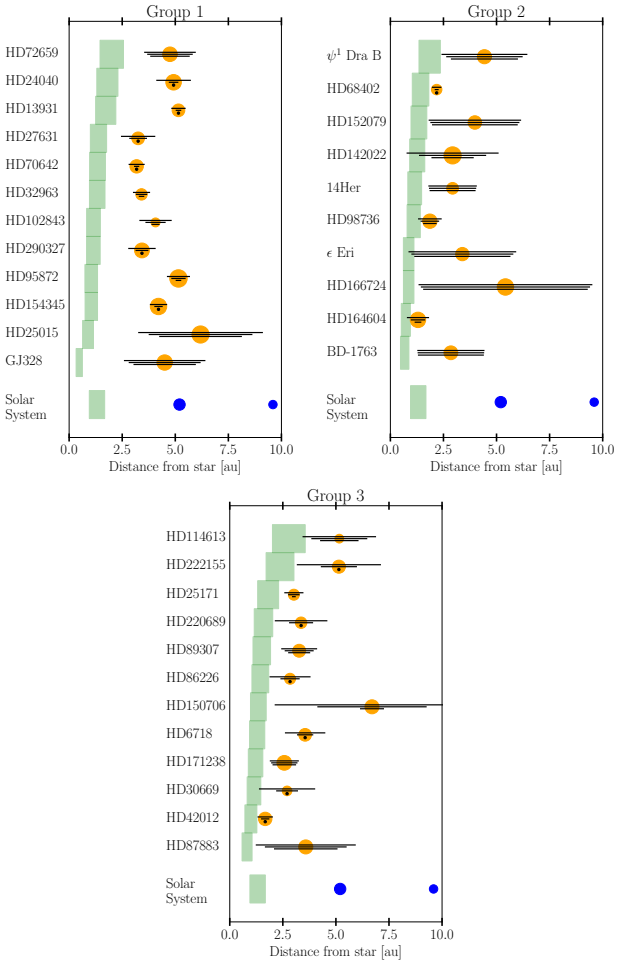

Figure 2.1: The planetary systems simulated. The planet is shown as an orange marker, where the area of the marker is proportional to $\sqrt{M_p/M_\star}$. The black lines show the peri- and apo-center range of the orbit using the reported best-fit and $\pm\ 1\sigma$ values of the eccentricity with a dot denoting that the lower value of the eccentricity gives a circular orbit. The green shaded area is the HZ calculated according to the formula from Kopparapu et al. (2014) (equation 1.1). The systems are split into three categories, from left to right: planets on distant orbits and/or with low eccentricity, planets on nearby orbits and/or with high eccentricity and planets with uncertain eccentricities that could fit in either Group 1 or 2.

Outcomes of planet–planet scatterings

We do a simple experiment in which we show that we can reproduce the entire range of observed eccentricities by using two different two-planet systems with different mass ratios orbiting a Solar-mass star. In the experiment we first simulate the scattering of two Jupiter-mass planets and then of a Jupiter-mass and a Saturn-mass planet. As described previously, the scattering leads to one of the planets being ejected (either one of the Jupiters in the first case and the Saturn in the second case) and the remaining one being left on an eccentric orbit. Figure 2.2 shows the semi-major axis and eccentricity of the remaining planet for the two systems. The eccentricity distribution is clearly dependent on the mass ratio of the two planets, with the average eccentricity increasing as the mass ratio goes towards one. It also appears that the two mass ratios tested are sufficient to cover the entire span of eccentricities.

The findings in our initial testing means that we can settle for only using the two mass ratios defined in the box above when we consider the history of the systems in figure 2.1. As we will show later we did this by assigning probabilities to each system of it having ejected either a lower or equal mass planet. As in; a system with a low observed eccentricity has a high probability of having ejected a lower mass planet and a very eccentric system has a near zero probability of being the result of such an ejection.

2.4 Numerical Experiment

We use the mass ratios in the previous sections and construct two sets of initial conditions for each of the observed systems. One with three equal mass planets (**3E**) where the planet mass equals $M_{\rm p} \sin i_{\rm p}$ of the observed giant. The other one has four planets with the same hierarchical masses (**4H**) as the Solar system giants, with the mass of the innermost one equal to $M_{\rm p} \sin i_{\rm p}$ of the observed planet. We refer to these as [lower case] jupiter, saturn, uranus and neptune. For computational efficiency, both setups have small initial separations between the planets as the only effect that has is to reduce the time until instability (Malmberg et al. 2011).

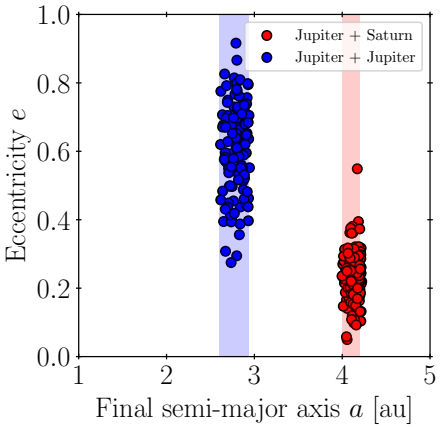

Figure 2.2: The figure shows the a and e of a surviving Jupiter-mass planet after having ejected a second planet in an unstable two-planet system. The shaded region shows the range of semi-major axes permitted based on a simple energy consideration. The two colours show two different mass combinations: Jupiter plus Jupiter, and Jupiter plus Saturn.

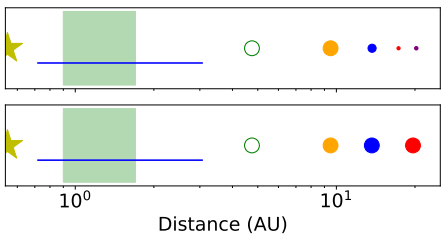

Figure 2.3: A schematic representation of the 3E and 4H initial conditions in a system where the observed planet is located at the empty green circle, with the innermost of the filled circles having a semi-major twice as large as the empty one. This is because the planets will shrink their semi-major axis as per equation 1.3 and end up near the empty green circle. The green shaded region is the HZ and the blue line shows where test particles are initially located. The area of each circle scales as the planet mass they are representing.

Determining the resilient habitability fraction

The initial setups of the simulations are shown in figure 2.3. We start off the innermost planet at twice the separation of the observed planet. We start the integration and the system quickly becomes unstable and ejects a planet and then we keep running it until test particles are no longer being removed.

At the end of the simulation the remaining planet will have a smaller semi-major axis than the innermost one had previously as it has done work to unbind the other planets, which is why we start the planets at twice the semi-major axis of the observed one. Now, the remaining planet in each run will only very rarely end up at the same semi-major axis as the observed planet but we can get around that by rescaling the whole system at the end. We can do the rescaling because other than the probability of collisions during close encounters and the time-scale of the evolution, the dynamics are wholly dependent on semi-major axis ratios rather than the semi-major axes themselves. Rescaling the system includes rescaling the position of the test particles with respect to the HZ which is the reason for having test particles initially extending to either side of it (as seen in figure 2.3).

The fraction of remaining test particles that started in the HZ (after rescaling) in the runs where the eccentricity of the remaining, innermost jupiter is within $\pm 1\sigma$ *of the eccentricity of the observed planet are used for determining* f_{rhab}.

We then compare our simulations of the system's history with simulations of the system in its present day configuration. This comparison is shown in fig 2.4 and in it there is one thing that stands out more than anything else and that is that the resilient habitability is always lower than the present day habitability. This is essentially due to two reasons:

1. The first reason is due to the limits of our observations. We find that in many cases an additional planet remains in the system post-scattering. This planet will be at a large enough separation for the system to be stable, but often close enough to exchange angular momentum and cause eccentricity oscillations. Given that we allow for these oscillations we count planets towards the resilient habitability that at some times might have significantly higher eccentricity than the observed planet. As these oscillations occur on

timescales of tens of thousands of years our observations are by comparison snapshots and do not capture them.

2. Throughout the history planetary orbits and resonances sweep across the HZ and not be there post-scattering. This effect is often seen throughout all the simulations that we perform, and from this we conclude that **history matters**, i.e. when considering how habitable a system is its history must be considered.

2.5 The History

So what is it then that happens through the history of the system, why does it matter so much? Given that the best measure we have of a system's history is its eccentricity it makes sense to consider the history with regards to the eccentricity.

In the correlation between eccentricity and resilient habitability what we find is what one might call a "double-whammy". To unpack this the first thing to consider is that we find that even if a 3E and 4H run end with similar final eccentricities, the 3E runs will in general always be significantly more destructive. The second thing we find is an inverse correlation between resilient habitability and final eccentricity. Combining these two findings with the fact that the probability of a system being 3E rather than 4H also increases with eccentricity is what makes a higher eccentricity doubly bad for the resilient habitability. Hence, as the eccentricity increases the destructive potential of the system's past increases two-fold, both from a dynamical perspective and due to the constraints on its initial configuration.

At first, it might seem odd that the two initial configurations have such drastically different effects on the HZ in runs where the final outcome is similar. Looking closer at the runs we find that in each case there is a different process that dominates the ejection of test particles. In the 3E runs we see that a planet is often scattered into the HZ and when that occurs nearly all of the test particles get ejected on a short time-scale. In the 4H runs the jupiter never enters the HZ, whereas the lower mass planets do it all the time. In the rare case that saturn enters the HZ it does eject a large number of test particles but not as much as a planet in the 3E case would, whereas the frequent and short-lived HZ-crossing orbits of neptune and uranus do close to no damage. The dominant effect is jupiter acting at a

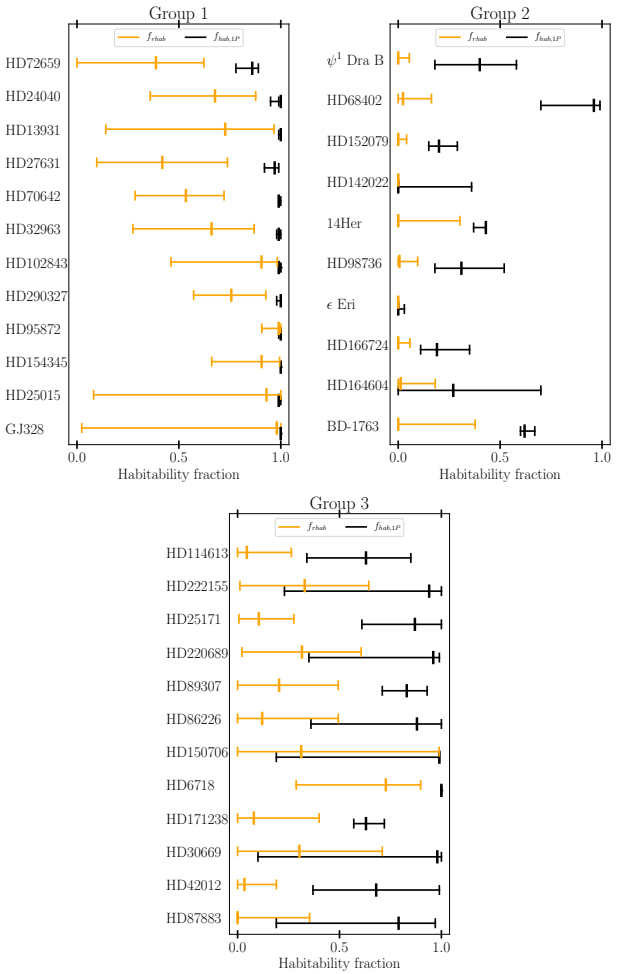

Figure 2.4: The figure shows the range of possible present day habitability (black), given by simulating the system in its observed configuration using the mean and $\pm 1\sigma$ eccentricities. We also show the one standard deviation range of the resilient habitability-distribution (orange), determined as described in the second text box, for the three different groups described previously.

distance through sweeping mean motion resonances. Two orbits are in MMR if their periods have an integer ratio, e.g. 1:2, 1:3, etc. As jupiter does work on the other planets and changes its semi-major axis its MMRs will also change and as these MMRs sweep over the HZ they excite the eccentricity of the test particle orbits leading to their eventual ejection.

2.6 Selected systems

All the low-eccentricity systems in Group 1 make good candidates for observations as they all have high median f_{rhab}-values. We have picked out the ones where the lower end of the orange interval in Figure 2.4 is high: HD 95872, HD 154345 and HD 102843. These are highlighted in Figure 2.5, where we show the resilient habitability for all of the systems we have studied as a function of the giant planet's eccentricity and distance to the HZ.

In Figure 2.5 we also pick out some other systems that offer good prospects for follow up. HD 6718 and HD 150706 have large uncertainties in their eccentricities, and if the true eccentricities are at the lower end of the allowed ranges then their resilient habitability is high. HD 25015 and GJ 328 are of high eccentricity ($e \sim 0.4$) but distant from the HZ. They show strongly bimodal distributions of f_{rhab}: their 3E runs give a very low f_{rhab} whereas the opposite is true for the 4H and given their eccentricity their initial configuration is uncertain.

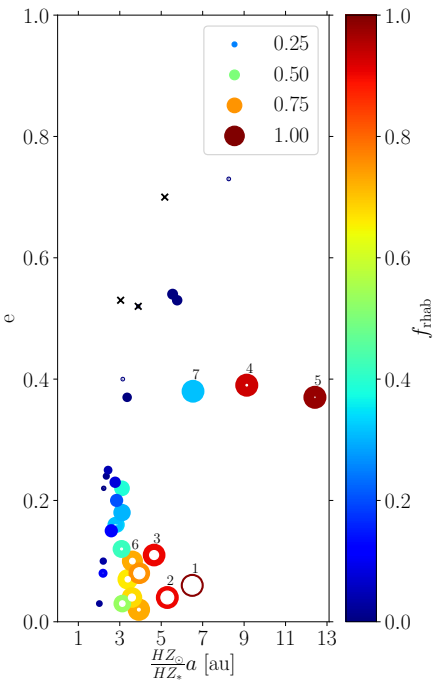

Figure 2.5: The figure shows all of the systems investigated, with their eccentricity plotted against their semi-major axis which is rescaled such that the midpoint of the systems' HZ corresponds to the midpoint of the HZ in the Solar System. The colour-scale shows the resilient habitability and the marker color gives the median of the $f_{\rm rhab}$-distribution. The inner and outer radii of annular symbols scale linearly with the $\pm 1\sigma$ values of $f_{\rm rhab}$-distribution. The crosses indicate systems with a $f_{\rm rhab} < 0.05$. Thus, the blue crosses are very bad, small blue dots are bad, the narrow brown/red annuli are good and the wide annuli give a range of possible outcomes. Our selected systems are:
1) HD 95872 2) HD 154345 3) HD 102843 4) HD 25015 5) GJ 328 6) HD 6718 7) HD 150706.

Chapter 3

Paper III

3.1 Introduction

Nearly all stars form in dense stellar clusters (Lada & Lada 2003). In these stellar clusters, a considerable fraction (10-20%) of Sun-like stars will have encounters within 100 au (Malmberg et al. 2007b) and during such encounters it is possible for planets to transfer between stars (Malmberg et al. 2011) with Li et al. (2020) suggesting that such transfers occur in roughly 1% of encounters. These transferred planets often end up on wide and eccentric orbits (Li et al. 2019) and will therefore rarely directly affect the planets and even more rarely habitable planets in its new host system. However, since these planets tend to be [massive] gas giants (the outermost planets are most likely to be exchanged) and that most stars are surrounded by a debris disk of comets and asteroids much like the Kuiper-belt (Montesinos et al. 2016; Sibthorpe et al. 2018) there is an indirect way in which the transferred planet can affect a habitable planet in its new host system. It can destabilise the orbits of the comets and asteroids and inject them into the planetary system leading to a bombardment of the habitable planet.

In this paper we examined what the effects would be on an Earth-like planet orbiting within the HZ if a planet was picked up by its host star during a stellar fly-by. We consider a system much like our own Solar system with an Earth-like planet in the HZ, giant planets external to it surrounded by an asteroid belt much like the Kuiper belt (referred throughout simply as **the asteroid belt**). The system picks up an additional giant planet during the fly-by and we can conclude that there are four outcomes of a planet being captured into such a system that would affect its

habitability:

1. If the planet is captured on an orbit with a small, HZ-crossing pericentre it can directly scatter out the Earth-like planet.

2. The giant planets can end up being destabilized following the fly-by or be destabilized later through secular interactions with the captured planet. In either case this leads to the scenario examined in Paper II.

3. If the captured planet's orbit ends up crossing the asteroid belt it can destabilize all of it and cause a massive bombardment of the inner planets.

4. The planet can end up on an orbit that depletes the asteroid belt slowly (through e.g. the Kozai mechanism) giving an increased asteroid flux over a much longer time-scale.

In Paper III we looked at the effects of points 3 and 4 but with most of our efforts being focused on 4, as this is by far the most common way a captured planet would affect a planet in the HZ.

3.2 The SEjC system

SEjC is the shorthand we use for the system studied the most in Paper III, it has the following structure: a central star of one Solar mass, an Earth-like planet at 1 au, a jupiter-mass giant planet at 10 au (henceforth referred to as 'jupiter') and an inclined Companion on a circular orbit at 100 au. The setup of this system does not satisfy the criteria presented in 1.3.2 which means that the simple quadrupole approximation will not be valid and that the behaviour will deviate from the system of equations (1.8). These deviations have been studied and to some degree generalized by several authors, e.g. Katz et al. (2011); Naoz et al. (2013b,a); Antognini (2015).

3.2.1 The Kozai mechanism in SEjC

We study this deviation for our particular setup, by focusing on how it affects the eccentricity of jupiter by simulating the SEjC system on its own before including any asteroids. We let the Sun, Earth and jupiter all orbit in the same plane and then do a range of simulations with the Companion on inclinations between 0 and 180. Figure 3.1 shows the maximum eccentricity of jupiter as a function of

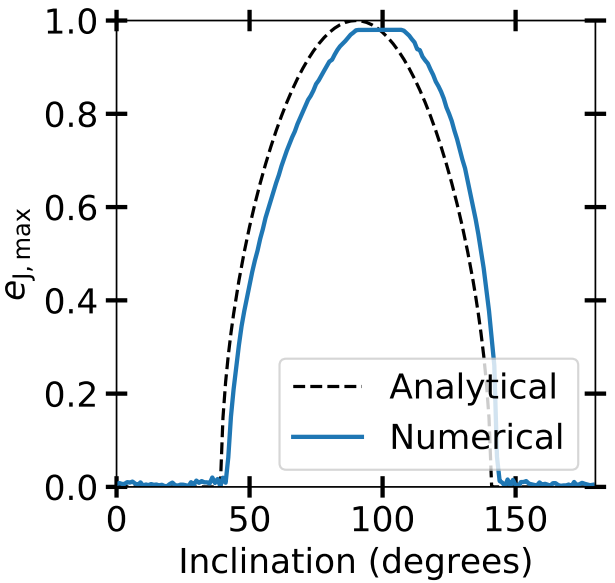

Figure 3.1: The figure shows simulations of SEjC with Companion inclinations $\in$ [0,180]. The dashed black line shows the theoretical $e_{\max}$ given by equation 1.12. The solid blue line shows the maximum eccentricity achieved by jupiter.

the Companion's inclination (solid) plotted together with the analytical values for the maximum eccentricity (dashed) given by equation 1.12. Two things stand out immediately, the flat top and the asymmetry. The flat top is a computational artefact; throughout all of the simulations we kept the stellar radius at 0.2 au in order to prevent the simulation from slowing down during very small pericentre passages; so what the flat top shows is jupiter hitting the star and being removed from the simulation. The asymmetry itself is very much a physical effect, which can be understood by considering what the conditions for the Kozai mechanism given in section 1.3.2 actually mean. The conditions that are not being met for SEjC (1 and 2) state that the vast majority of the system's angular momentum should be held by the inclined companion, which is not the case for SEjC as the Companion holds 75% of it. Therefore, putting the Companion on an equally inclined retrograde orbit will not simply flip the angular momentum vector as the angular momentum vector of jupiter would still point in the same direction; which results in the asymmetry of the system.

3.2.2 Simulating SEjC with asteroids

As mentioned in the previous section we inflate the Sun to 0.2 au in order to prevent the simulation from being bogged down by very high eccentricity asteroids during their pericentre passages (in any case one could argue that they would sublimate if they got that close to the star) but in addition to the Sun we also inflate the Earth to 100 Earth radii. We do this to have some asteroids actually hit the Earth†, both here and in the paper we use a dagger to differentiate hitting the inflated Earth† from a regular sized Earth.

We model the asteroids as a two-component Kuiper-belt located between 45 and 55 au, using the prescription of Volk & Malhotra (2011). This model gives a wide range of inclinations for the asteroid belt which means that for a Companion at a given inclination each asteroid can be placed in one out of three categories. Asteroids with mutual inclination below θ_c that do not undergo Kozai cycles, the asteroids that do and a subset of these whose $e_{\max}$ lead to a pericentre crossing jupiter's orbit that we call 'close Kozai' (ck).

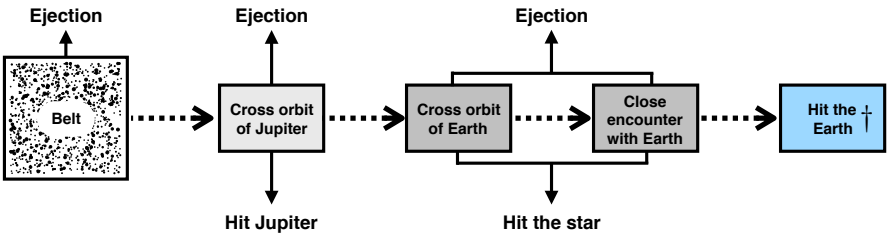

Figure 3.2: The possible fates of an asteroid starting in the asteroid belt. The figure shows every possible way in which the asteroid can be removed in the simulation as well as the hurdles it must pass in order to hit the Earth†.

SEjC simulations – Set 1

We do the simulations for the Companion at five different inclinations w.r.t. the reference frame ([25, 40, 55, 70, 85] degrees). We do different kinds of simulations which we denote with the prefixes/suffixes shown below:

- **ck** – 'close Kozai' asteroids, i.e. asteroids with initial theoretical pericentre less than 10 au.
- **k** – Any asteroid that can undergo Kozai cycles is included.
- **f** – Full asteroid belt
- **r** – Runs with companion on retro-grade orbit. We give it an inclination using figure 3.1 that results in the same $e_{\max}$ for jupiter.

For each inclination we do 150 runs of each kind with random phasing for the planets and a small random eccentricity and inclination on jupiter. Each run includes 150-250 asteroids as test particles, ck is done at the highest resolution with a total of 37 500 asteroid orbits, 20 000 for k/r and 15 000 for the full runs. The companion is placed at 100 au on a circular orbit and we let the simulation run for 100 Myrs.

We track the fate of each asteroid and summarize the possible outcomes in figure 3.2. The flowchart shows how an asteroid gets from the belt to hitting the Earth†. The vertical arrows in the flowchart shows ways in which an asteroid

can be removed from the system, these are; ejection by Companion whilst still in the belt or by jupiter/Earth as it crosses their orbit, hitting the star or hitting the Earth†/jupiter although the number of jupiter-hits are pretty much negligible. The fraction of asteroids that end up being removed in each manner (or remain in the belt) changes with the Companion's inclination, with the fraction of asteroids hitting the star rising sharply with inclination being most significant. However, when we compute how many asteroids would actually hit the Earth we find the same number regardless of the Companion's inclination. Of the removed asteroids 4×10^{-6} end up hitting the Earth, which can represent as many as 10^4 km-sized impacts when considering a Kuiper-belt like asteroid belt. The constant fraction regardless of Companion inclination we interpret as being because the asteroids hitting the Earth will always encounter jupiter along the way, which changes their orbit so much so that its previous orbit no longer matters.

The fraction hitting the Earth being independent of the Companion's orbit is very useful. This means that for any given Companion orbit we only need to consider the asteroids removed from the belt rather than tracking their encounters with Earth. This both allows us to speed up the computations both by using fewer asteroids and to do the simulations without including the Earth. Since the time-step is determined by the period of the innermost orbit ($\sim 1/12$th of it), removing the Earth results in speeding up the simulations by essentially an order of magnitude; and reducing the number of asteroids speeds it up even more. This means that we can do simulations that run for much longer to study the long term effects on the asteroid belt by less destructive Companions, e.g. ones on more distant orbits and/or with lower inclinations.

3.3 Generalizing farther

We do two more sets of simulations (set 2 and 3), now without including the Earth. Set 2 is essentially a follow-up on the SEjC runs in which we look at the long term behaviour of the runs with low inclination with a full asteroid belt. In the set 3 simulations we utilize what we learned in both the SEjC and set 2 to explore the parameter space of Companion orbits. We examine how much the orbits disrupt the asteroid belt, the resulting impact rates and the duration of the bombardments.

Long high resolution simulations – Set 2

We redo the f-simulations for Companion inclinations of [25, 40, 55] and their retrograde counterparts, i.e. we initialize the system with the exact same initial conditions for Companion, jupiter and all of the asteroids but without the Earth. Excluding the Earth makes the new 1 Gyr run take about as long as the previous 100 Myr run.

We then fit a two-component exponential function (shown below) to the fraction of asteroids remaining in the belt.

$$f(t) = A \times \exp(-Bt) + C \times \exp(-Dt) + E \tag{3.1}$$

We find that the equation fits the data very well with one faster-acting exponential and one slower. We interpret this as each exponential corresponding to the work done by each body on the asteroids to unbind them, with jupiter giving the fast exponential and the Companion the slow one.

We now consider the different orbits on which the Companion can be captured. We consider three types of orbits on which it can be captured that affects the asteroid belt:

1. The Companion can orbit-cross the asteroid belt disrupting it directly.
2. The Companion can pump up the eccentricities of the asteroids with either the Companion itself or jupiter ejecting them later.
3. The Companion can pump up the eccentricities of the asteroids and then have them be removed by only jupiter.

We test a number of orbits to explore the different effects; the semi-major axes and eccentricities of these orbits are shown in figure 3.3.

Exploring effects of different Companion orbits – Set 3

For each black cross in figure 3.3 we simulate a Companion at six different inclinations; [40,55,70] and their retrograde counterparts. These simulations are also run for 1 Gyr without the Earth as in Set 2, they are however done in lower resolution using 1 500 test particles rather than 15 000 and additionally jupiter is moved from 10 to 5 au as it allows us to test a larger part of the phase space as per figure 3.3.

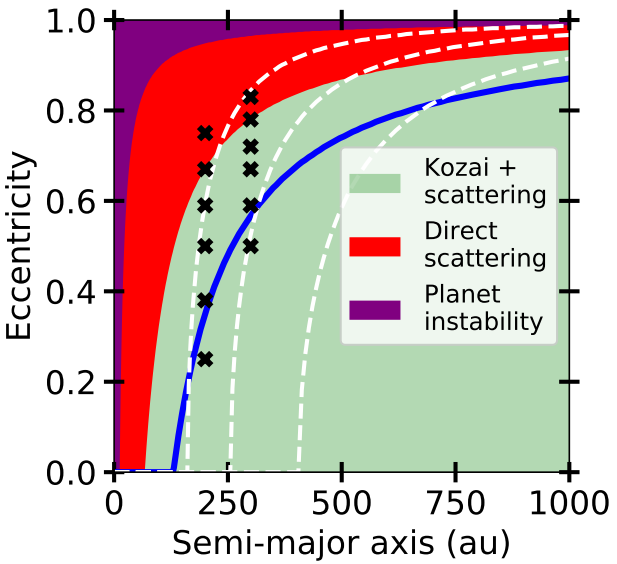

Figure 3.3: The different effects that are dominant for different a and e for captured planets. The purple region shows where the system would be wholly disrupted. Red region shows where effect 1) dominates. The green region shows where effect 2) and 3) dominate with the blue line being the boundary between them. The black crosses show the Companion's a and e in the Set 3 simulations. The white lines show where the precession from a Jupiter-mass inner planet with a semi-major axis of (from left to right) 10, 5 and 2.5 au blocks the Kozai cycles of the asteroids.

Then, given our findings in the higher resolution runs of Set 2 we also fit equation 3.1 to the outcomes of these simulations. Our findings do indeed match what we predicted in figure 3.3. We see a very rapid depletion when in the red, a sharp decline in rates as we move into the green regime which slowly decreases as the pericentre moves outward only to have another sharp decrease once the blue line is crossed.

3.3.1 Computing impact rates

We showed with SEjC that the fraction of asteroids that hit the Earth out of the removed ones remain constant with Companion inclination, we have in Paper III extended this by claiming that the fraction remains constant regardless of the Companion's orbit. Then, in order to go from fractions to actual impact rates we need to determine the number of asteroids in the asteroid belt. We chose to consider > 1 km sized asteroids as these are large enough to have global impact (Toon et al. 2016) on an Earth-like planet. Occultation-studies put the number of > 1 km sized bodies at $\sim 10^{10}$ (Schlichting et al. 2012), with a steep size-distribution meaning the vast majority of these will be roughly km-sized. The number of asteroids hitting the Earth will then simply be $10^{10} \times f_{\text{removed}} \times 4 \times 10^{-6}$ or $40\,000 f_{\text{removed}}$ where f_{removed} is the fraction of asteroids removed during the simulation.

3.4 Effect on habitability

We find that in roughly 40% of the cases where a Companion is captured it will either be on such a high inclination as to make the planets cross their orbit or push them into the star. Or, it will be on such an eccentric orbit that it itself crosses the orbits of the inner planets. Therefore, in these cases the capture of a Companion renders the system essentially uninhabitable. For the remaining 60% of cases we consider what the Companion does to the asteroids and compare that to the Earth. The impact rate of > 1 km sized bodies on the Earth is $\sim 1\ \text{Myr}^{-1}$ and when considering the effects on habitability the simulated impact rates have, we present them in terms of how many times higher they are than the impact rate on Earth. We determine the outcomes by drawing a large number of Companion orbits with isotropic inclination and thermal eccentricity (as shown by Li et al. 2019) and interpolating over the outcomes from the simulations done in 3.3. The outcomes fall roughly in one of three equally probable groups:

1. Enhancements of a few hundred to around a thousand times the Earth-rate that lasts for a few tens of Myr.

2. Enhancements of a few tens to a hundred or so times the Earth-rate that lasts for a few hundred Myr.

3. Enhancements of up to ten or so times the Earth rate that lasts for a Gyr or longer.

Given that Companions are captured in the birth clusters of stars, 1) and 2) will likely not have an effect as the terrestrial planets might not even have finished forming or it might still be very early in their history, whilst they are still far too hot to support any liquid water on their surface. An enhanced rate of asteroid bombardment that lasts for a Gyr or more as in 3) however will very likely be detrimental for the development of life on such a planet. This means that the Companions that end up on low to moderate inclinations with moderate to large pericentres will be the ones who will impact the habitability on Earth-like planets.

Chapter 4

Paper I

4.1 Introduction

As a star moves through the Galaxy it can encounter things that can be very harmful for life on habitable planets orbiting it. These encounters have the potential to induce so called mass extinctions. In Paper I we examine the risk of mass-extinction events as a star passes through a giant molecular cloud (GMC).

Whilst no strict definition exists of a mass extinction, they are considered to occur when a large fraction ($\gtrsim$ 10%) of species disappear from the fossil archive, the most notable of which might be the end-Cretaceous extinction in which the (non-avian) dinosaurs were all killed by an asteroid impact (Alvarez et al. 1980). However, the possibility of an astrophysical connection to mass extinctions was first pointed out by Oort (1950) who hypothesised that Galactic tides can perturb comets in the outer Solar system and send them plunging inwards towards the inner planets. A few decades later the idea was reinvigorated by the rather controversial findings of Raup & Sepkoski (1984) who found a periodic signal of 27 Myr in the mass extinction record on Earth.

Analysis by several other authors (Lutz 1985; Stigler & Wagner 1987; Heisler & Tremaine 1989; Feng & Bailer-Jones 2013) could not confirm their periodicity and pointed to faults in their methodology. However, the idea of a periodic extinction record with a period of $\sim$ 30 Myr has persisted Yabushita (1997); Rampino (1997) and even been shown to have been made more significant with a time-revision due to updated dating methods Melott & Bambach (2013). There has

also been a divergence with some authors suggesting a 60 rather than 30 Myr period Lieberman & Melott (2007).

Several different mechanisms have been proposed to explain this periodicity, with some of the more popular including: The presence of a distant planetary companion in the Solar system (Whitmire & Jackson 1984), reversal of the Earth's magnetic poles (Raup 1985; Stothers 1986), crossing through the Galactic midplane (Rampino & Stothers 1984; Bahcall et al. 1985; Shaviv et al. 2014) and spiral arm crossings (Leitch & Vasisht 1998; Shaviv 2002, 2003; Gillman & Erenler 2008). For a detailed review on the topic see Bailer-Jones (2009).

In Paper I we have essentially considered how often stars on different orbits cross through the spiral arms but on a more granular level. We consider how often stars cross through GMCs, most of which happen to be located within the spiral arms. Further, we postulate that any extinction-level event as a result of crossing a spiral arm would be due to a GMC and not a spiral arm potential.

4.1.1 Mass extinctions induced by giant molecular clouds

The natural first question to ask is: How can a GMC cause a mass extinction in stellar systems passing through it? In Paper I we discuss three potential mechanisms: Tidal force leading to cometary bombardment, accretion of gas into the system leading to an ice age and supernovae within GMCs exploding near the star.

GMCs are very massive and rather compact and therefore have a significant tidal field. As such, comets in a structure such as the Oort Cloud (Oort 1950) (believed to exist around most other stars: Tremaine 1993; Raymond et al. 2012) are easily unbound (Napier & Staniucha 1982; Hut & Tremaine 1985) as a star passes through a GMC. Many of these unbound comets can then be injected into the planetary system leading to giant impacts (Rubincam 2016).

As the star passes through the GMC it can accrete upwards of an earth mass of gas (Hoyle & Lyttleton 1939). This gas can settle in the upper atmosphere of planets and when doing so can seed rapid cloud formation (Kataoka et al. 2013) or enshroud the upper atmosphere (Pavlov et al. 2005; Nimura et al. 2016). Both of these will cause a sharp decline in light received by the planet, in the first case it is due to an increase in albedo and in the second the light is simply blotted out; both of them can lead to a so-called "Snowball Earth" scenario.

The threat that poses the greatest danger and has the highest probability of causing significant damage to the biosphere is not the GMC itself, rather it is the risk of being struck by a supernova during the passage through the GMC. The reason for this high risk is that nearly all stars are formed inside GMCs. Stars that end their lives as core-collapse supernovae are short-lived (< 50 Myrs, see e.g. Zapartas et al. 2017) and therefore end their lives and explode where or close to where they are born. The type I supernovae which are the result of mass transferring binaries happen on much longer time-scales and are thus distributed throughout the Galaxy but they only represent $\sim$30% of all supernovae (Li et al. 2011). Therefore, the risk of being struck by a supernova when inside a GMC is much higher than anywhere else in the Galaxy.

Whilst it might seem obvious that a nearby supernova would be catastrophic for life on the surface of a planet it is not clear exactly why that would be. Here are a few ways in which they could affect the planet:

1. Assuming the planet has an ozone layer protecting it from high energy radiation, Beech (2011) shows that a typical 10^{46} J supernova (which has an F-UV/X-ray effect of $\sim 10^{38}$ W for the first few minutes) within 9 pc can cause mass extinction due to UV and X-ray irradiation of the surface. That is under the assumption that the ozone layer absorbs 99% of the radiation, barring such protection the "kill radius" would be 90 pc.

2. Ruderman (1974) discusses a mechanism in which the ozone layer can be destroyed by the formation of nitric oxide (NO) in the upper atmosphere which then will destroy the ozone and cause the UV flux of the host star to cause the mass extinction. Taking the Sun as an example, it has an FUV/X-ray power output of 10^{20} W (Güdel 2007), meaning the irradiation of the Earth will be a factor 10^3 lower than that of the Beech (2011) supernova[1], however the ozone will take decades to replenish (Thomas et al. 2005) meaning the overall irradiation will be significantly higher as the relative duration differs by a factor of 10^6. For the destruction of the ozone layer to occur, Ruderman (1974) assumes a supernova producing 10^{40} J of X-rays

[1] $(1 \text{ au} / 90 \text{ pc})^2 \approx 10^{-15}$

or $10^{43} - 10^{44}$ J of cosmic rays needs to occur at a distance of ~ 15 pc.

3. Thomas et al. (2005) showed (in the context of a 2 kpc distant GRB, producing equivalent amounts of FUV and X-rays hitting the Sun as a nearby supernova) how the production of NO can lead to an extinction from an ice age rather than irradiation. The NO will form nitrogen dioxide (NO_2) which will significantly increase the albedo of the planet plunging it into an ice age. Not only that, but the biosphere would also be stressed by nitric acid rain.

4. Tanaka (2006) showed that at a distance of 12-15 pc 10^{43} J of cosmic rays can also cause an ice age by seeding cloud formation in the upper atmosphere.

Which one of these effects will cause the mass extinction in the event of a nearby supernova is up for debate but it will likely depend on the distance to the supernova and the conditions in which it occurs. Further, these works all consider the Sun completely unshielded, however the nearby supernovae we will discuss in this paper occur within GMCs. The amount of shielding will depend strongly on what kind of GMC the supernova occurs in and where in the GMC it happens. Regardless, it is clear that the relatively dense gas will provide some form of shielding and for this reason we adopt a 10 pc kill radius.

4.2 GMCs in the Galaxy

The life of a typical GMC can be put in rather concise terms nicely summarizing how we model them in Paper I: Gas falls into the spiral arm potential and as it does an over-density forms which grows as the gas falls deeper into the potential. At some point stars form in the newly born GMC and the feedback from the stars along with the fact that the GMC starts climbing out of the spiral arm potential leads to the GMC dispersing. After the gas is dispersed a young stellar cluster is left behind.

4.2.1 GMC properties

GMC masses range between $\sim 10^4$ *to a few times* 10^6 *Solar masses with sizes ranging from one to few tens of parsec. They are transient structures that form and dissolve in*

roughly 40 million years.

Rosolowsky & Leroy (2006) gives the mass distribution of GMCs for local galaxies on the form:

$$\frac{dN}{dM} = (\gamma + 1)\frac{N_0}{M_0}\left(\frac{M}{M_0}\right)^{\gamma}, \quad M < M_0. \tag{4.1}$$

For the Milky Way they find a best fit by setting the constants, $\gamma = 1.53$ and $N_0 = 36$. M_0 is the maximum mass of $3 \times 10^6 \mathrm{M}_\odot$. The minimum mass is $10^4 \mathrm{M}_\odot$. The resulting mass distribution ends up being fairly top heavy, with 3.5% of GMCs above $10^6 \mathrm{M}_\odot$, accounting for 40% of the total H_2 mass. The mass of the GMC drawn from this distribution corresponds to M_i in equation 4.4.

GMCs are large, their exact size is determined by measuring their angular radius (typically arc minute scale) and computing the distance to them. The distance is computed by assuming they are on circular orbits, which is reasonable as the gas they form from is dissipative. With that assumption and a measured radial velocity and position relative to us the distance can then be computed. If the rotation curve is roughly flat, the distance is given by first calculating its Galactocentric radius as:

$$R = \frac{R_\odot V_c \sin l}{V_c \sin l + V_\mathrm{r}}. \tag{4.2}$$

Here V_c is the circular rotation velocity, V_r the measured radial velocity, $R_\odot$ the Solar Galactocentric radius and l the Galactic longitude-coordinate. The distance from the Sun is then simple trigonometry.

Computing the distance gives the size of the GMC, the mass of the GMC is determined by inferring its density. The density of the GMC is inferred by measuring the column density of the CO. More specifically (as described in Pineda et al. 2008), the ^{12}CO is assumed to be optically thick and in local thermodynamic equilibrium (LTE), assuming the same excitation temperature and that ^{13}CO is optically thin, a relation between the integrated ^{13}CO-intensity along the line of sight, and the column density can be derived. The ^{13}CO column densities are then usually converted into ^{12}CO column densities using a uniform $n(^{12}\mathrm{CO})/n(^{13}\mathrm{CO}) = 45$ isotope ratio. Finally, H_2 mass is determined by using $n(^{12}\mathrm{CO})/n(\mathrm{H}_2) = 8 \times 10^{-5}$. From this we get a mass and for the radius we use the mass-relation from Roman-Duval et al. (2010) who finds:

$$\left(\frac{M}{\mathrm{M}_\odot}\right) = A \times \left(\frac{R}{1\mathrm{pc}}\right)^{2.36}, \tag{4.3}$$

with $A = 228$. Further analysis in Roman-Duval et al. (2016) revealed three distinct GMC populations, which they dubbed diffuse, dense and very dense; representing 25, 60 and 15% of the molecular gas respectively. $A = 228$ gives the mass-radius relationship for the very dense GMCs with surface densities between 130 and 300 $\mathrm{M_\odot pc^{-2}}$, given the mass limits from equation 4.1. As no mass-radius relations are provided for the diffuse and dense GMCs we utilize 4.3 with two different values of A. $A = 79$ represents the dense GMCs and covers the range from 50 to 130 $\mathrm{M_\odot pc^{-2}}$, for the diffuse GMCs we pick $A = 28$ which covers 25 to 50 $\mathrm{M_\odot pc^{-2}}$.
As mentioned, the GMCs are transient structures, meaning they form and dissolve. The formation and dissolution is described by Gustafsson et al. (2016) where they show that the change in mass over time is well described by:

$$M(t) = \left(-0.25 \times \left(\frac{t - t_0}{10} \right)^2 + \frac{t - t_0}{10} \right) \times M_i. \tag{4.4}$$

where M_i is the maximum mass and $t - t_0$ is the age at time t in Myr. Equation 4.4 gives a 40 Myr lifetime where the GMC mass is given as a symmetric parabola peaking at 20 Myr. The 40 Myr lifetime is consistent with observations from e.g. Williams & McKee (1997), Vallini et al. (2016), and the shape of the function given by equation 4.4 is based on simulations from Krumholz et al. (2006) and Goldbaum et al. (2011).

4.2.2 GMC distribution

GMCs are predominantly located inside spiral arms and are compared to the stars in the Galaxy, on flatter and more centrally concentrated orbits.

Figure 4.1 shows the M81 spiral galaxy, which is a galaxy very similar to our own. It is in the spiral arms that we distribute the GMCs in Paper I. We distribute them according to the spiral pattern observed by Hou & Han (2014), where we utilize the best fit which they determine by combining observations carried out in three different ways. They are as follows:

1. Observations of HII regions, GMCs are regions of star formation and young, hot stars will ionize the surrounding hydrogen gas.

2. Observations of methanol masers which also trace star formation.

3. Observations of carbon monoxide (CO) emission lines. CO is a very fragile molecule that cannot survive unless embedded in another, dense gas. It is therefore an excellent tracer for GMCs.

To the observations they then fit a logarithmic spiral, which in cylindrical coordinates is given as:

$$\ln \frac{R}{R_\mathrm{i}} = (\theta - \theta_\mathrm{i}) \tan \psi_\mathrm{i} \tag{4.5}$$

Where R_i is the starting radius, θ_i the starting angle and ψ_i the pitch angle, i.e. how non-circular the spiral is.
Due to the GMCs being so short-lived they largely follow the same radial and vertical scaling as the molecular gas; i.e. a vertical scale height of ~ 100 pc and scale radius of ~ 1.8 kpc (Clemens et al. 1988; Nakanishi & Sofue 2006). This is because the process which could change their orbits (interactions with other GMCs or the spiral arm potential) act on much longer time-scales than the lifetimes of the GMCs.

4.2.3 Star formation and supernovae

GMCs are lumpy balls of gas: in the clumps stars are formed. The more massive stars formed will be short-lived and detonate as supernovae within the GMC. How many supernovae occur within each GMC is dependent on the GMC mass and the stellar initial mass function.

As discussed previously, the potentially greatest threat, when encountering a GMC, pose to habitability is being struck by a supernova. The risk arises because GMCs are sites of star formation and stars that end their lives as supernovae are short-lived, meaning they tend to explode before having time to leave the GMC. To determine this risk we need to compute how many supernovae occur during the GMC's 40 Myr lifetime which we can do given an star formation efficiency and stellar mass function.

One can represent GMCs overall well by assuming them to be balls of uniform density as shown by Roman-Duval et al. (2010) and this is sufficient for most of the simulations we perform. However when we look at the supernovae in particular we need to consider the internal structure of the GMCs (as seen in section 4.5.2) and how this relates to star formation. Looking at the internal structure one finds large scale filamentary overdensities known as clumps. The clumps in turn also have

overdense substructures known as cores, which is where the stars form (Draine 2011). Stars forming in the cores will lead to more cores forming in the clumps which in turn form more stars until most of the clump mass is converted to stars. Observations put the clump mass fraction at $\sim$ 10% (Wienen et al. 2015; Faesi et al. 2016; Ochsendorf et al. 2017) which appears to be consistent with the star-forming efficiency one finds in simulations (Federrath & Klessen 2012; Hopkins et al. 2012; Körtgen et al. 2016).
As an initial mass function we use the one from Kroupa (2001). This IMF is shown below:

$$\frac{dN}{dM_*} = C_\alpha \, M_*^\alpha \tag{4.6}$$

where C_α is a constant dependent on α chosen such that the function is continuous and

$$\alpha = \left\{ \begin{array}{ll} -0.3, & 0.01 < M_*/M_\odot < 0.08 \\ -1.3, & 0.08 < M_*/M_\odot < 0.5 \\ -2.3, & 0.5 < M_*/M_\odot < 100 \end{array} \right\} \tag{4.7}$$

Using the Kroupa IMF results in one in 300 stars being above 8 solar masses; or, for every 100 $M_\odot$ of stars formed there is one supernova.

Figure 4.1: Composite image of the grand design spiral galaxy M81 utilizing the Hubble, Spitzer and GALEX space telescopes.
Image credit: Courtesy NASA/JPL-Caltech.

Our GMC model

Throughout the integration we have a constant number of GMCs, set to 6700. This gives a total average GMC mass, consistent with observations of the H_2 mass in the Galaxy ($6.5 \times 10^8 M_\odot$, Roman-Duval et al. 2016; Miville-Deschênes et al. 2017) when considering that our GMC mass will vary with time.

Each GMC has a set life-time of 40 Myr. We generate them in the simulation such that they cross the curves defined by eq. 4.5 after 20 Myr and mimic their behaviour by increasing their mass as it is traveling towards the arm and later decrease in mass as they move away. The change in mass with time is modelled using equation 4.4.

After 40 Myr passes the GMC is removed from the simulation and replaced by a new one at a random location in the Galaxy. The R and z at which each GMC is placed is set by observations of the surface density and scale heights of molecular hydrogen by Nakanishi & Sofue (2006).

We put everything together and compare it to observations. Using the time averaged total H_2 mass of $6.5 \times 10^8 M_\odot$ with 40 Myr lifetime of GMCs during which 10% of their mass is converted to stars we end up with a star formation rate of 1.64 $M_\odot$ yr^{-1}. This agrees well with observations; Licquia & Newman (2015) find a SFR of $1.65 \pm 0.19 M_\odot yr^{-1}$.

4.3 Stellar orbits

The key difference between a star orbiting in a galaxy and a planet orbiting a star is the potential. Whereas the planet orbits a point mass, the star orbits inside a density distribution. The resulting orbit of the star will not be closed, i.e. it will never return to the same spot as it was in before. In qualitative terms the stellar orbits can be described as follows:

First, we consider the XY-plane in which a star will do epicycles. Each star has a so-called guiding radius (R_G), which is the Galactocentric radius around which

the orbit cycles. As the star does one revolution around the galaxy it will do several cycles around its guiding radius. In the Z-direction the star will oscillate around the mid-plane. If its epicycles are small compared to the scale length of the galactic disk potential (~ 3.5 kpc) then the motion in Z can essentially be seen as a harmonic oscillator. If not then the oscillation amplitude will go up and down with increasing and decreasing R. We see this behaviour in our simulations where some stars with large non-circular velocities will change their $z_{\max}$ for a given V_z throughout their orbit.

4.3.1 Changing stellar orbits

The fact that the Galactic potential has non-axisymmetric components in terms of spiral arms and local overdensities in terms of GMCs means that a star orbiting inside it will neither conserve its orbital angular momentum nor its orbital energy. This results in stellar orbits changing over time.

As we will see later, the key findings in Paper I is that the GMC encounter rate is a steep function of both its guiding radius (R_G) and its velocity in the Z-direction; which at $Z = 0$ we denote as V_z. Both the R_G and V_z of a star will change as a star ages and orbits through the galaxy. Stars get *hotter*, i.e. their non-circular XY-velocities and their Z-velocities increase (Nordström et al. 2004). And through interactions with the spiral arms they can can change their guiding radii.

We can easily show that the changes do not occur through interactions with other stars by considering the relaxation time of the system:

$$t_{\rm relax} \simeq \frac{0.1N}{\ln N} t_{\rm cross}. \tag{4.8}$$

Typical galaxies have crossing times of $\sim 10^8$ years and $\sim 10^{11}$ stars, meaning star–star interactions can be disregarded. The interactions that change stellar orbits will be those with GMCs and spiral arms.

Consider a star scattering against a GMC, due to the large difference in mass we can approximate the star as a test particle and work from the rest frame of the GMC. In this frame the star has a Jacobi energy[2]:

[2]The only conserved quantity in the restricted 3-body problem

$$E_j = \frac{1}{2}|v|^2 + \Phi_{eff}(r) \tag{4.9}$$

where v is the velocity of the star in the rotating frame and Φ_{eff} is sum of the gravitational and centrifugal potential. E_j being a conserved quantity in this frame one can see that the only thing a scattering can do is to change the direction of v, not its magnitude.

We examine the effects of such a change by looking at the total angular momentum J. We can split J into the components $J_{\rm rand}$ and L, where L is the rotational angular momentum or a proxy for the guiding radius and $J_{\rm rand}$ the random component of it or a measure of how dynamically *hot* a star is. We can write $J_{\rm rand}$ as:

$$\Delta J_{\rm rand} = (\gamma^2 - 1)\frac{u_\phi + \frac{1}{2}\Delta u_\phi}{v_c}\Delta L. \tag{4.10}$$

Here u_ϕ is a component of the epicycle energy and γ is twice the ratio of the orbital and epicycle frequency. This shows that any change in L will also result in a change in $J_{\rm rand}$, except at co-rotation where $u_\phi = \Delta u_\phi = 0$. Given that only a small fraction of stars will encounter clouds with $u_\phi \approx 0$ we can conclude that GMCs will be much more efficient at dynamically heating stars, rather than changing their guiding radii.

Now let us consider the spiral arms. An orbit in a steady state non-axisymmetric rotating potential has the conserved quantity:

$$E_j = E - \Omega_p L \tag{4.11}$$

where E and L are the specific energy and angular momentum of the star in a non-rotating frame and Ω_p is the pattern speed of the perturbation. This gives us the relation:

$$\Delta E = \Omega_p \Delta L. \tag{4.12}$$

Then by splitting up the energy into a specific and circular energy and a radial part one can in the same manner as before find how to change the angular momentum without changing the eccentricity of the orbit. It is given as:

$$\Delta J = \frac{\Omega_p - \Omega}{\omega_R}\Delta L, \tag{4.13}$$

Here J is a radial action, e.g. a change that would make the orbit more eccentric, Ω_p the pattern speed, Ω the orbital frequency, ω_R the radial oscillation frequency and L the specific angular momentum. This shows that the guiding radius of an orbit can be increased without changing the eccentricity when at co-rotation, i.e. when $\Omega_p = \Omega$. This mechanism was first proposed and confirmed in Sellwood & Binney (2002) and later dubbed "churning" by Schönrich & Binney (2009) who also dubbed heating in the XY-plane as "blurring".

This has two significant implications for the work in Paper I:

1. It means that a given star could have originated at any radius and there would be little to no dynamical evidence of its past. We show in Paper I that the guiding radius is key in determining how often stars encounter GMCs, however our Galactic potential does not include a spiral arm component which means that there will be no radial migration; instead we do simulations at a range of different radii. This means that we can consider both the GMC encounter history and future encounters of a star regardless, because we can consider stars with similar dispersions at different radii.

2. The longer a star orbits throughout the Galaxy the hotter it gets, i.e. the larger its non-circular velocity component becomes. Rather than doing simulations on 10 Gyr time-scales, we do a sets of 1 Gyr simulations with a range V_z and the XY-plane velocity randomly drawn from a Gaussian distribution. Setting up the simulation this way means that we end up simulating 1 Gyr snapshots of stars at different ages.

4.4 GMC encounter rates

Simulations performed

The simulations consist of integrating a range of stellar orbits through a Galactic potential in which the GMCs described in the previous section are also orbiting and logging whenever a star on a particular orbit crosses through a GMC.

Following Feng & Bailer-Jones (2013) we perform the simulations using a three-component symmetric, analytic Galactic potential given in García-Sánchez et al. (2001); consisting of a Miyamoto (Miyamoto & Nagai 1975) disk and a Plummer (Plummer 1911) bulge and halo.[a]

We do a set of simulations where for each simulation we initialize 50 000 stellar trajectories at 8 different radii, $R = (5, 5.5, 6, 6.5, 7, 7.5, 8, 8.5)$kpc. We do 1000 runs for each integer V_z between 1 and 50 km/s where V_z is the velocity away from the Galactic plane defined at $z = 0$. The azimuthal angle, θ, was randomly, uniformly chosen between 0 and 2π. We set the in-plane velocity to equal the local circular velocity plus a random component drawn from a Gaussian velocity dispersion distribution. For the different simulations that we perform we vary the velocity dispersion and try a range of different spiral and GMC distributions.

[a] We did some tests including a spiral arm potential and found small differences in the encounter rates of $\sim 5\%$, an improvement in accuracy which was offset by the greatly increased computational time required limiting the number of trajectories we could simulate.

The GMC encounter rate is a strong function of both the V_z of the star as well as its mean Galactocentric radius, R. The V_z-dependence arises because the GMCs are mostly located in a thin layer ($|z| < 100$pc) and with increasing V_z the stars will spend less and less time in this layer; reducing the encounter rates. As for the the decrease with R that is because the surface density of GMCs drops sharply with R, even more so than that of stars which have a scale length of ~ 2.5 kpc compared to the GMCs that have a scale length of ~ 1.8 kpc. This dependance is shown in figure 4.2 for the simulation where we used a four armed spiral model with a pattern speed of 20 km/s/kpc (Hou & Han 2014) and a velocity dispersion

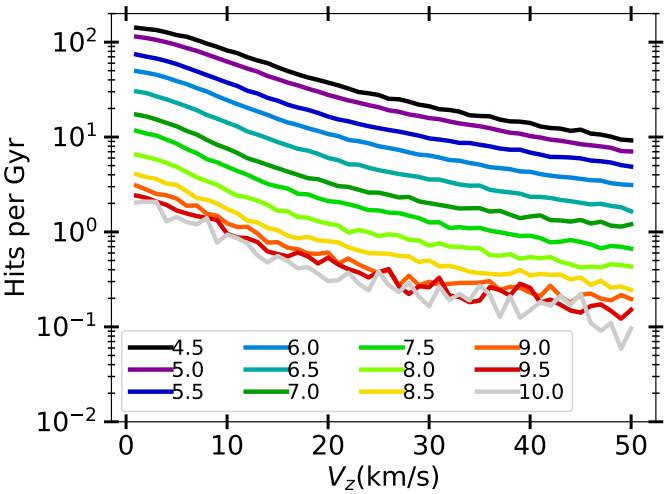

Figure 4.2: The mean number of GMC hits per Gyr as a function of initial V_z. The stars were initialized at different radii using spiral arm model A and then binned and plotted in 500 pc wide bins centred at the values shown in the figure. Velocity dispersion is σ_R = 30 km/s and σ_θ = 20 km/s. These are the in-plane velocity dispersions for stars aged 4 Gyrs, as seen in Nordström et al. (2004) or (Yu & Liu 2018).

corresponding to a 4 Gyr star in the Solar neighbourhood (Nordström et al. 2004). It clearly shows the strong correlations discussed where a star on flat orbit at small R can have hundreds of encounters per Gyr whereas a star on with large R and high V_z can have less than one.

It should be noted that we found no significant differences between the outcomes when using different spiral arm models, even stretching so far as a model with no arms and only a radially distributed homogeneous disk of GMCs showing near identical results.

4.5 Consequences of GMC encounters

The two questions we can quantify following the work in the paper is that of mass accretion and that of being hit by a supernova when passing through a GMC. We showed that the mass accretion is rarely going to be a problem and that the

danger posed by supernovae is far more substantial. Here follows a summary of our findings.

4.5.1 Mass accretion

As a star passes through a GMC, gas is accreted through so called Bondi-Hoyle-Lyttleton accretion, (Hoyle & Lyttleton 1939; Bondi & Hoyle 1944) given by:

$$\dot{M} = \frac{4\pi G^2 M_*^2 \rho}{v_{\rm rel}^3}. \tag{4.14}$$

Where M_* is the mass of a star that passes through a GMC which has density ρ with a velocity of $v_{\rm rel}$. For the density of the GMC we use the mean i.e. the mass divided by the spherical volume which results in the majority of our densities of $n = 10 \sim 100$ cm^{-3}). GMCs have a $R^{-1} - R^{-2}$(Cambresy 1999; Faesi et al. 2016) density profile and the impact parameters from the hit history follow a roughly inverse distribution to that so using the mean gives a reasonable estimate of the average accretion rates. Plugging in our impact velocity distribution gives us accretion rates between 10^{-14} and 10^{-12} M$_\odot$yr^{-1}. This means that there will be no buildup of gas since we know from studies of protoplanetary disks that they have depletion rates exceeding 10^{-10}M$_\odot$yr^{-1}(Clarke et al. 2001). The Sun would likely evaporate the incoming gas at a 6-8 times lower rate than a planet-forming star due to the lower UV flux (Claire et al. 2012). This would still be sufficient to suppress any mass aggregation that could lead to mass extinctions.

As mentioned, GMCs are not smooth structures, but they contain local overdensities known as clumps. If we account for this along with the probability of going straight through the dense central region of a GMC we find that in a few percent of cases the accretion rate will be high enough to trigger a so called "Snowball Earth".

4.5.2 Supernovae

When constructing our GMC model we calculated a star formation rate and found that it matches observations if we assume that all of our GMCs are forming stars. This means that when a star crosses through a GMC there is a probability that it will be hit by a supernova. This probability can be parameterised with the mass of the GMC as it determines how many supernova go off and by the relative encounter velocity as it determines for how long the star is at risk. We map this

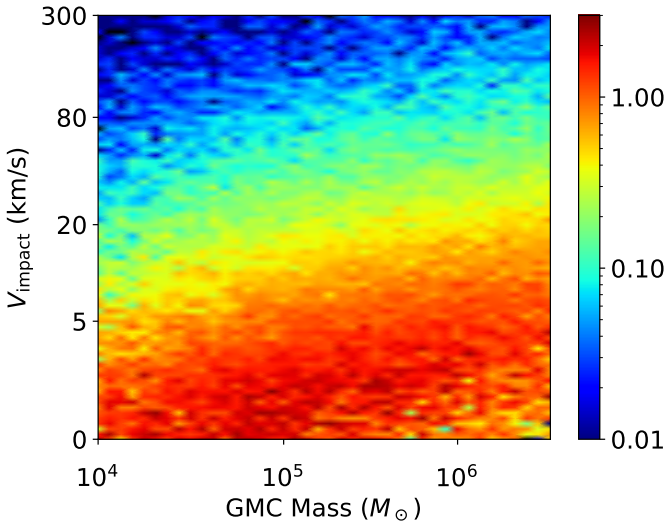

Figure 4.3: The average number of supernovae encounters within 10 pc per GMC crossing as a function of GMC peak mass (equation 4.4) and the velocity of the star when it passes through the surface of the GMC.

probability in the following way:

> A GMC of mass M will make $0.1M$ mass of stars out of which the ones above 8 solar masses end their lives as supernovae; the fraction of these is set by the IMF (equation 4.7). We assume that all stars form when the GMC is 10 Myr old and to the supernovae we assign a detonation time using Zapartas et al. (2017) and position following the prescription of Parker et al. (2014). We then draw a random time and position on the face of the GMC (with the position following a $1/R^2$ distribution), and at each point we draw a line through the GMC and and compute how many 10 pc supernovae spheres this line intersects. We do this for a range of masses and impact velocities which gives us a function that gives the average number of supernovae encountered within 10 pc as a function of GMC mass and impact velocity. We show an example of one such map in figure 4.3.

Inside the GMC, the supernovae are distributed in a fractal manner following the

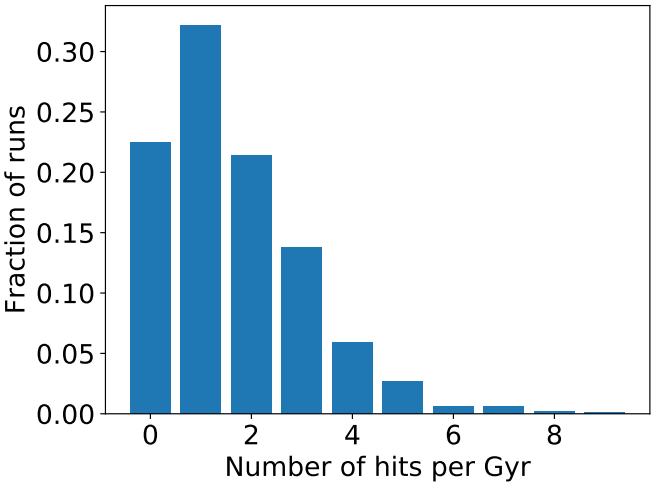

Figure 4.4: The number of GMC hits per Gyr for 1 000 stars on Sun-like orbits where the only difference between them is their initial θ in cylindrical coordinates.

prescription by Goodwin & Whitworth (2004). The fractal distribution is generated by taking a cube and splitting it evenly into 8 sub-cubes. A sub-cube is accepted with probability $P = 2^{-3}$. If accepted, the cube is randomly nudged in a direction to avoid having them all on a lattice and then split further into another 8 sub-cubes which are also accepted with probability $P = 2^{D-3}$. Where D is the fractal dimension and $D = 3$ gives a homogeneous cube, we use $D = 2$ which is a reasonable dimensionality for open clusters. Once a generation of cubes whose number exceeds the number of supernovae required is generated, the cube is pruned into a sphere and a number of sub-cubes are removed to get the specified number of them. If the pruning removes too many sub-cubes the process is repeated. Once this is done, a supernova is put into the center of each remaining sub-cube.

Then we select points on one face of the GMC with random angle and at randomly picked radii, weighted with $1/R^2$ to match the expected hit radius distribution.

4.6 Implications for the Sun

We did a set of simulations where we simulated the orbit of the Sun, in order to determine the Solar encounter rates. The number of encounters per Gyr are shown in figure 4.4. We see that the Sun, which is kinematically colder than the average for stars of its age in the neighbourhood, has a lower average encounter rate of 1.6 per Gyr rather than 2.1 for a Sun-like star in figure 4.2. However, what figure 4.4 shows is the large randomness in the outcome, i.e. the Sun is as likely to have no encounters during 1 Gyr as it is to have 3 or 4; which results in a one sigma encounter frequency of one encounter per 625^{+2700}_{-280} Myrs. If we then consider how often the Sun gets within 10 pc of a supernova under the assertion that two supernovae within the same GMC yields the same result as one, i.e. it would still be one mass extinction, we find an occurrence rate of supernovae within 10 pc of one per $1.25^{+5.25}_{-0.55}$ Gyr.

Such a low rate means that it is very unlikely for any mass extinction to have been caused by nearby supernovae. However, recent work has suggested that the Sun likely formed at a Galactocentric radius of $\sim$5 kpc and later migrated outwards (see e.g. Frankel et al. 2018). This means that a young Sun would have experienced a $\sim$ 100 times nearby supernova rate, in which case Galactic supernovae would most certainly have affected a young Earth.

Bibliography

Alvarez, L. W., Alvarez, W., Asaro, F., & Michel, H. V. 1980, Science, 208, 1095

Antognini, J. M. O. 2015, MNRAS, 452, 3610

Bahcall, J. N., Hut, P., & Tremaine, S. 1985, ApJ, 290, 15

Bailer-Jones, C. 2009, Int. J. Astrobiology, 8, 213

Batygin, K. & Laughlin, G. 2015, Proceedings of the National Academy of Science, 112, 4214

Beech, M. 2011, Ap&SS, 336, 287

Bitsch, B., Crida, A., Libert, A. S., & Lega, E. 2013, A&A, 555, A124

Bondi, H. & Hoyle, F. 1944, MNRAS, 104, 273

Bottema, M., Plummer, W., Strong, J., & Zand er, R. 1965, J. Geophys. Res., 70, 4401

Buchhave, L. A., Bitsch, B., Johansen, A., et al. 2018, ApJ, 856, 37

Cai, M. X., Kouwenhoven, M. B. N., Portegies Zwart, S. F., & Spurzem, R. 2017, MNRAS, 470, 4337

Cambresy, L. 1999, A&A, 345, 8

Carrera, D., Davies, M. B., & Johansen, A. 2016, MNRAS, 463, 3226

Cegla, H. 2019, Geosciences, 9, 114

Chyba, C. F. 1990, Nature, 343, 129

Claire, M. W., Sheets, J., Cohen, M., et al. 2012, ApJ, 757, 95

Clarke, C. J., Gendrin, A., & Sotomayor, M. 2001, MNRAS, 328, 485

Clemens, D., Sanders, D., & Scoville, N. 1988, ApJ, 327, 139

Draine, B. T. 2011, Physics of the Interstellar and Intergalactic Medium (Princeton University Press)

Dyson, F. 1999, Origins of life (Cambridge University Press)

Faesi, C., Lada, C., & Forbrich, J. 2016, ApJ, 821, 18

Federrath, C. & Klessen, R. S. 2012, ApJ, 761, 156

Feng, F. & Bailer-Jones, C. A. L. 2013, ApJ, 768, 152

Ford, E. B. & Rasio, F. A. 2008, ApJ, 686, 621

Frankel, N., Rix, H.-W., Ting, Y.-S., Ness, M., & Hogg, D. W. 2018, ApJ, 865, 96

García-Sánchez, J., Weissman, P. R., Preston, R. A., et al. 2001, A&A, 379, 534

Gillman, M. & Erenler, H. 2008, International Journal of Astrobiology, 7, 17

Goldbaum, N. J., Krumholz, M. R., Matzner, C. D., & Mckee, C. F. 2011, ApJ, 101

Goodwin, S. P. & Whitworth, A. P. 2004, A&A, 413, 929

Güdel, M. 2007, Living Reviews in Solar Physics, 4, 3

Gustafsson, B., Church, R., Davies, M. B., & Rickman, H. 2016, A&A, 593, 19

Heisler, J. & Tremaine, S. 1989, Icarus, 77, 213

Hopkins, P. F., Kereš, D., Murray, N., Quataert, E., & Hernquist, L. 2012, MNRAS, 427, 968

Hou, L. G. & Han, J. L. 2014, A&A, 125, 1

Hoyle, F. & Lyttleton, R. A. 1939, Proc. Camb. Phil. Soc., 35, 405

Hut, P. & Tremaine, S. 1985, AJ, 90, 1548

Innanen, K. A., Zheng, J. Q., Mikkola, S., & Valtonen, M. J. 1997, AJ, 113, 1915

Ito, T. & Ohtsuka, K. 2019, Monographs on Environment, Earth and Planets, 7, 1

Johansen, A., Davies, M. B., Church, R. P., & Holmelin, V. 2012, ApJ, 758, 39

Jurić, M. & Tremaine, S. 2008, ApJ, 686, 603

Kasting, J. F., Whitmire, D. P., & Reynolds, R. T. 1993, Icarus, 101, 108

Kataoka, R., Ebisuzaki, T., Miyahara, H., & Maruyama, S. 2013, New Astronomy, 21, 50

Katz, B., Dong, S., & Malhotra, R. 2011, Phys. Rev. Lett., 107, 181101

Kopparapu, R. K., Ramirez, R. M., SchottelKotte, J., et al. 2014, ApJ, 787, L29

Körtgen, B., Seifried, D., Banerjee, R., Vázquez-Semadeni, E., & Zamora-Avilés, M. 2016, MNRAS, 459, 3460

Kozai, Y. 1962, AJ, 67, 591

Kroupa, P. 2001, MNRAS, 322, 231

Krumholz, M. R., Matzner, C. D., & McKee, C. F. 2006, ApJ, 653, 361

Lada, C. J. & Lada, E. A. 2003, ARA&A, 41, 57

Lambrechts, M., Morbidelli, A., Jacobson, S. A., et al. 2019, A&A, 627, A83

Laskar, J. 1997, A&A, 317, L75

Leitch, E. M. & Vasisht, G. 1998, New Astronomy, 3, 51

Leite, A. C. O., Martins, C. J. A. P., Molaro, P., et al. 2018, arXiv e-prints, arXiv:1812.06796

Li, D., Mustill, A. J., & Davies, M. B. 2019, MNRAS, 488, 1366

Li, D., Mustill, A. J., & Davies, M. B. 2020, MNRAS

Li, W., Chornock, R., Leaman, J., et al. 2011, MNRAS, 412, 1473

Licquia, T. C. & Newman, J. A. 2015, ApJ, 806, 96

Lidov, M. L. 1962, 9, 719

Lieberman, B. S. & Melott, A. L. 2007, PLoS ONE, 2, e759

Lissauer, J. J., Ragozzine, D., Fabrycky, D. C., et al. 2011, ApJS, 197, 8

Lutz, T. M. 1985, Nature, 317, 404

Malmberg, D., Davies, M. B., & Chambers, J. E. 2007a, MNRAS, 377, L1

Malmberg, D., Davies, M. B., & Heggie, D. C. 2011, MNRAS, 411, 859

Malmberg, D., de Angeli, F., Davies, M. B., et al. 2007b, MNRAS, 378, 1207

Marconi, A., Di Marcantonio, P., D'Odorico, V., et al. 2016, in Society of Photo-Optical Instrumentation Engineers (SPIE) Conference Series, Vol. 9908, Ground-based and Airborne Instrumentation for Astronomy VI, ed. C. J. Evans, L. Simard, & H. Takami, 990823

Melott, A. L. & Bambach, R. K. 2013, ApJ, 773, 6

Milaković, D., Pasquini, L., Webb, J. K., & Lo Curto, G. 2020, , 493, 3997

Miville-Deschênes, M.-A., Murray, N., & Lee, E. J. 2017, ApJ, 834, 1

Miyamoto, M. & Nagai, R. 1975, PASJ, 27, 533

Montesinos, B., Eiroa, C., Krivov, A. V., et al. 2016, A&A, 593, A51

Morbidelli, A., Chambers, J., Lunine, J. I., et al. 2000, Meteoritics and Planetary Science, 35, 1309

Mordasini, C., Alibert, Y., & Benz, W. 2009, A&A, 501, 1139

Nakanishi, H. & Sofue, Y. 2006, PASJ, 58, 13

Naoz, S., Farr, W. M., Lithwick, Y., Rasio, F. A., & Teyssandier, J. 2013a, MNRAS, 431, 2155

Naoz, S., Yoshida, N., & Gnedin, N. Y. 2013b, ApJ, 763, 27

Napier, W. M. & Staniucha, M. 1982, MNRAS, 198, 723

Nimura, T., Ebisuzaki, T., & Maruyama, S. 2016, Gondwana Research, 37, 301

Nordström, B., Mayor, M., Andersen, J., et al. 2004, 1019, 989

Ochsendorf, B. B., Meixner, M., Roman-duval, J., Rahman, M., & Evans, N. J. 2017, ApJ, 841, 109

Oort, J. 1950, Bulletin of the Astronomical Institutes of the Netherlands, 11, 91

Parker, R. J., Church, R. P., Davies, M. B., & Meyer, M. R. 2014, MNRAS, 437, 946

Patel, B. H., Percivalle, C., Ritson, D. J., Duffy, C. D., & Sutherland, J. D. 2015, Nature chemistry, 7, 301

Pavlov, A. A., Toon, O. B., Pavlov, A. K., Bally, J., & Pollard, D. 2005, Geophys. Res. Lett., 32, L03705

Pepe, F. A., Cristiani, S., Rebolo Lopez, R., et al. 2010, in Society of Photo-Optical Instrumentation Engineers (SPIE) Conference Series, Vol. 7735, Ground-based and Airborne Instrumentation for Astronomy III, 77350F

Petit, A. C., Pichierri, G., Davies, M. B., & Johansen, A. 2020, A&A, 641, A176

Pineda, J. E., Caselli, P., & Goodman, A. A. 2008, ApJ, 679, 481

Plummer, H. C. 1911, MNRAS, 71, 460

Quillen, A. C. 2011, MNRAS, 418, 1043

Ragusa, E., Rosotti, G., Teyssandier, J., et al. 2018, MNRAS, 474, 4460

Rampino, M. R. 1997, Celestial Mechanics and Dynamical Astronomy, 69, 49

Rampino, M. R. & Stothers, R. B. 1984, Nature, 308, 709

Rauer, H., Catala, C., Aerts, C., et al. 2014, Experimental Astronomy, 38, 249

Raup, D. M. 1985, Nature, 314, 341

Raup, M. D. & Sepkoski, J. J. 1984, PNAS, 81, 801

Raymond, S. N., Armitage, P. J., Moro-Martín, A., et al. 2012, A&A, 541, A11

Raymond, S. N., Mandell, A. M., & Sigurdsson, S. 2006, Science, 313, 1413

Rodhe, H., Charlson, R., & Crawford, E. 1997, Ambio, 26, 2

Roman-Duval, J., Heyer, M., Brunt, C. M., et al. 2016, ApJ, 818, 144

Roman-Duval, J., Jackson, J. M., Heyer, M., Rathborne, J., & Simon, R. 2010, ApJ, 723, 492

Rosolowsky, E. & Leroy, A. 2006, PASP, 118, 590

Rothschild, L. J. & Mancinelli, R. L. 2001, Nature, 409, 1092

Rubincam, D. P. 2016, Icarus, 264, 132

Ruderman, M. A. 1974, Science, 184, 1079

Sagan, C. & Pollack, J. B. 1967, J. Geophys. Res., 72, 469

Schlichting, H. E., Ofek, E. O., Sari, R., et al. 2012, ApJ, 761, 150

Schönrich, R. & Binney, J. 2009, MNRAS, 396, 203

Sellwood, J. A. & Binney, J. J. 2002, MNRAS, 336, 785

Shaviv, N. J. 2002, Physical Review Letters, 89, 051102

Shaviv, N. J. 2003, New Astronomy, 8, 39

Shaviv, N. J., Prokoph, A., & Veizer, J. 2014, Scientific Reports, 4, 6150

Sibthorpe, B., Kennedy, G. M., Wyatt, M. C., et al. 2018, MNRAS, 475, 3046

Sozzetti, A., Casertano, S., Lattanzi, M. G., et al. 2008, in IAU Symposium, Vol. 248, A Giant Step: from Milli- to Micro-arcsecond Astrometry, ed. W. J. Jin, I. Platais, & M. A. C. Perryman, 256–259

Stigler, S. M. & Wagner, M. J. 1987, Science, 238, 940

Stothers, R. B. 1986, Nature, 322, 444

Tanaka, H. K. M. 2006, Atmosph. Sol.–Terrestr. Phys, 68, 1396

Thomas, B. C., Melott, A. L., Jackman, C. H., et al. 2005, ApJ, 634, 509

Thommes, E. W., Matsumura, S., & Rasio, F. A. 2008, Science, 321, 814

Thompson, S. J., Queloz, D., Baraffe, I., et al. 2016, in Society of Photo-Optical Instrumentation Engineers (SPIE) Conference Series, Vol. 9908, Ground-based and Airborne Instrumentation for Astronomy VI, ed. C. J. Evans, L. Simard, & H. Takami, 99086F

Toon, O. B., Bardeen, C., & Garcia, R. 2016, Atmospheric Chemistry & Physics, 16, 13185

Tout, C. A., Pols, O. R., Eggleton, P. P., & Han, Z. 1996, MNRAS, 281, 257

Tremaine, S. 1993, in Astron. Soc. Pac., San Francisco, Vol. 36, Planets Around Pulsars, ed. J. A. Phillips, S. E. Thorsett, & S. R. Kulkarni, 335–344

Vallini, L., Ferrara, A., Pallottini, A., et al. 2016, 14, 1

Valtonen, M. & Karttunen, H. 2006, The Three-Body Problem (Cambridge University Press)

Volk, K. & Malhotra, R. 2011, ApJ, 736, 11

von Zeipel, H. 1910, Astronomische Nachrichten, 183, 345

Whitmire, D. P. & Jackson, A. A. 1984, Nature, 308, 713

Wienen, M., Wyrowski, F., Menten, K. M., et al. 2015, A&A, 579, A91

Williams, J. P. & McKee, C. F. 1997, ApJ, 476, 166

Yabushita, S. 1997, Celestial Mechanics and Dynamical Astronomy, 69, 31

Yu, J. & Liu, C. 2018, MNRAS, 475, 1093

Zapartas, E., de Mink, S. E., Izzard, R. G., et al. 2017, A&A, 601, A29

Zhu, W. & Wu, Y. 2018, AJ, 156, 92

Part II

Research Papers

Paper I

Paper I:
Stellar encounters with Giant Molecular Clouds

G. Kokaia, M.B. Davies (2019)
Monthly Notices of the Royal Astronomical Society, Volume 489, Issue 4, p. 5165-5180

My contribution:

Giorgi Kokaia (GK) had the original idea for this work after reading the thesis (Feng 2013) which was entitled How often do stars on different orbits go through the spiral arms. After writing and performing a number of numerical tests and analyzing them together with his supervisor (Melvyn B. Davies (MBD), they settled on considering GMCs. GK wrote the code for this as MBD helped guide GK through the wide range of literature that had to go into the model. Through discussions and joint analysis of the output, the model was improved upon, bugs ironed out and the final results produced. GK wrote the paper, which was submitted and accepted after making a lot of revisions based on feedback and discussions with MBD.

Monthly Notices of the ROYAL ASTRONOMICAL SOCIETY

MNRAS **489,** 5165–5180 (2019) doi:10.1093/mnras/stz813
Advance Access publication 2019 April 10

Stellar encounters with giant molecular clouds

Giorgi Kokaia★ and Melvyn B. Davies

Department of Astronomy and Theoretical Physics, Lund Observatory, Lund University, Box 43, SE-221 00 Lund, Sweden

Accepted 2019 March 17. Received 2019 February 18; in original form 2018 October 10

ABSTRACT

Giant molecular clouds (GMCs) are believed to affect the biospheres of planets as their host star passes through them. We simulate the trajectories of stars and GMCs in the Galaxy and determine how often stars pass through GMCs. We find a strong decreasing dependence with Galactocentric radius, and with the velocity perpendicular to the Galactic plane, V_z. The *XY*-component of the kinematic heating of stars was shown to not affect the GMC hit rate, unlike the *Z*-dependence (V_z) implies that stars hit fewer GMCs as they age. GMCs are locations of star formation, therefore we also determine how often stars pass near supernovae. For the supernovae the decrease with V_z is steeper as how fast the star passes through the GMC determines the probability of a supernova encounter. We then integrate a set of Sun-like trajectories to see the implications for the Sun. We find that the Sun hits 1.6 ± 1.3 GMCs per Gyr which results in 1.5 ± 1.1 or (with correction for clustering) 0.8 ± 0.6 supernova closer than 10 pc per Gyr. The different the supernova frequencies are from whether one considers multiple supernovae per GMC crossing (few Myr) as separate events. We then discuss the effect of the GMC hits on the Oort cloud, and the Earth's climate due to accretion, we also discuss the records of distant supernova. Finally, we determine Galactic Habitable Zone using our model. For the thin disc, we find it to lie between 5.8 and 8.7 kpc and for the thick disc to lie between 4.5 and 7.7 kpc.

Key words: astrobiology – Sun: general – stars: general – stars: kinematics and dynamics – supernovae: general – ISM: clouds.

1 INTRODUCTION

As stars orbit in the Galaxy they interact with giant molecular clouds (GMC). GMCs are large and massive gas clouds with masses ranging from tens of thousands to several million solar masses with sizes between 10 and 100 pc and there are upwards of 8000 of them in the Milky Way (Miville-Deschênes, Murray & Lee 2017); they are primarily located inside the spiral arms, because that is where the gas can cool to form them (Hou, Han & Shi 2009). Because there are so many of them and because they are so large and massive it is inevitable that stars will interact with them. This interaction can imply two things. If the star passes the GMC at a distance it will be scattered, contributing to the kinematic heating of a star as it ages (Nordström et al. 2004). If it gets so close that it passes through the GMC it will not only be scattered as a whole range of other things can occur during the passage.

Passing through the GMC can potentially be catastrophic for the habitability of a planet orbiting the star as it represents a large deviation from normal environmental conditions. This can lead to a so called mass extinction (large loss of biodiversity) for the following reasons. The GMCs are massive and exert a strong tidal force on a structure such as the Oort cloud (Oort 1950), believed to exist around most other stars (Tremaine 1993). This interaction has been shown to be strong enough to unbind comets orbiting in it (Napier & Staniucha 1982; Hut & Tremaine 1985). These comets could be injected into the planetary system leading to giant impacts (Rubincam 2016). Or, as the star passes through the GMC upwards of an Earth mass of gas can be accreted (Hoyle & Lyttleton 1939). This gas can settle in the upper atmosphere of planets and when doing so can seed rapid cloud formation (Kataoka et al. 2013) or enshroud the upper atmosphere (Pavlov et al. 2005; Nimura, Ebisuzaki & Maruyama 2016), either of these will cause a sharp increase in albedo and can lead to a so called 'Snowball Earth' scenario.

An additional threat is posed by the GMC passage due to them being sites of star formation. Stars that end their lives as core-collapse supernovae are short-lived (<50 Myr, see e.g. Zapartas et al. 2017) and therefore end their lives and explode where or close to where they are born. This means that whilst passing through a GMC a star risks passing near a supernova. There are several ways in which a nearby supernova can be catastrophic for life on the surface of a planet. (1) Assuming the planet has an ozone layer protecting it from high-energy radiation, Beech (2011) shows that a typical 10^{46} J supernova (giving out $\sim 10^{38}$ W of far-ultraviolet (FUV) and X-rays during the initial shock break out for a few minutes) within

★ E-mail: giorgi@astro.lu.se

9 pc can cause mass extinction due to UV and X-ray irradiation of the surface even with the ozone layer absorbing 99 per cent of the radiation. Barring such protection, he places the 'kill radius' at 90 pc. (2) Ruderman (1974) discusses a mechanism in which this protective layer can be destroyed by the formation of nitric oxide (NO) in the upper atmosphere which then will destroy the ozone and cause the UV flux of the host star to cause the mass extinction. Taking the Sun as an example, it has an FUV/X-ray power output of 10^{20} W (Güdel 2007), meaning the irradiation of the Earth will be a factor 10^3 lower than that of the Beech (2011) supernova, however the ozone will take decades to replenish (Thomas et al. 2005) meaning the overall irradiation will be significantly higher as the relative duration differs by a factor of 10^6. For the destruction of the ozone layer to occur, Ruderman (1974) assumes a supernova producing 10^{40} J of X-rays or 10^{43}–10^{44} J of cosmic rays needs to occur at a distance of ∼15 pc. (3) Further, Thomas et al. (2005) showed (in the context of a 2 kpc distant GRB, producing equivalent amounts of FUV and X-rays hitting the Sun as a nearby supernova) how the production of NO can lead to an extinction from an ice age rather than irradiation. The NO will form nitrogen dioxide (NO_2) which will significantly increase the albedo of the planet plunging it into an ice age. Not only that, but the biosphere would also be stressed by nitric acid rain. (4) Similarly, Tanaka (2006) showed that at a distance of 12–15 pc 10^{43} J of cosmic rays can also cause an ice age by seeding cloud formation in the upper atmosphere. Which one of these effects will cause the mass extinction in the event of a nearby supernova is up for debate but it will likely depend on the distance to the supernova and the conditions in which it occurs. These works consider all consider the Sun completely unshielded, however the nearby supernova we will discuss in this paper occur within GMCs. The amount of shielding will depend strongly on what kind of GMC the supernova occurs in and where in the GMC it happens. It is clear that there will be some shielding regardless and for that reason we adopt a 10 pc kill radius.

In this work, we will focus on the destructive effects of a star passing through a GMC or being near a supernova as it detonates. It is important to point out that there is a different way in which one can study the effect of the Galactic environment on the habitability of planetary systems, in particular the effects of cosmic rays. Instead of looking at the cosmic rays originating from a nearby supernova one can look at the integrated flux from a larger number of more distant supernovae and their remnants. Shaviv (2002, 2003) does this by constructing a diffusion model of the Galaxy in which the cosmic ray sources are the spiral arms since that is where nearly all the supernova are found. They find that the cosmic ray flux varies by up to a factor of four between the minima in the interarm region and the maxima when crossing the spiral arm and suggest that this variation could be the cause the historical glaciations observed with some regularity in the geological archive.

The question of how often the Sun passes through a GMC or encounters a nearby supernova was thrust into the limelight when Raup & Sepkoski (1984) saw a periodicity in mass extinctions in the geological record and speculated it could have an extra-Solar origin. For an in-depth review on this topic in particular see Bailer-Jones (2009). More generally, it ties into the discussions of the Galactic Habitable Zone (GHZ). The GHZ is defined as the annular region in which the Galaxy is most habitable and likely to host life. The outer boundary is set by looking at the average metallicity of stars. Gonzalez, Brownlee & Ward (2001) estimate that a metallicity of [Fe/H] $\gtrsim -0.7$ is needed to form Earth-like planets, i.e. planets with mechanisms for interior heat loss, volatile inventory for complex life and sufficient atmospheric retention. The inner boundary is usually set in one of two ways: the first way is to set the boundary where the metallicity gets too high (Gonzalez et al. 2001; Vukotić et al. 2016), because at that point you will also start producing a lot of gas giants (Fischer & Valenti 2005) instead of just rocky planets and the rocky planets you produce will have too high surface gravities to be habitable by organic life. It is known from e.g. Carrera, Davies & Johansen (2016) that a high multiplicity of gas giants cause problems for habitable systems as they destabilize the system. The other way of determining the boundary is to look at supernova rates (Gowanlock, Patton & Mcconnell 2011; Spitoni, Matteucci & Sozzetti 2014; Morrison & Gowanlock 2015), and then calculate how often a star would experience a nearby supernova. One then sets a threshold for the acceptable supernova rate (usually a factor of the nearby Solar supernova rate) and find the boundary. Since both the average metallicity and supernova rate in a region of the Galaxy will change with time one can actually find a time-dependent GHZ such as Lineweaver, Fenner & Gibson (2004).

In this paper, we will determine how often stars pass through GMCs by integrating their orbits and counting how often they coincide. In Section 2, the Galactic potential used for integrating orbits of stars and GMCs will be discussed. We also discuss the spiral arms of the Galaxy and how they are used in the simulations along with how we use Galactic observations of H_2 to synthesize the population of GMCs. Following that we give the results in Section 3. In Section 4, we add supernovae into the GMCs, discuss the implications for the Sun and finish off by determining the GHZ using what we find in this paper together with the methods discussed in papers mentioned above.

2 SETUP OF THE NUMERICAL EXPERIMENT

2.1 Galactic potential

We conduct an experiment in which we follow orbits of stars and GMCs to investigate how often stars on different orbits pass through GMCs, which we from now on will refer to as 'hitting' the GMCs. We do this by integrating them through a Galactic potential. Following Feng & Bailer-Jones (2013), we use a three-component symmetric, analytic Galactic potential given in García-Sánchez et al. (2001). The potential $\Phi_G(R, z)$ is given by

$$\Phi_G = \Phi_b + \Phi_h + \Phi_d, \tag{1}$$

The three components are the halo, bulge, and disc. The halo and bulge are modelled as two spherical Plummer (Plummer 1911) potentials. The equation describing them is shown below in cylindrical coordinates.

$$\Phi_{b,h} = -\frac{GM_{b,h}}{\sqrt{R^2 + z^2 + b_{b,h}^2}}, \tag{2}$$

The disc we model as a Miyamoto (Miyamoto & Nagai 1975) disc, shown below.

$$\Phi_d = -\frac{GM_d}{\sqrt{R^2 + \left(a_d + \sqrt{z^2 + b_d^2}\right)^2}} \tag{3}$$

The above equations are in cylindrical coordinates, meaning R represents the Galactocentric distance and z the distance from the Galactic plane. $M_{d,\,b,\,h}$ is the mass of the disc, bulge, and halo, respectively. b represents the scale length of each component and a_d is the scale height of the disc. The values for these parameters can be found in Table 1.

Table 1. The parameter values used in equations (2) and (3) to construct the potential which is used in the integration (García-Sánchez et al. 2001).

Parameter	Value
M_d	$7.9080 \times 10^{10}\ M_\odot$
M_b	$1.3955 \times 10^{10}\ M_\odot$
M_h	$6.9766 \times 10^{11}\ M_\odot$
a_d	3550 pc
b_b	250 pc
b_d	350 pc
b_h	24000 pc

Table 2. Arm parameters used in equation (4) in order to construct the spiral arms used in the simulation models with four arms. The R_s determine at which radius each arm starts, the θ determines at what angle they start and ψ is the pitch angle, i.e. how non-circular each arm is. Values are from Hou & Han (2014).

	Arm 1	**Arm 2**	**Arm 3**	**Arm 4**
R	3270 pc	4290 pc	3580 pc	3980 pc
θ	38.5°	189.0°	215.2°	320.0°
ψ	9.87°	10.51°	10.01°	8.14°

Some tests were also conducted using other potentials, such as Paczynski (1990) and McMillan (2017). We found that the number of GMC hits changed by a factor of ∼10 per cent for orbits with the same set of initial conditions in the different potentials, overall however the number of hits remain unchanged. This due to the fact that changing potential results in changing the orbit of both stars and GMCs in the same way. More on this in Section 4.4.

2.2 Spiral arms

In the Galaxy, GMCs are primarily located in the spiral arms. In fact, they are one of the best ways to find and trace the arms (Hou et al. 2009; Hou & Han 2014). We do not consider the spiral arm gravitational potential, however to accurately reproduce the Galactic GMC population in our experiment we distribute them in the spiral pattern observed by Hou & Han (2014). These observations are carried out in three different ways: (1) they look for HII regions, because GMCs are regions of star formation and young, hot stars will ionize the surrounding gas, (2) the study includes observations of methanol masers which also trace star formation, and (3) finally, they look for CO emission. CO is a very fragile molecule that cannot survive unless embedded in another, dense gas. It is therefore an excellent tracer for GMCs. To the observations they then fit a logarithmic spiral, shown below

$$\ln \frac{R}{R_i} = (\theta - \theta_i) \tan \psi_i \tag{4}$$

Where R_i is the starting radius, θ_i the starting angle, and ψ_i the pitch angle, i.e. how non-circular the spiral is. θ and R are cylindrical coordinates. The best fit to their observations is a four-armed spiral and the parameters can be found in Table 2. We use these parameters for all our models (as seen in Table 6) except one which uses a three arm fit from the same paper. Parameters for the three armed spiral are shown in Table 7. The GMC distribution generated from Table 2 can be seen in Fig. 1.

The spiral pattern rotates rigidly in the Galaxy, i.e. at a constant angular velocity. This angular velocity is known as the pattern speed.

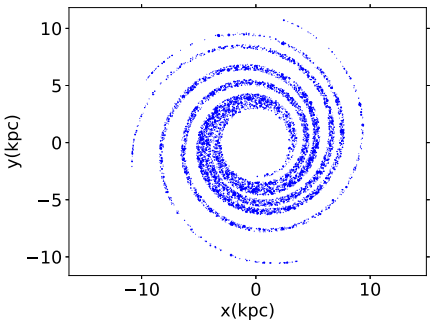

Figure 1. Distribution of GMCs in the Galaxy. The arms are generated using equation (4) and the values in Table 2. The arms range from 3 to 12 kpc with a pattern speed of 20 km s^{-1} kpc^{-1}, measured pattern speeds are given in Table 3. Note that GMC sizes in figure are to scale.

Table 3. Measurements of the pattern speed of the spiral arms in the Milky Way.

Study	Result
Martos et al. (2004)	$\Omega = 20$ km s^{-1} kpc^{-1}
Bissantz, Englmaier & Gerhard (2003)	$\Omega = 20$ km s^{-1} kpc^{-1}
Li et al. (2016)	$\Omega = 23 \pm 2$ km s^{-1} kpc^{-1}
Junqueira et al. (2015)	$\Omega = 23 \pm 1$ km s^{-1} kpc^{-1}
Dias & Lépine (2005)	$\Omega = 24$ km s^{-1} kpc^{-1}
Vallée (2017)	$\Omega = 23 \pm 2$ km s^{-1} kpc^{-1}

Some measured values for this pattern speed are shown in Table 3. This motion around the Galaxy is very different from that of stars that have a fairly flat rotation curve due to the Galactic potential. A flat rotation curve implies a constant circular velocity which means that the angular velocity will be linearly decreasing, so stars at different radii will have a different velocity relative to the spiral arms. The radius at which the angular velocities coincide is known as the corotation radius.

2.3 GMC properties

To model the GMC population in addition to the spiral distribution of the GMCs we also need their remaining spatial distribution (R, z), the distribution of their sizes and densities, their mass function and their lifetimes. For the mass function, we use equation (5) fit to observations by Rosolowsky & Leroy (2006) as shown below

$$\frac{dN}{dM} = (\gamma + 1)\frac{N_0}{M_0}\left(\frac{M}{M_0}\right)^{\gamma}, \quad M < M_0 \tag{5}$$

where $\gamma = 1.53$ and $N_0 = 36$ are constants. M_0 is the maximum mass of 3×10^6 M$_\odot$. The minimum mass is 10^4 M$_\odot$. The resulting mass distribution ends up being fairly top heavy, with 3.5 per cent of GMCs above 10^6 M$_\odot$, accounting for 40 per cent of the total H_2 mass.

A GMC forms slowly as gas falls into the local spiral arm potential and accumulates. It then starts losing mass due to stellar feedback from the newly formed stars as it is leaving the spiral arm potential. We model this behaviour by adopting an age-dependent

Table 4. Measurements of molecular gas in the Galaxy, from Nakanishi & Sofue (2006). Measurements are averages over binned annuli and σ is the standard deviation of a Gaussian distribution fitted to the gas density about the mid-plane.

Radius (kpc)	Surface density ($M_\odot$ pc^{-2})	σ (pc)
3–4	3.5 ± 1.6	37 ± 10
4–5	4.6 ± 2.0	33 ± 5
5–6	3.9 ± 2.0	43 ± 4
6–7	2.8 ± 1.4	37 ± 9
7–8	0.9 ± 0.7	38 ± 13
8–9	0.5 ± 0.4	79 ± 8
9–10	0.5 ± 0.4	78 ± 8
10–11	0.3 ± 0.2	69 ± 8

mass, following the prescription in Gustafsson et al. (2016). GMC mass varies with age as shown below

$$M(t) = \left(-0.25 \times \left(\frac{t-t_0}{10}\right)^2 + \frac{t-t_0}{10}\right) \times M_\mathrm{i} \quad (6)$$

where M_i is the mass drawn from equation (5), $t - t_0$ is the age at time t in Myr. This results in a 40 Myr lifetime where the GMC increases in mass for the first 20 Myr, peaks and then decreases for another 20 Myr. The 40 Myr lifetime is consistent with observations from e.g. Williams & McKee (1997), Vallini et al. (2016), and the shape of the function given by equation (6) is based on simulations from Krumholz, Matzner & McKee (2006) and Goldbaum et al. (2011).

Given a mass drawn using equation (5) and adjusted according to equation (6) we determine the GMC radius by first putting the modelled GMCs in one of three populations. Following the categorization and nomenclature from observations by Roman-Duval et al. (2016), the H_2 gas is put in one of three categories; very dense, dense, and diffuse. They make up 15, 60, and 25 per cent of all the gas, respectively. For the very dense gas, we already have a mass–radius relationship from Roman-Duval et al. (2010) shown in equation (7), this gives the range of gas surface densities between 130 and 300 $M_\odot$ pc^{-2}.

$$\left(\frac{R_\mathrm{GMC}}{1\ \mathrm{pc}}\right) = \frac{1}{229}\left(\frac{M}{1\ M_\odot}\right)^{1/2.36} \quad (7)$$

We then construct two additional mass–radius relationships to get full range of observed surface densities in Roman-Duval et al. (2016) and make sure it is consistent with other observations such as Miville-Deschênes et al. (2017). The two additional mass–radius relationships are shown below. Equation (8) covers the range from 50 to 130 $M_\odot$ pc^{-2}, equation (9) covers 25 to 50 $M_\odot$ pc^{-2}.

$$\left(\frac{R_\mathrm{GMC}}{1\ \mathrm{pc}}\right) = \frac{1}{79}\left(\frac{M}{1\ M_\odot}\right)^{1/2.36} \quad (8)$$

$$\left(\frac{R_\mathrm{GMC}}{1\ \mathrm{pc}}\right) = \frac{1}{28}\left(\frac{M}{1\ M_\odot}\right)^{1/2.36} \quad (9)$$

The radial and vertical distributions are given by H_2 observations by Nakanishi & Sofue (2006). Their observed data are shown in Table 4. We take the radial data and to it we fit a sixth-degree polynomial using the NUMPY module POLYFIT, using this we then generate our own radial distribution with an accept/reject method.

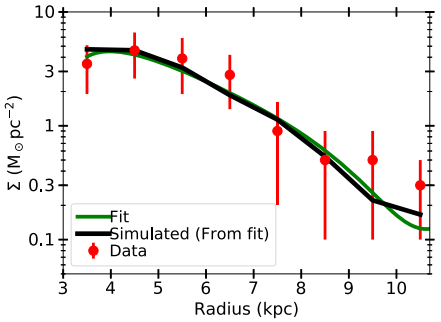

Figure 2. GMC surface density as a function of Galactocentric radius. The black line shows the average GMC surface density measured in our simulations. The distribution of the clouds were generated using the data of Nakanishi & Sofue (2006), which is shown as the red points in the figure (values listed in Table 4). The green line shows the fitted function from which the data are generated, note that the black and green lines diverge at large R, this is due to the small number count of clouds there. Results are also consistent with other work such as Clemens, Sanders & Scoville (1988), Scoville et al. (1987), Wienen et al. (2015), and Roman-Duval et al. (2016).

Table 5. The factors in the sixth-degree polynomial plotted using equation (10) to generate the surface density ($M_\odot$ pc^{-2}) as a function of radius (kpc) in Fig. 2.

n	0	1	2	3	4	5	6
k_n	−106	91	−30	5.2	−0.50	0.0025	-5.3×10^{-4}

The resulting (time-averaged) surface distribution can be seen in Fig. 2 along with the observed data and the fitted polynomial. The fitted constants to the polynomial, shown in equation (10), are given in Table 5.

$$y = \sum_{n=0}^{6} k_\mathrm{n} x^n \quad (10)$$

2.4 Integration of orbits within the Galaxy

We populate our simulation with 6700 randomly generated clouds and keep this number constant; as GMCs reach the end of their life a new one is initiated in the next time-step. At the start of the simulation, the clouds are given a random age and their mass is changed according to equation (6), this results in a total H_2 mass of $\sim 6.5 \times 10^8$ $M_\odot$ in agreement with the total H_2 mass as measured with CO observations by Roman-Duval et al. (2016). The initial conditions are set as follows: the Galactocentric radius, R, is chosen by using the accept/reject method with the function in Fig. 2, z and V_z chosen such that observed scale height from Nakanishi & Sofue (2006) is maintained (values from observations are shown in Table 4).

θ is chosen such that the cloud crosses the analytic line of a randomly chosen spiral arm 20 Myr into its 40 Myr lifetime, i.e. when it is at peak mass. The velocities are chosen such that the GMCs end up on circular orbits. The resulting distribution of GMCs, using model A listed in Table 6 can be seen in Fig. 1. The way we

Table 6. The different sets of parameters for the GMC distributions in the simulation. The pattern speeds in models B and C are calculated and set up such that the corotation radii are at 8 and 6 kpc, respectively, and in the others, we see it is consistent with values from Table 3 shows a list of measured pattern speeds.

Model	Arm properties	Pattern speed ($\mathrm{km\,s^{-1}kpc^{-1}}$)
A	Four-arm spiral	20→corotation: 11.6 kpc
B	Four-arm spiral	28.8→corotation: 8.0 kpc
C	Four-arm spiral	38.6→corotation: 6.0 kpc
D	Three-arm spiral	20→corotation: 11.6 kpc
E	Four-arm spiral with double GMC mass	20→corotation: 11.6 kpc
F	No arms	–

Table 7. Arm parameters used in equation (4) with an alternate, three-armed spiral mode used in model D. This is an alternate fit to the data, presented in Hou & Han (2014). It gives slightly worse fit, but it is interesting to see if any differences are observed using three arms instead of four.

	Arm 1	**Arm 2**	**Arm 3**
R	3220 pc	3430 pc	3100 pc
θ	44.1°	184.5°	210.3°
ψ	9.25°	9.50°	7.80°

model the GMC trajectories and lifetimes (equation 6) results in the width of the spiral arms being a function of the relative difference between the local orbital velocity and the pattern speed of the spiral arms. The difference in width between the inner and outer arms can be seen in Fig. 1. In it the arms are a few kpc wide in the inner region and a few 100 pc in the outer regions.

We also perform the experiments with different sets of spiral arms structures, primarily by varying the pattern speed; the different models can be seen in Table 6. The parameters for the three-armed spiral in model D is shown in Table 7. Model E was to test how the experiment scales with increased total GMC mass. This also implies a higher star formation rate (SFR), which we know the Galaxy had in the past from e.g. van Dokkum et al. (2013) who show that as a function of redshift the SFR changes as $\log(1 + \mathrm{SFR}) = 0.26 + 0.92z - 0.23z^2$, where the redshift at the birth of the Sun (4.5 Gyr ago) is 0.415.

For the stellar trajectories, we initialize 50 000 runs each at eight different radii, $R = (5, 5.5, 6, 6.5, 7, 7.5, 8, 8.5)$ kpc. The polar angle, θ, was randomly, uniformly chosen between 0 and 2π, we do 1000 runs for each integer V_z between 1 and 50 $\mathrm{km\,s^{-1}}$ where V_z is the velocity away from the Galactic plane defined at $z = 0$. Unlike the GMCs, the stars are not on circular orbits. We tested setting the initial velocities with different velocity dispersions σ_θ and σ_R. These are standard deviations in the normal distribution from which V_R and V_θ are randomly generated. These velocities can be characterized as the non-circular component of the orbital velocity, for V_θ we then have; $V_\mathrm{orb} = V_\mathrm{circ} + V_\theta$. The sets of velocity dispersions used were: $\sigma_\mathrm{R} = [20.0, 22.5, 25.0, 27.5, 30.0]$ and $\sigma_\theta = [10.0, 12.5, 15.0, 17.5, 20]$. In most runs, we used $\sigma_\mathrm{R} = 25$ and $\sigma_\theta = 15$ $\mathrm{km\,s^{-1}}$. Corresponding to a 4 Gyr old star in the Solar neighbourhood.

For the integration, we use a leapfrog integrator with variable time-step, where the maximum time-step is $h = 0.1$ Myr. To make sure the scattering during close encounters are well modelled, when

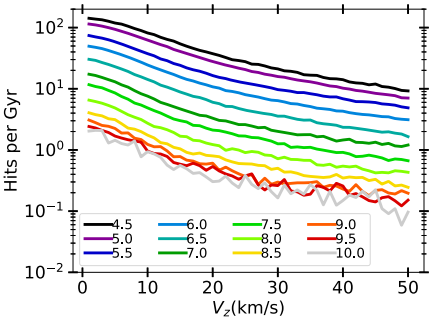

Figure 3. The mean number of GMC hits per Gyr as a function of initial V_z. The stars were initialized at different radii using spiral arm model A and then binned and plotted in 500 pc wide bins centred at the values shown in the figure. Velocity dispersion is $\sigma_\mathrm{R} = 30$ $\mathrm{km\,s^{-1}}$ and $\sigma_\theta = 20$ $\mathrm{km\,s^{-1}}$. This is the in-plane velocity dispersions for stars aged 4 Gyr, as seen in Nordström et al. (2004) or Yu & Liu (2018).

a star gets close to a GMC it is changed as follows:

$$h = \frac{0.1\,(\mathrm{int}(d/R_\mathrm{GMC}) + 1)}{10}\ \mathrm{Myr} \tag{11}$$

where d is separation between star and GMC. We also make sure that the relative velocity of the star to the GMC is always larger than the escape velocity. This because the changing mass and the fact that GMCs can form very close to stars could lead to unphysical encounters. We find that these are very rare and for the few that were found we removed the trajectory for the analysis.

The duration of the integration is 1 Gyr. There are three reasons for choosing 1 Gyr as the integration time. First, it is sufficiently long to complete one revolution around the Galaxy at the outermost radius in the spiral arm rest frame. Second, it is the time-scale for which the static, unchanging Galaxy, and the spiral arm model remains valid (Sellwood & Carlberg 2014). Finally, since we set initial conditions for a range of V_z, this can be viewed as sampling a Gyr snapshot of stars of different ages and different interaction histories with GMCs. This because the GMC interaction will primarily act to drive up the V_z (Sellwood & Binney 2002).

3 RESULTS

We have followed 400 000 stellar trajectories to see how often different orbits hit a GMC, and to remind the reader by this we mean when the star passes through the GMC, i.e. when the distance between the star and the centre of the GMC is smaller than the GMC radius. We find the number of hits depends strongly on the parameters R and V_z which can be seen in Fig. 3. Each line in Fig. 3 represents trajectories with an average radius $((R_\mathrm{max} + R_\mathrm{min})/2)$ binned to 0.5 kpc wide bins. V_z is defined as the velocity away from the Galactic plane at $z = 0$. The decreasing number of hits with increasing V_z is due to the fact that the GMCs are all located in a thin layer, as can be seen in Table 4. With a higher V_z, a star spends less time close to the Galactic plane, as V_z goes up and the vertical oscillation period of the star increases, resulting in less time spent in the GMC layer and fewer plane crossings per Gyr, lowering the probability of hitting a GMC. The R-dependence comes from two

Table 8. Fits using equation (12) which gives the mean number of GMC hits per Gyr at different radii as a function of V_z. The data which it is fitted to is shown in Fig. 3.

Radius (kpc)	A	V_0 (km s^{-1})	C
4.5	159.9 ± 18	13.7 ± 0.38	5.0 ± 1.1
5.0	127.3 ± 12	12.3 ± 0.29	4.7 ± 0.7
5.5	81.2 ± 7.7	11.0 ± 0.23	4.3 ± 0.4
6.0	55.0 ± 3.4	10.9 ± 0.14	2.7 ± 0.16
6.5	33.4 ± 1.9	10.2 ± 0.17	1.7 ± 0.14
7.0	19.1 ± 1.1	9.3 ± 0.21	1.2 ± 0.07
7.5	12.8 ± 0.8	9.1 ± 0.19	0.7 ± 0.06
8.0	7.2 ± 0.8	9.1 ± 0.22	0.4 ± 0.03
8.5	4.5 ± 0.6	9.1 ± 0.25	0.3 ± 0.02
9.0	3.3 ± 0.4	9.1 ± 0.25	0.3 ± 0.02
9.5	2.6 ± 0.4	9.4 ± 0.31	0.3 ± 0.02
10.0	2.3 ± 0.8	8.8 ± 0.55	0.3 ± 0.02

separate factors, first of all the surface density of GMCs goes down with increasing R as can be seen in Fig. 2. The second reason is that at larger R, a star gets to a larger $|z|$ for the same V_z due to the shape of the potential.

We fit an exponential equation (equation 12 below) to each line shown in Fig. 3. We find the lines to be well modelled by the equation and the resulting fits are shown in Table 8

$$N = A \exp\left(-\frac{V_z}{V_0}\right) + C \tag{12}$$

where N is the number of hits per Gyr and C is a constant.

We then fit a single exponential to the number of hits as a function of radius for each V_z and find that in this case the single exponential ($N = A \times \exp(-R/R_0)$) works well. We find the scale length to be 750 pc at low V_z, increasing to 850 pc as it reaches a peak at $V_z = 11$ km s^{-1} and then decreasing towards 800 pc.

3.1 Distribution of the number of hits

We look at how the number of hits are distributed at all radii within a single V_z bin. In Fig. 4, we see how the hits are distributed at all radii for $V_z = 11$ km s^{-1}. 11 km s^{-1} is chosen because it is the velocity at which orbits start getting above the H_2 layer (11 km s^{-1} gives a maximum z of ∼50 pc at 5 kpc). We see a fairly narrow distribution at small radii which widens significantly as the radius is increased. In Fig. 4, we can see that 95 per cent of the stars at 4–5 kpc have a number of GMC hits within a factor of two of the mean. However beyond 8 kpc, we see larger deviations from the mean with a fraction having several times the mean in the number of hits and an even larger fraction (∼20 per cent) with no hits at all during 1 Gyr.

There might be very little difference between having 50 or 100 hits in a Gyr, it all depends on how affected the planet is by the perturbation and how fast it recovers. On the other hand, the difference between zero and three hits in a Gyr could be the difference that allows conditions for life be maintained sufficiently long for it to emerge.

3.2 Kinematic heating, eccentricity, and age

We set the stars on non-circular orbits whilst we approximate GMCs to be on circular orbits (reasonable as they have a low velocity dispersion, see e.g. Gammie, Ostriker & Jog 1991). The stars being on non-circular orbits means that stellar orbits can cross GMC orbits as the stars move radially and in doing so they can collide. One might think that the more non-circular a stellar orbit is, the higher the probability is for collisions as it would cross more GMC orbits. To study the effects of non-circular orbits, we define a Keplerian eccentricity for the stars as $e = (R_{max} - R_{min})/(R_{max} + R_{min})$, where R_{max} and R_{min} are the maximum and minimum radii reached during the simulation. We find that 95 per cent of the stars have $e < 0.11$ and we find no correlation between e and the number of GMC hits. In order to confirm the robustness of this result we do a set of runs in which we give the GMCs a small in-plane velocity dispersion (5 km s^{-1} in R and θ) and we find that the results are the same as if we were to increase the dispersion of the stars.

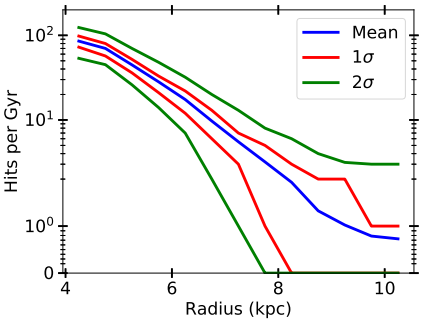

Figure 4. The mean number of hits per Gyr in each mean radial bin with an initial $V_z = 11$ km s^{-1} plotted together with the spread. The 1σ and 2σ indicate the bounds where 68 per cent and 95 per cent of the data is contained, respectively.

The result is intriguing because the eccentricity is a consequence of the kinematic heating a star experiences as it ages and along with increasing the eccentricity, the kinematic heating also increases the V_z. Since the eccentricity appears to have no effect on the number of GMC hits it means that we can keep the in-plane velocity dispersion constant, use a range of V_z and in doing so test stars at different ages. Therefore, as a star ages its hit frequency with GMCs goes down. Let us take a typical star in the Solar neighbourhood as an example. In the Solar neighbourhood, the vertical age–velocity dispersion relation for stars 1–8 Gyr old is $\sigma_z \in [9.3, 23.5]$ km s^{-1} (Nordström et al. 2004). This σ_z gives a mean $|V_z| \in [7.7, 19.4]$ km s^{-1}. Using equation (12), we see that a star with an average heating history in the Solar neighbourhood decreases its hit rate by a factor of 1.6 as it ages from 1 to 8 Gyr.

3.3 Radial migration

The radial dependence on the number of hits per Gyr is strong. The strength of the gradient becomes particularly important when the radial migration of stars is considered, a process in which stars can change their guiding radius without becoming more eccentric due to interactions with spiral arms (Sellwood & Binney 2002). The reason this is important is because more stars have been formed at 5 kpc compared to 8 kpc and perhaps more importantly, due to the Galaxy forming 'inside out' (Martig, Minchev & Flynn 2014) stars

started forming earlier and with a higher metallicity at smaller radii. Some of these would have migrated outwards to a region in which the potentially habitable planets orbiting them are significantly less perturbed by GMCs, e.g. a migration from 5 to 8 kpc along with a heating in V_z by 12 km s^{-1} implies the hit rate lowering by a factor of ∼100. The stars that formed early on with a high metallicity and migrated outwards when they were young are likely the first planets on which life would have developed in the Galaxy.

3.4 Trajectories with zero hits

In Fig. 4, we see that after a certain radius there is a fraction of trajectories that experience no GMC hits during 1 Gyr. A natural question to pose when seeing this is; are there trajectories that *never* hit GMCs? Such trajectories would always go above/under the spiral arms and in doing so never hit the GMCs (perpetual missers). One can also make an intuitive argument against them, for perpetual missers to exist the azimuthal frequency must equal an integer times the vertical oscillation frequency because then if it misses all the arms during one revolution it will do so next time as well. As a star orbits it changes radius and therefore the azimuthal and vertical oscillation frequency changes. They do not change in the same manner and thus no perpetual missers can exist. To check this, we reran the missers for another Gyr and found that at a given R and V_z the same fraction of the missers remained missers as had been the original fraction of missers. Redoing this a few times, we find that eventually all stars hit a GMC at inner radii (< 8 kpc) where the GMC density is higher. At larger radii, there is a small subset of orbits (∼1 per cent) that avoid hitting GMCs yet get scattered to such high V_z that they can avoid hitting GMCs for 10 Gyr, essentially making them perpetual missers. These kinds of orbits are discussed further in Section 4.2.

3.5 Different spiral arm models

As shown in Table 6, we tested a few different models for the spiral arms to see if any difference in the number of hits was observed. For every model except E (in which the number of GMCs are doubled), there was no difference in the overall rates. For E it was as expected, doubling the number of GMCs doubled the number of GMC hits. However, this is not fully representative of what really happens since collisions between GMCs and their subsequent mergers were not considered which at this high a density becomes relevant. So to answer what the mass scaling really looks like we need a more realistic treatment of the GMC dynamics.

There was something interesting observed in model C (corotation at 6 kpc). Even though the mean number of hits for the trajectories were the same as in model A at all locations and for all V_z. When looking at the distribution in time for the hits at 6 kpc we found that nearly all hits happen at one or two intervals of time. This happens due to how our GMC trajectories are defined, near corotation the spiral arm will be much more narrow which makes it much more dense in GMCs. Once a stellar trajectory gets close to the arm it will stay there for a long time since the relative velocity is so low and get hit a lot of times. The same effect was not observed in model B (corotation at 8 kpc), because there are so few hits for each trajectory at and around 8 kpc. The fact that nothing happens even when we artificially increase the density of the arms like this has implications for when discussing the periodicity of mass extinctions on Earth and ascribing it to spiral arm crossings. We find the same thing as Feng & Bailer-Jones (2013); for most spiral arm crossings at 8 kpc nothing happens.

4 DISCUSSION

4.1 Putting supernovae in the GMCs

An extension of our model is to also use it to calculate how often a star passes near a supernova as it explodes. The lifetime of stars that end their life as a core-collapse supernovae ($M_* \gtrsim 8$ M$_\odot$) is about the same as a GMC lifetime (see e.g. Zapartas et al. 2017). This means that nearly all core core-collapse supernovae explode inside or near the GMC in which they are formed; this has been confirmed observationally by Gao et al. (2001). For this reason, we can calculate the probability of a star encountering a supernova when a GMC is hit, apply this to the simulated GMC hit history of our stars and find the probability of being within a certain distance of a supernova when it explodes.

We calculate the probability of a star being within 10 pc of a supernova when it explodes. The mechanisms in which a supernova can cause a mass extinction was discussed in the Introduction, they are: direct irradiation (Beech 2011), destruction of ozone layer and consequent death by Solar radiation (Ruderman 1974), triggering an ice age by increasing albedo by forming NO_2 in upper atmosphere (Thomas et al. 2005), and triggering an ice age by having cosmic rays seed cloud formation (Tanaka 2006). Which of these mechanisms will be dominant is unclear and it will likely depend on the supernova itself along with the environment in which it happens. The distances for which the supernova can cause mass extinctions is up to 15 pc, however these distances are derived assuming an isolated Sun. The supernova in our simulations go off inside GMCs and a star inside a GMC will be shielded by the gas. How much it is shielded will depend on what kind of GMC it occurs in and the location in the GMC. Due to this uncertainty, we adopt a 10 pc kill radius in our experiment. From now on in this paper when we refer to being affected by a supernova we mean being within 10 pc of it when it explodes.

We do a Monte Carlo simulation in which we draw trajectories within a range of measured hit velocities randomly through GMCs over the range of masses and sizes included in the model. As the star passes through the GMCs supernovae are detonated and we count how many of them are within 10 pc and get the probability of a supernova affecting the star. A detailed description of the Monte Carlo simulation follows in the section below.

4.1.1 Supernovae during GMC passages

The number of supernovae per GMC is determined by the amount of gas converted to stars. We take all the GMCs to have a star-forming efficiency of 10 per cent, consistent with recent observations such as Ochsendorf et al. (2017). Once we know how much gas is being made into stars we draw stars from a Kroupa (2001) initial mass function (IMF) shown below:

$$\frac{\mathrm{d}N}{\mathrm{d}M_*} = C_\alpha \, M_*^\alpha \tag{13}$$

where C_α is a constant dependent on α chosen such that the function is continuous and

$$\alpha = \begin{cases} -0.3, & 0.01 < M_*/M_\odot < 0.08 \\ -1.3, & 0.08 < M_*/M_\odot < 0.5 \\ -2.3, & 0.5 < M_*/M_\odot < 100 \end{cases} \tag{14}$$

Once stars have been drawn to reach 10 per cent of the total GMC mass, we stop drawing additional stars. Using the Kroupa IMF results in one in 300 stars being above 8 solar masses, or; for every

100 $M_\odot$ of stars formed we get one supernova. At this point, we can do a reality check of our model by calculating what SFR we end up with under our assumptions and comparing it to observations. Taking a total H_2 mass of 6.5×10^8 $M_\odot$ with 40 Myr lifetime of GMCs during which 10 per cent of their mass is converted to stars we end up with an SFR of 1.64 $M_\odot\,yr^{-1}$. This agrees well with observations; Licquia & Newman (2015) find an SFR of 1.65 ± 0.19 $M_\odot\,yr^{-1}$.

The supernovae are spatially distributed within the GMC in a fractal manner following the prescription by Goodwin & Whitworth (2004). To each supernova we then assign a detonation time, determined by their mass with the delay time distribution given in Zapartas et al. (2017). We treat all the star formation in the GMC as occurring instantly when the GMC is 10 Myr old.

The fractal distribution is generated by taking a cube and splitting it evenly into eight sub-cubes. A sub-cube is accepted with probability $P = 2^{D-3}$. If accepted, the cube is randomly nudged in a direction to avoid having them all on a lattice and then split further into another eight sub-cubes who are also accepted with probability $P = 2^{D-3}$, where D is the fractal dimension and $D = 3$ gives a homogeneous cube, we use $D = 2$ which is a reasonable dimensionality for open clusters (Parker et al. 2014). Once a generation of cubes whose number exceeds the number of supernovae required is generated, the cube is pruned into a sphere and a number of sub-cubes are removed to get the specified number of them. If the pruning removes too many sub-cubes the process is repeated. Once this is done, a supernova is put into the centre of each remaining sub-cube.

We test a large range of relative velocities, we generate trajectories with velocities of 1–200 $km\,s^{-1}$ isotropically crossing through the GMC, averaging over the impact parameters observed in the simulation. We then draw a time from a randomly uniform distribution between 0 and 40 Myr to also average over potential ages. Then, we check how often the trajectory is within 10 pc of a supernova as it explodes. We treat the expansion of the ejecta and the speed of light as infinite which is a reasonable approximation given typical relative speeds. This generates a function of GMC mass and crossing velocity giving an average number of supernovae per crossing. The average number of hits go up with GMC mass and go down crossing velocity. The decrease with velocity is non-linear as can be seen in Fig. 5. The average number of supernovae a star is affected by does not go up sharply with GMC mass as one might have expected. This because the GMC density goes down with increasing mass as one can see in equations (7)–(9), resulting in the supernova distribution getting sparser.

4.1.2 Supernova results

Having determined the average number of supernovae a star is affected by when a GMC is hit we can take the masses and impact velocities from the trajectories described in the previous section and calculate how many supernovae they would have been affected by during 1 Gyr. Fig. 6 shows how many supernovae a star is affected by during 1 Gyr for different trajectories. The results look similar to what we see in Fig. 4, however there is one key difference. The fall-off with V_z is larger because not only does it reduce the probability of hitting a GMC, but it also increases the velocity relative to the GMCs and in doing so it reduces the probability of being affected by a supernova because the star spends less time within 10 pc of the potential supernova. It is important to note that quite a bit of information is lost when using the mean because the distribution is quite lopsided. In the majority of GMC crossings,

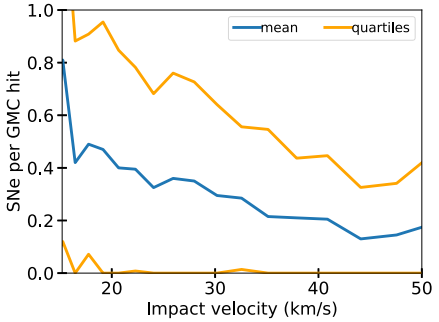

Figure 5. The average number of supernovae a trajectory is affected by when hitting the most common type of GMC, i.e. a 8×10^5 $M_\odot$ dense GMC. The x-axis starts from the escape velocity of the cloud as slower hits than that are not possible and the noise in the function is due to the inherently stochastic process in which it is generated.

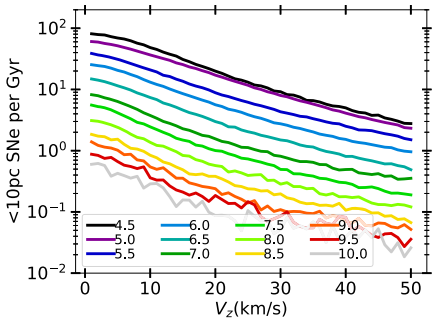

Figure 6. The average number of <10 pc supernovae affecting a star during 1 Gyr as a function of initial V_z. The figure was produced by taking the results of the procedure described in Section 4.1 and applying it to the data plotted in Fig. 3.

the star is not affected by any supernovae. Due to the fractal and lumpy distribution of the supernovae not only does the trajectory have to cross through the GMC at the right time, but also in the right place. When this happens the star is affected by several supernovae per crossing. So we can ask a different question; when a GMC is hit, what is the risk of being affected by at least one supernova? We take the distributions calculated in the previous subsection but now when determining the function we do not allow more than one supernova per crossing. The resulting risk of being affected by a supernova is shown in Fig. 7. In this we see what we expect in that the risk of being affected by a supernova goes down with V_z since the relative velocity increases and we also see that the risk ranging between 0.2–0.3. If we just take the number of supernova affecting the star per GMC hits we find it to be 0.4–0.5.

The median GMC hit mass is large at 8×10^5 $M_\odot$, this has a consequence for the probability of being affected by a supernova. The large mass means that the star accelerated from a few up to almost 10–15 $km\,s^{-1}$ depending on the geometry and initial relative

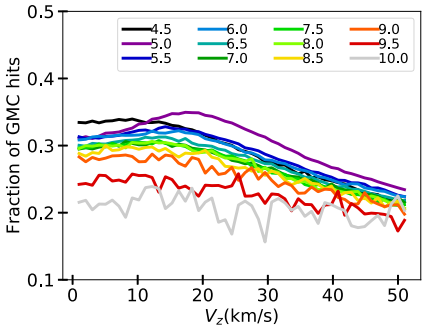

Figure 7. The fraction of GMC hits at different mean radii and initial V_z that result in at least one supernova affecting a star within 1 Gyr.

velocity of the GMC hit. The resulting effect is a quicker passage through the GMC. How many supernovae the star is affected by during a passage is a dependent on velocity as can be seen in Fig. 5. So an increase in velocity by $\sim$10 km s^{-1} can significantly lower the probability of being affected by a supernova. This means the probability of being affected is enhanced in lower mass GMCs, compensating for the fact that they produce fewer supernovae.

4.2 Testing with Solar parameters

To find the rates for the Sun, we use the Solar orbital parameters as determined by Dehnen & Binney (1998) to initialize a set of runs. The orbital parameters given as U, V, and W are the peculiar velocities of the Sun defined as; the deviation from the local standard of rest along the Solar orbit, radially inwards to the Galactic centre and away from the Galactic plane towards the position of Sun, respectively. They are $[(U, V, W) = (10.0 \pm 0.35, 5.23 \pm 0.65, 7.17 \pm 0.38)$ km s^{-1}], they are lower than an average 4.5 Gyr old star for which the average peculiar velocities are (23, 16, 11) km s^{-1}. (Nordström et al. 2004). Whilst the non-circular component of the velocity has little to no effect on the hit rate of GMCs, it will affect the supernova probability as it increases the relative velocity of the hit.

Using the Solar values of peculiar velocities, we initialize 1000 trajectories at randomly selected θ at 8 kpc, and the velocities are given small differences that are drawn from the Gaussian errors shown above. Then, we see how often a Sun-like trajectory will hit a GMC and be affected by a supernova. Fig. 9 shows the results from using a Sun-like orbit. In it, we see that the Sun will hit an average of 1.6 ± 1.3 GMCs per Gyr, or, one GMC every 625^{+2700}_{-280} Myr. The deviation in 1.6 ± 1.3 comes from fitting a Poisson distribution to the number of hits per Gyr, seeing it matches and then taking the Poisson standard deviation; $\sqrt{\lambda}$ where λ is the mean. Then, 625^{+2700}_{-280} Myr is simply its inverse. We could apply the supernova function from Section 4.1 directly, however due to the Sun's low peculiar velocity it passes through GMCs much more slowly. Therefore, it is affected by at least one supernova during nearly half (47 per cent) of the hits. It should be noted that due to the slow hits the Sun is even more prone to multiple supernova per GMC hit, if we were to look at the average rather than the risk we find 0.9 supernova affecting the Sun on per GMC hit. This means that when the Sun experiences a nearby supernova it more often than not experiences multiple supernovae in a short time period. So if we just look at the average, we find that the supernova occur once every 667^{+2500}_{-240} Myr, however if we correct for the spatial and temporal clustering by assuming that two supernovae within a few Myrs is as bad for habitability as one we instead find supernova occurring once every $1.25^{+5.25}_{-0.55}$ Gyr.

However, there is a tail to the distribution that does not arise from just the stochasticity of the hit probabilities. We looked closer at this by doing a 10 Gyr integration for the Sun-like runs. Fig. 10 shows the time until the first GMC hit for all the Sun-like runs, in it we see the tail ($\sim$1 per cent of the runs), these are runs that get scattered to high V_z without actually hitting a GMC and in doing so it makes it possible for them to avoid hits for $>$5 Gyr. In the figure we see two lines, one for model A and one for model E. This further exemplifies that the spiral arm model does not matter for the results.

Our average time between nearby supernovae affecting the Sun differs from some of the reported values [such as Ellis (1995) – 243 Myr, Tanaka (2006) – 100 Myr or Sørensen, Svensmark & Jørgensen (2017) – 183 Myr]. The primary reasons for the difference is that they use the radial distribution of stars or the local stellar density in their calculation which we argue below is not an accurate way of calculating the probability of supernova occurring nearby. Supernovae in our Galaxy model follow the distribution of the GMCs, because that is where star formation and thus SNII occur. The radial surface density distribution of GMCs and stars are different. The surface density of stars follow an exponential with a 2.6 ± 0.6 kpc scale length (Bland-Hawthorn & Gerhard 2016). The molecular gas density decreases rapidly at first, then it plateaus between 3–5 kpc and then continues rapidly to fall off (as seen in Fig. 2). The fall-off after the plateau we find to follow an exponential with a scale length of 1.73 kpc in our simulation with data from Nakanishi & Sofue (2006). One can fit an exponential to the H_2 distribution as a whole and then one ends up with a scale length of $\sim$2 kpc (Miville-Deschênes et al. 2017). Naively one might assume that the two distributions should follow each other as stars form from the gas, however stars are on average moved outwards to larger radii due to radial migration whereas the tendency for the gas is the opposite (Sellwood & Binney 2002).

We investigate this difference by distributing the GMCs following the stellar surface density and then redo the simulation with $\sigma_R = 25$ km s^{-1} and $\sigma_\theta = 15$ km s^{-1}. Fig. 8 shows the resulting number hits for a nearly flat orbit ($V_z = 1$ km s^{-1}) using the two different radial distributions of GMCs. The figure shows a higher hit rate for the gas distribution further in which then crosses over at 6 kpc and has a lower hit rate further out, resulting in a factor of $\sim$4 difference at the Solar circle. The supernovae being more centrally concentrated is also consistent with recent observational findings by Green (2015).

It should also be noted that our Galactic supernova rate is lower than the previously mentioned work for two reasons. First of all our model is limited to looking at core-collapse supernova. Second, is that our supernova rate is more in line with up to date estimates of the Galactic supernova rate (Li et al. 2011).

Nearby SNIa could be more frequent than core-collapse supernova as they follow the stellar distribution and make up 25 per cent (Li et al. 2011) of the Galactic supernovae. We can estimate the time between nearby SNIa by taking the numbers derived in other work in which nearby supernovae are determined by looking at stars and multiplying them by four. This gives 732, 400, and 972 Myr. Those numbers are very similar to and well within the uncertainty range of our first result (664 Myr) and all of them are smaller than our second one (1.28 Gyr). If we consider the assertion of Gowanlock et al. (2011) that SNIa are disruptive for planets they would certainly

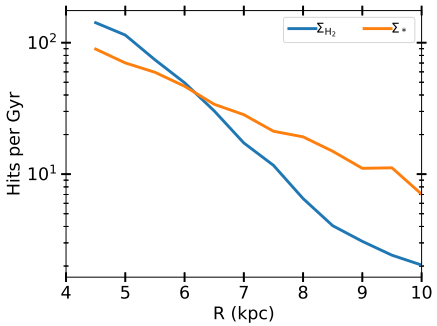

Figure 8. The number of hits as a function of radius for stars with initial $V_z = 1$ km s^{-1}. The blue line shows the result when using the radial distribution of the molecular gas, whereas the orange line shows the result for when using a stellar exponential radial distribution. We see here that the gas and therefore the SNII are more centrally concentrated than the stars and therefore the SNIa. We chose to do the comparison at the lowest V_z, we test for since when local supernovae rates are calculated, motion in the z-direction often is ignored.

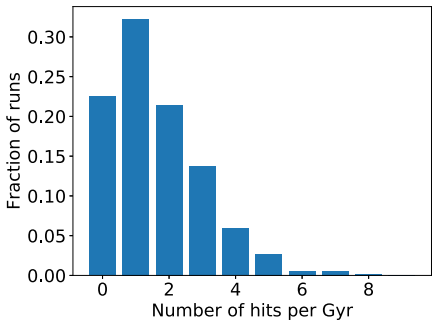

Figure 9. The number of hits per Gyr for a set of 'Sun-like' runs. I.e. starting the trajectory at 8 kpc and giving it the non-circular velocity components from Dehnen & Binney (1998). The difference between each run being the angle at which the trajectory starts.

be the bigger threat regardless of model. That assertion was based on the absolute magnitude of the different class of supernovae and as we have discussed previously it is the FUV/X-ray luminosity that matters. Observations by *Swift* (Immler et al. 2006; Modjaz et al. 2009) indicate that even though SNIa are visually brighter than core-collapse supernovae, their luminosity in the shorter wavelengths are comparable and even pointing to the core-collapse being slightly brighter. For that reason, we believe the risk posed by the different kinds of supernovae to be equal.

4.2.1 *Matching the geological record*

There is geological evidence of two supernovae going off within 30–100 pc of the Sun 1.5–3.2 and 6.5–8.7 million years ago (Knie et al. 2004; Wallner et al. 2016; Ludwig et al. 2016; Hyde & Pecaut

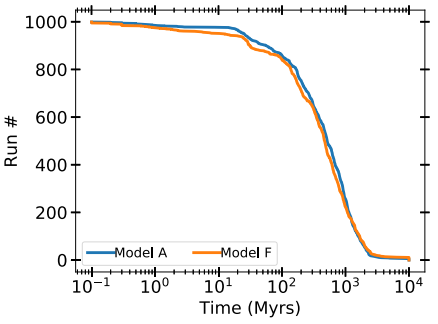

Figure 10. The time until the first GMC hit for each Sun-like trajectory in an extended, 10 Gyr, simulation. In the bottom, there is a subset of runs that never hit a GMC, this is because they get scattered to such a high V_z that the hit probability gets sufficiently low for them to avoid hits for the full 10 Gyr.

2018). This is determined by looking at deep sea cores, where one finds deposits of ^{60}Fe which can only exist on Earth if newly formed as it has a 2.6 Myr half-life. The conclusion is that it comes from supernovae and by looking at the amount of ^{60}Fe one can estimate the distance to the supernovae.

Our model should be able to reproduce the geological record in one of two ways, either by encountering two separate GMCs between the arms and being hit by a supernova from each of them. Or, by being hit by two separate supernovae from a single GMC. From the GMC maps of the spiral arms in Hou & Han (2014), we know that the Sun is currently between spiral arms, and in our model we do not have any GMCs there. To be able to draw conclusions about the Sun's current location in the Galaxy, we use both models A and F (Table 6) with a key difference. The difference is that we do two runs, one in which we check when the trajectory gets within 100 pc (or is inside) of any GMC and one in which we check when the trajectory gets within 30 pc (or is inside) any GMC. Then given the encounter history, we calculate the probability of encountering two supernovae within 5 Myr of each other. With a caveat; the dating in the geological data has a $\sim$1 Myr uncertainty, therefore we stipulate that the supernovae hits on passage have to take place with at least 1 Myr separation in time. Neither of the GMC distributions represent the current GMC distribution around the Sun, however by interpolating between what we see in the different models we can draw conclusions about the Sun. To find the supernova history we redo the procedure described in the previous section but rather than using a range of masses and velocities, we use the ones we find in the simulation. Also, instead drawing trajectories through the GMC we draw them through 30/100 pc spheres centred on the GMC if the GMC is smaller.

In Fig. 11, the number of supernovae one finds if one looks at a randomly chosen 5 Myr timespan for the 30 and 100 pc runs in the different models is shown. We see that it is 8 ± 1.3 and 6.9 ± 0.8 times more likely to have come from the 100 pc case in models A and F, respectively. Which is slightly less than what one would expect from simple geometry. What we also see in model A is an overproduction of supernova, it becomes 32 per cent more likely to have three supernovae rather than two in the 5 Myr timespan. This is likely due to having 37 per cent of cases have supernovae

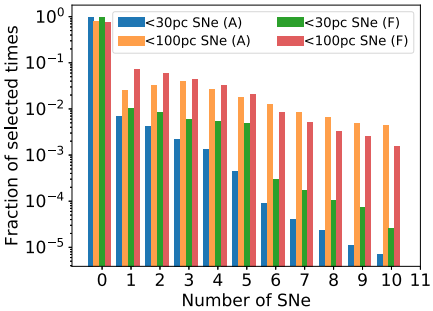

Figure 11. The distribution of the number of supernovae found when randomly picking a 5 Myr interval. In it the result using models A and F (Table 6) are shown.

from more than one GMC with model A compared to 24 per cent with model F. This means that our model reproduces the geological record if the Sun is currently in an environment with a higher GMC density than randomly spread in a disc, but lower than that of the spiral arm. That is consistent with being a spur and therefore the observations, and as a consequence of this we can say that our model is consistent with the geological record and the observed spiral structure around the Sun. As for the distance to the supernovae, it is clear that we favour more distant supernovae, however it must be noted that if we relax our one supernova per Myr criterion we see a higher multiplicity in supernova encounters per passage. This means that two distant supernova can easily go off within such a timespan as to be indistinguishable from a single, nearer supernova. For this reason, along with the low percentages of supernovae we see from different GMCs we favour the two supernovae having come from the same star-forming region. The fact that it is not likely overall to have any supernovae during the 5 Myr interval is not a problem as we randomly draw from all times in Fig. 11, this includes times when not located near spiral arms. Since the Sun is currently located in the local spur we can disregard the high probability of no supernovae.

Additionally, we also tested model B (corotation at 8 kpc). When at corotation and whilst being located in the local arm/spur we see much higher multiplicity of supernovae. If one supernova is observed we expect to see an order of magnitude more supernovae in the following 5 Myr compared to the homogeneous case. Therefore, we claim that it is unlikely we are at corotation as suggested by Junqueira et al. (2015).

However, it should be stressed that to fully understand the history of the Sun it is necessary to investigate all aspects and in particular to utilize the geological record when possible such as the record presented in e.g. Shaviv (2003) and Shaviv, Prokoph & Veizer (2014) where they look at cosmic ray tracers in iron meteorites and fossils, respectively. This is however outside of the scope of this paper, but can be explored in future work as an extension of our model.

4.2.2 *Stripping the Oort cloud*

As the Sun passes through a GMC it will feel the tidal force being exerted upon it. The Oort cloud (Oort 1950), which is a cloud of comets surrounding the Sun extending out to ∼1 pc, is due to its size very susceptible to tidal disruption. Previous work on Oort cloud depletion due to tidal interactions have been done, e.g. Napier & Staniucha (1982) and Hut & Tremaine (1985). These two works use different methods and arrive at very different survival fractions of the Oort cloud, for this reason we will look closer at them and see how their results would have changed given the results from our model of the GMC hit history.

Napier & Staniucha (1982) calculate their depletion by integrating a set of Solar trajectories as they pass through a GMC. Where they use $5 \times 10^5 M_\odot$ as a typical GMC mass where the GMC consists of 25 sub-particles of $2 \times 10^4 M_\odot$. They surround their Sun with 33 000 particles representing the Oort cloud and count what fraction of them are stripped away at each passage. The fraction removed is calculated for a range of velocities, which means that we can take the fractions and interpolate between them to calculate the depletion given our hit history. We have different encounter histories for the lifetime of the Sun (4.5 Gyr). They assume 14 GMC hits, and we find the average number of hits during 4.5 Gyr to be 7. They assume a typical encounter velocity of 20 km s^{-1}, whilst in our runs we determine the typical velocity to be 15 km s^{-1}. As an approximation when using their results to calculate the survival fraction we will use their cloud mass ($5 \times 10^5 M_\odot$) which is slightly lower than the typical cloud mass encountered in our simulation ($8 \times 10^5 M_\odot$) since it will not affect the outcome significantly. Since slower encounters remove a larger fraction of comets we end up with a similar survival fraction to theirs despite having only half as many encounters; we find a survival fraction of 2×10^{-3} compared to theirs of 1.5×10^{-3}. The depletion rate is proportional to the number of comets at a given time so to calculate the survival fraction the depletion rate is integrated over time. For this reason we can, much like with radioactive decay, calculate a half-life for the Oort cloud. Doing that we find that a survival fraction of 1.5×10^{-3} corresponds to a half-life of 480 Myr and 2×10^{-3} corresponds to a half-life of 510 Myr.

Hut & Tremaine (1985) do an analytical calculation of the Oort cloud depletion by GMCs. The work is based on their previous work on disruption of wide binaries by GMCs in the Galactic field (Bahcall, Hut & Tremaine 1985) in which they derive an equation for the half-life of binaries due to GMC interaction. The same equation is used (Hut & Tremaine 1985, equation 7) to estimate the half-life of the Oort cloud. They estimate the half-life to be 2.7 Gyr. We do the same thing with Hut & Tremaine (1985) and use their method with numbers from our model and from newer observations. The estimation is dependent on seven factors, four of which we can extract from observations and our simulation (ρ_0, f_z, f_c, f_p in equation 7) and the remaining three are all dependent on powers of the velocity dispersion of the encounters. The velocity dispersion we find is 15 km s^{-1}, using that instead of their value of 22 km s^{-1} results in a half-life of 680 Myr (survival fraction of 10^{-2}).

The half-lives calculated, using our numbers and applying it to their methods, are similar. This does not however mean that it is the definitive answer of how depleted the Oort cloud is; what this simple exercise has shown is how sensitive the depletion fraction is to the relative velocity of the encounters. The velocities we find have a wide distribution and we have also shown that the number of encounters vary enormously; taking these two facts into account we can derive the ranges of half-lives shown in Fig. 12. Fig. 12 implies that some Sun-like stars will have nearly pristine Oort clouds (few and fast encounters giving a long half-life) and some have very depleted Oort clouds (many slow encounters giving a short

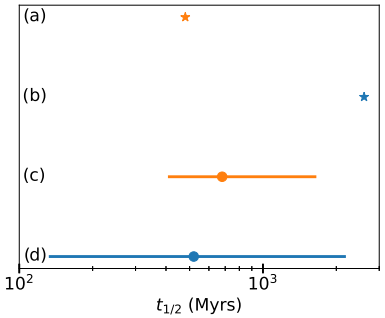

Figure 12. The half-life of the Oort cloud computed in four different ways: (a) the half-life of the Oort cloud from Napier & Staniucha (1982), (b) the half-life of the Oort cloud from Hut & Tremaine (1985), (c) the mean half-life and the 80 per cent interval calculated by taking the distribution of the number of GMC hits and hit velocities in our model and then interpolating in the results of Napier & Staniucha (1982), and (d) the mean half-life and the 80 per cent interval calculated by taking the distribution of GMC hit velocities in our model and applying those together with new observations to equation (7) in Hut & Tremaine (1985).

half-life). This has implications for both the past and future of these systems, the ones with pristine Oort clouds will have had few injections of comets in the past with a large risk of comet injection in the future whereas the opposite is true for the ones with a depleted Oort cloud.

Additional uncertainties arise when considering that stars will also disrupt the Oort cloud. Recently, Hanse et al. (2018) looked at how stellar encounters strip the Oort cloud throughout the lifetime of the Sun. They simulate different orbital histories for the Sun and extract the resulting close encounter histories. With the encounter history they then simulate the single encounters and look at the exchange and loss of comets. They find that 25–65 per cent of the initial mass has been lost from just stellar encounters.

4.2.3 *Accretion*

As a star passes through a GMC, gas is accreted through Bondi–Hoyle–Lyttleton accretion. The accretion rate is given in the equation below (Hoyle & Lyttleton 1939; Bondi & Hoyle 1944).

$$\dot{M} = \frac{4\pi G^2 M_*^2 \rho}{v_{\rm rel}^3} \tag{15}$$

where M_* is the mass of the star that passes through a GMC which has density ρ with velocity $v_{\rm rel}$. This simple analytic approach has been studied in simulations by e.g. Springel, Di Matteo & Hernquist (2005) and Rafferty et al. (2006) and they show that the accretion rates drop below the analytic one once feedback is considered. However, the temperatures and time-scales for which this becomes relevant are much higher and longer than what we would expect to see for a GMC hit, therefore we can take the hit history of the Sun-like trajectories and apply equation (15) to them in order to determine the typical accretion rates experienced by the Sun when it passes through a GMC. The density of the GMCs is set to be the mean, i.e. the mass divided by the spherical volume. The distribution of densities is shown in Fig. 13. GMCs have a $R^{-1} - R^{-2}$(Cambresy 1999; Faesi, Lada & Forbrich 2016) density profile and the impact

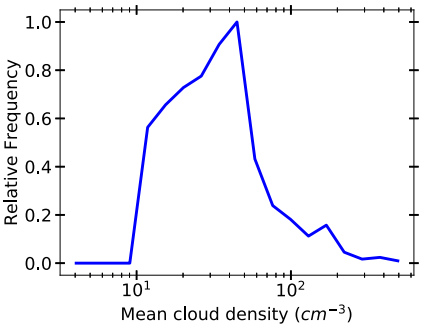

Figure 13. The mean densities of clouds hit by a star on a Sun-like orbit. These are the densities used to calculate the accretion rates in Fig. 14. The jagged corners in the distribution arise due to the mass–radius relationships defined in equations (7)–(9).

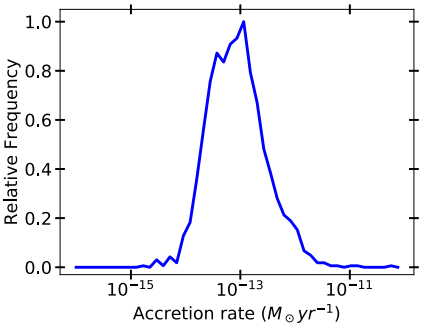

Figure 14. The accretion rates for stars passing through a GMCs on a Sun-like orbit.

parameters from the hit history follow an inverse distribution to that so using the mean gives a reasonable estimate of the average accretion rates. The resulting rates can be seen in Fig. 14.

From Fig. 14, we can conclude that during a regular GMC passage the particle densities required ($n > 1000\,{\rm cm}^{-3}$) to trigger so called 'Snowball Earth' as described by Pavlov et al. (2005), Yeghikyan & Fahr (2006), and Kataoka et al. (2013) will not be reached. This is because we know from studies of protoplanetary discs that they have depletion rates exceeding 10^{-10} $M_\odot$ yr^{-1}(Clarke, Gendrin & Sotomayor 2001). The Sun would likely evaporate the incoming gas at a 6–8 times lower rate than a planet-forming star due to the lower UV flux (Claire et al. 2012), however the evaporation would still be large enough to prevent any buildup of gas.

It should be pointed out that GMCs are not smooth structures (Draine 2011). They contain local overdensities known as clumps the densities of these objects can be between 10^2-10^4 times higher than the average GMC density. The accretion rates scales linearly with the surrounding gas density which means that a passage through such a clump would then cause a corresponding increase in accretion by a factor of 10^2-10^4. We can estimate how often a

star passes through a clump as it passes through a GMC by looking at the problem geometrically. Observations with APEX presented in Urquhart et al. (2018) show that a $\sim 10^6 M_\odot$ GMC will host $\sim$10 clumps, and the size scale of these clumps is $\sim$1 pc. The median size of GMCs hit in our simulation is 50 pc. Looking at surface area covered we get 0.4 per cent probability of going through a clump. We can easily show that the accretion rates in a clump would be sufficient, if we take a typical Bondi–Hoyle radius from our simulation, $\sim$7 au and say that we need to fill a sphere with that radius such that the mean density exceeds 1000 cm^{-3}. To do that it needs to accrete $10^{-11} M_\odot$ during a clump passage, which is easily done when the photoevaporation is overcome. However, the Sun experiences 1.6 ± 1.3 GMC crossings per Gyr. For that reason, it unlikely that any of the ice ages in the past 500 Myr were caused by passing through a clump.

4.3 Nearby and distant supernovae

We have looked at the occurrence rate of supernovae within 10 pc as it has been shown that this is the distance at which a mass extinction can be caused by a single supernovae (Beech 2011). Other work (Shaviv 2002; Shaviv et al. 2014) has pointed out that the integrated flux of cosmic rays from the more distant supernovae can also be damaging to the habitability of a planet. For this reason, we compare the two effects by looking at the total cosmic ray flux as a function of distance from a star. We do this by modifying the procedure first described in Section 4.1. We do the calculation using the median GMC mass encountered by the Sun ($5 \times 10^5 M_\odot$) with the median encounter velocity for the Sun (14 km s^{-1}). However, instead of drawing trajectories just through the GMC we let them pass through or near it, where the maximum distance they can pass from the surface of the GMC is also the maximum distance at which we count the supernovae. We determine the number of supernova occurring within 10 pc thick spherical shells. To get an estimate of the flux, we use the equation below.

$$F(R) = \Gamma(R) \sum_{i=0}^{N} d_i^{-2} \tag{16}$$

Here, d_i is the distance to a supernova and Γ is the relative frequency of the GMC encounters as a function of radius as determined in Section 4.2.1. The result is shown in Fig. 15. In it we see that over time the flux from the nearby supernovae will be the dominant source of cosmic rays hitting the star. The difference is not that large, it is a factor of $\sim$2 between the innermost and outermost radii. In the outer parts of the Galaxy, several Gyrs can pass without a supernova occurring within 10 pc so to fully understand the habitability of the Galaxy both the nearby and distant supernova need to be considered.

4.4 Non-axisymmetric potentials

We estimate the effect a spiral arm potential would have had by implementing a modified version of the potential presented in Pichardo et al. (2003). In their work, they construct the spiral arm potential by superpositioning oblate spheroids along the arm. We take their model and construct an analytical version of it in which the oblate spheroids are replaced by Plummer spheres (equation 2). We put in 50 Plummer spheres per arm, and set the total mass of the arms consisting of 200 Plummer spheres arms to be 1.75 per cent of the disc mass shown in Table 1. We set the softening length ($b_{\rm b,\,h}$ in equation 2) to be 500 pc, the same as the semiminor axis of

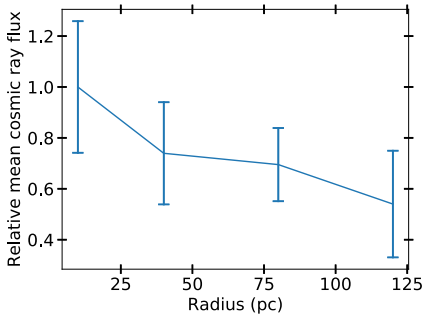

Figure 15. The total cosmic ray flux from supernovae at different distances from a star orbiting through the Galaxy, calculated using equation (16).

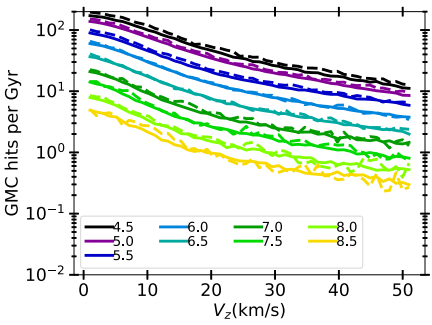

Figure 16. The number of GMC hits per Gyr for runs with a spiral arm potential (dashed) and without (solid) as a function initial V_z. The stars were initialized at different radii using spiral arm model A and then binned and plotted in 500 pc wide bins centred at the values shown in the figure. Velocity dispersion is $\sigma_R = 30$ km s^{-1} and $\sigma_\theta = 20$ km s^{-1}. It should be noted that for computational efficiency the number of trajectories in the runs with the spiral potential are reduced by a factor of 10 This lead to large amounts of noise at large V_z for $R > 6$ kpc and bins with $R > 8.5$ kpc have been excluded as they were too noisy.

the oblate spheroids in Pichardo et al. (2003) and with the mass of the Plummer spheres following the same radial distribution as the gas. We find that the effect on the number of GMC hits is small, as the gravitational focusing by the arms is limited. Fig. 16 shows an increase in the number of GMC hits by 5–10 per cent at a given radius which is small compared to the spread in the number of hits seen in Fig. 4. The only significant difference that we do see is that there are fewer trajectories in the bins at large radii. The spiral arms scatter the trajectories such that their guiding radii on average become slightly smaller. This effect is *not* churning, or as it is also known, radial migration. For that corotation with the spiral arms is needed, along with transient spiral arms (Sellwood & Binney 2002) which is not the case here since with our potential and chosen pattern speed (20 km s^{-1} kpc^{-1}) corotation occurs at 11.6 kpc. The inclusion of the spiral arms also leads to a marginally

higher velocity dispersion which slightly reduces the supernova risk during a GMC hit as seen in Fig. 5, this effect is however also quite small. All in all the inclusion of the spiral arm potential would have a very small effect on the result.

Looking specifically at radial migration, studies (Schönrich & Binney 2009; Frankel et al. 2018) have suggest that the Sun formed at 5 kpc and then migrated outward. From the previously determined radial scale length of the number of hits per Gyr of 750–850 pc, we find that this change corresponds to 3.5–4 scale lengths depending on the V_z. This means that such a migration would result in a factor of 35–55 change in the hit rate depending on the V_z. As was discussed with respect to Fig. 4, at 5 kpc all trajectories of young stars (low V_z) have several tens of to hundreds hits per Gyr. This means that prior to its migration the Sun was constantly hitting GMCs and being affected by supernovae, whereas at 8 kpc its not uncommon for a Gyr to pass without a single GMC being hit. This does not take into account that the SFR was higher by a factor of 3 (van Dokkum et al. 2013) in the Sun's infancy (4.5 Gyr ago). The Sun's birth at 5 kpc and subsequent migration could in part explain the late emergence of land-based life on the Earth.

As for the potential itself, as stated previously we tested a set of potentials (Paczynski 1990; McMillan 2017) and only found differences in the hit rate on the order of 10 per cent when reproducing the simulations in different potentials. The total number of hits remained largely unchanged however we do see some local differences, i.e. there is a variation in the number of hits at a given V_z for different radii. This can be explained by the fact that the motion of the GMCs and stars change in the same way when the potential is changed. What is invariant between the potential changes is the distribution of the GMCs, e.g. in one potential at a given R and V_z a star might get out of the GMC layer, whereas in a different one it just barely cannot. This will of course lead to some differences.

4.5 Galactic Habitable Zone

The GHZ is an annular region in the Galaxy in which one is most likely to find a habitable planet (Gonzalez et al. 2001). The outer edge of the annulus is generally determined by the average metallicity of stars, once this drops too low ([Fe/H] $\lesssim -0.7$) making an Earth analogue which can sustain complex life becomes impossible (Lineweaver et al. 2004). The inner edge of the annulus can also be set by looking at the metallicity. A high metallicity results in a higher occurrence rate of gas giants (Fischer & Valenti 2005), this can inhibit the chances of forming terrestrial planets in the habitable zone (Levison & Agnor 2003) and if planets do end up in the habitable zone their orbits can easily be destabilized (Carrera et al. 2016; Agnew et al. 2017; Agnew, Maddison & Horner 2018). Additionally, authors argue (Gonzalez et al. 2001; Vukotić et al. 2016) that the high metallicity will make terrestrial planets with such high surface densities as to be inhospitable for organic life. Another way of setting the bound is by looking at the hazards posed by the Galaxy, primarily nearby supernovae (Gowanlock et al. 2011; Spitoni et al. 2014; Morrison & Gowanlock 2015).

Using our results we can determine our own habitable zone in which the z-dimension (which is often excluded) is included in the analysis and supernovae are correctly distributed in the Galaxy. The Sun is obviously habitable, so we take our findings for Sun-like orbits and determine a habitability criterion based on that. The Sun experiences 1.6 ± 1.3 GMC hits per Gyr so as the habitability criteria we say that a star must experience two or fewer GMC hits per Gyr. Then, we determine the distribution of the number of habitable

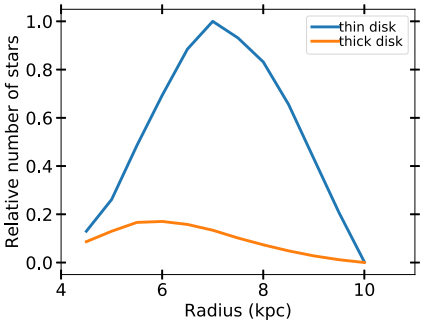

Figure 17. The relative number of habitable stars in the Galaxy as a function of radius. This is calculated using the condition for habitability that a star hits fewer than two GMCs per Gyr, which is based on the Solar value. Then, using the structure of the discs found in Bland-Hawthorn & Gerhard (2016, equation 4.5) we determine the distributions.

stars as a function of Galactic radius using the equation below:

$$N = \sum_{V_z} A \times f_2(V_z, R) \times f_h(V_z) \times f_{[Fe/H]}(R) \times \Sigma(R) R dr \quad (17)$$

where A is a normalization constant, f_2 the fraction of runs at a given V_z, and R that have fewer than two hits per Gyr. f_h is the fraction of stars in a V_z bin given a scale height of the stars. $\Sigma(R)Rdr$ is the number of stars in a radial bin, scale height, and length given by Bland-Hawthorn & Gerhard (2016). $f_{[Fe/H]}$ is the fraction of stars at [Fe/H] > -0.7, given by Hayden et al. (2015). The resulting distributions can be found in Fig. 17. For the thin disc, we find the habitable zone to be at 5.8–8.8 kpc with a peak at 7 kpc, and for the thick disc 4.5–7.7 with a peak at 5.7 kpc, with a peak at 17 per cent relative to the thin disc. The thick disc is the kinematic thick disc with a radial scale length of 2 kpc and a scale height of 1 kpc. The width of what we call the habitable zone is where the occurrence rate drops to 50 per cent of the peak value.

Further, one could consider where one is most likely to find a star having a planet hosting complex life on it. For this one would also have to consider the age of the systems as it takes time for life to evolve which means that the longer time a system has been within the GHZ the higher the probability of complex life having formed. From Martig et al. (2016), we know there is a strong negative radial age gradient, i.e. there are more older stars at small radii. This means that both the distributions in Fig. 17 would shift inwards and additionally the thick disc can even host more habitable planets depending on ones criteria as it has a significantly older population.

5 SUMMARY

We have investigated how often stars on different trajectories pass through GMCs (hits) and during a passage how often a star passes within 10 pc of a supernova as it explodes and is affected by it. Through this we have been able to address a number of issues both with regards to the Sun and its history but also with regard to the Galaxy and other stars as a whole. The main results are:

(i) We find that the number of GMC hits decrease exponentially with increasing radius (R) and velocity perpendicular to the Galactic plane (V_z). The resulting hit rates can be seen in Fig. 4. We find the

scale length for the number of hits to lie between 750 and 850 pc dependent on the V_z and the scale velocity is $\sim$12 km s^{-1} (Table 8). These effects can cancel out, meaning that a star at 7 kpc with a V_z of 5 km s^{-1} will experience the same number of hits as a star at 5 kpc with a V_z of $\sim$30 km s^{-1}.

(ii) We find a narrow distribution in the number of GMC hits at smaller radii for low V_z orbits. This implies that at 4–5 kpc nearly all stars will experience several tens of GMC hits per Gyr, whereas a significant fraction of stars at 8 kpc experience no GMC hits at all during 1 Gyr, even though the mean is roughly 2.

(iii) As a star ages and V_z is excited the frequency of GMC hits will go down and the frequency of supernovae a star is affected by will go down even more rapidly (Fig. 7) because when the star does hit a GMC it will pass through it with a higher velocity and thus decrease the chance of being affected by a supernova because the risk is dependent on the velocity with which the GMC is hit.

(iv) We find that a Sun-like orbit hits 1.6 ± 1.3 GMCs per Gyr (once every 625^{+2700}_{-280} Myr) and we find that it is within 10 pc of and affected by a supernova 1.5 ± 1.1 times per Gyr (once every 667^{+2500}_{-240} Myr) or 0.8 ± 0.6 times per Gyr if one corrects for the spatial and temporal clustering, i.e. if a star passes through a GMC as supernovae are going off it is likely to be hit by more than one (once every $1.25^{+3.75}_{-0.55}$ Gyr).

(v) The nearby supernova occurrence rate that we calculate differs somewhat from literature values. This is due to the fact that previous authors have used the local stellar density to determine the nearby supernova occurrence rate, we argue that it is the H_2 density as a proxy for SFR that matters and in Fig. 8 we see the resulting differences in using a stellar and gas density for the occurrence rates.

(vi) If the Sun was located at 5 kpc it would have a much higher GMC hit frequency and therefore also similarly be affected much more by supernovae. It has been suggested that the Sun did form at 5 kpc (Schönrich & Binney 2009; Frankel et al. 2018), if this is the case it will constantly have been perturbed by the Galaxy at earlier times. A migration later in the lifetime of the Sun could explain the late emergence of land-based life on Earth.

(vii) We find that our model is consistent with deposits from recent distant supernova history traced by radioactive elements found on ocean floor. We show that the observed local arm substructure explains the supernova record well and we favour a model in which both the recorded supernovae originated from the same star-forming cloud. To model the history of the Sun specifically one needs to include the potential of the spiral arms.

(viii) The amount of gas needed to be accreted by the Sun to trigger a 'Snowball Earth' is easily reached based on our calculations. However, the main obstacle is overcoming the evaporation of incoming gas by the Sun. To do so a much larger accretion rate is required, which can be achieved in very few cases (0.4 per cent) when a clump will be hit resulting in accretion rates up to 10^2-10^4 times the normal.

(ix) Applying our data and results to Napier & Staniucha (1982) and Hut (1984), we find that the Oort Cloud has been depleted to only contain $10^{-2}-10^{-3}$ of its original comets. However, we find that the depletion is very sensitive to the number of and the relative velocity of the encounters; implying that some Sun-like stars can have nearly pristine Oort Clouds and others very depleted.

(x) We determine the habitable zone for Galaxy for the two kinematically different discs. We do this by using the hit history for the Sun-like orbits (Fig. 9) to find limits for habitability, along with average metallicity of the Galaxy and stellar number count. For the thin disc, we find it to lie between 5.8–8.8 kpc and for the thick disc between 4.5–7.7 kpc peaking at 7 and 5.7 kpc, respectively, as can be seen in Fig. 17.

ACKNOWLEDGEMENTS

The authors are supported by the project grant 2014.0017 'IMPACT' from the Knut and Alice Wallenberg Foundation. The simulations were performed on resources provided by the Swedish National Infrastructure for Computing (SNIC) at Lunarc, which we can contribute thanks to grants from The Royal Physiographic Society of Lund. We would also like to thank the referee who gave us valuable input that helped improve the paper.

REFERENCES

Agnew M. T., Maddison S. T., Thilliez E., Horner J., 2017, MNRAS, 471, 4494
Agnew M. T., Maddison S. T., Horner J., 2018, MNRAS, 477, 3646
Bahcall J. N., Hut P., Tremaine S., 1985, ApJ, 290, 15
Bailer-Jones C., 2009, Int. J. Astrobiol., 8, 213
Beech M., 2011, Ap&SS, 336, 287
Bissantz N., Englmaier P., Gerhard O., 2003, MNRAS, 340, 949
Bland-Hawthorn J., Gerhard O., 2016, ARA&A, 54, 529
Bondi H., Hoyle F., 1944, MNRAS, 104, 273
Cambresy L., 1999, A&A, 345, 8
Carrera D., Davies M. B., Johansen A., 2016, MNRAS, 463, 3226
Claire M. W., Sheets J., Cohen M., Ribas I., Meadows V. S., Catling D. C., 2012, ApJ, 757, 95
Clarke C. J., Gendrin A., Sotomayor M., 2001, MNRAS, 328, 485
Clemens D., Sanders D., Scoville N., 1988, ApJ, 327, 139
Dehnen W., Binney J. J., 1998, MNRAS, 298, 387
Dias W. S., Lépine J. R. D., 2005, ApJ, 629, 825
Draine B. T., 2011, Physics of the Interstellar and Intergalactic Medium. Princeton Univ. Press, Princeton, NJ
Ellis J., 1995, Proc. Natl. Acad. Sci., 92, 235
Faesi C., Lada C., Forbrich J., 2016, ApJ, 821, 18
Feng F., Bailer-Jones C. A. L., 2013, ApJ, 768, 152
Fischer D. A., Valenti J., 2005, ApJ, 622, 1102
Frankel N., Rix H.-W., Ting Y.-S., Ness M., Hogg D. W., 2018, ApJ, 865, 96
Gammie C. F., Ostriker J. P., Jog C. J., 1991, ApJ, 378, 565
Gao Y., Lo K. Y., Lee S.-W., Lee T.-H., 2001, ApJ, 548, 172
García-Sánchez J., Weissman P. R., Preston R. A., Jones D. L., Lestrade J.-F., Latham D. W., Stefanik R. P., Paredes J. M., 2001, A&A, 379, 534
Goldbaum N. J., Krumholz M. R., Matzner C. D., Mckee C. F., 2011, ApJ, 738, 101
Gonzalez G., Brownlee D., Ward P., 2001, Icarus, 152, 185
Goodwin S. P., Whitworth A. P., 2004, A&A, 413, 929
Gowanlock M. G., Patton D. R., Mcconnell S. M., 2011, Astrobiology, 11, 855
Green D. A., 2015, MNRAS, 454, 1517
Güdel M., 2007, Living Rev. Solar Phys., 4, 3
Gustafsson B., Church R., Davies M. B., Rickman H., 2016, A&A, 593, 19
Hanse J., Jílková L., Portegies Zwart S. F., Pelupessy F. I., 2018, MNRAS, 473, 5432
Hayden M. R. et al., 2015, ApJ, 808, 132
Hou L., Han J., Shi W., 2009, A&A, 499, 473
Hou L. G., Han J. L., 2014, A&A, 125, 1
Hoyle F., Lyttleton R. A., 1939, Proc. Camb. Phil. Soc., 35, 405
Hut P., 1984, Nature, 311, 638
Hut P., Tremaine S., 1985, AJ, 90, 1548
Hyde M., Pecaut M. J., 2018, Astron. Nachr., 339, 78
Immler S. et al., 2006, ApJ, 648, L119
Junqueira T. C., Chiappini C., Lépine J. R. D., Minchev I., Santiago B. X., 2015, MNRAS, 449, 2336

Kataoka R., Ebisuzaki T., Miyahara H., Maruyama S., 2013, New Astron., 21, 50
Knie K., Korschinek G., Faestermann T., Dorfi E. A., Rugel G., Wallner A., 2004, Phys. Rev. Lett., 93, 1
Kroupa P., 2001, MNRAS, 322, 231
Krumholz M. R., Matzner C. D., McKee C. F., 2006, ApJ, 653, 361
Levison H. F., Agnor C., 2003, AJ, 125, 2692
Li W., Chornock R., Leaman J., Filippenko A. V., Poznanski D., Wang X., Ganeshalingam M., Mannucci F., 2011, MNRAS, 412, 1473
Li Z., Gerhard O., Shen J., Portail M., Wegg C., 2016, ApJ, 824, 11
Licquia T. C., Newman J. A., 2015, ApJ, 806, 96
Lineweaver H. C., Fenner Y., Gibson K. B., 2004, Science, 303, 59
Ludwig P. et al., 2016, Proc. Natl. Acad. Sci., 113, 9232
Martig M., Minchev I., Flynn C., 2014, MNRAS, 442, 2474
Martig M., Minchev I., Ness M., Fouesneau M., Rix H.-W., 2016, ApJ, 831, 139
Martos M., Hernandez X., Yá nez M., Moreno E., Pichardo B., 2004, MNRAS, 350, 2000
McMillan P. J., 2017, MNRAS, 465, 76
Miville-Deschênes M.-A., Murray N., Lee E. J., 2017, ApJ, 834, 1
Miyamoto M., Nagai R., 1975, PASJ, 27, 533
Modjaz M. et al., 2009, ApJ, 702, 226
Morrison I. S., Gowanlock M. G., 2015, Astrobiology, 15, 683
Nakanishi H., Sofue Y., 2006, PASJ, 58, 13
Napier W. M., Staniucha M., 1982, MNRAS, 198, 723
Nimura T., Ebisuzaki T., Maruyama S., 2016, Gondwana Res., 37, 301
Nordström B., Mayor M., Andersen J., Holmberg J., Pont F., Olsen E. H., Udry S., Mowlavi N., 2004, A&A, 1019, 989
Ochsendorf B. B., Meixner M., Roman-duval J., Rahman M., Evans N. J., 2017, ApJ, 841, 109
Oort J., 1950, Bull. Astron. Inst. Netherlands, 11, 91
Paczynski B., 1990, ApJ, 348, 485
Parker R. J., Church R. P., Davies M. B., Meyer M. R., 2014, MNRAS, 437, 946
Pavlov A. A., Toon O. B., Pavlov A. K., Bally J., Pollard D., 2005, Geophys. Res. Lett., 32, L03705
Pichardo B., Martos M., Moreno E., Espresate J., 2003, ApJ, 582, 230
Plummer H. C., 1911, MNRAS, 71, 460
Rafferty D. A., McNamara B. R., Nulsen P. E. J., Wise M. W., 2006, ApJ, 652, 216
Raup M. D., Sepkoski J. J., 1984, Proc. Natl. Acad. Sci., 81, 801
Roman-Duval J., Jackson J. M., Heyer M., Rathborne J., Simon R., 2010, ApJ, 723, 492
Roman-Duval J., Heyer M., Brunt C. M., Clark P., Klessen R., Shetty R., 2016, ApJ, 818, 144
Rosolowsky E., Leroy A., 2006, PASP, 118, 590
Rubincam D. P., 2016, Icarus, 264, 132
Ruderman M. A., 1974, Science, 184, 1079
Schönrich R., Binney J., 2009, MNRAS, 396, 203
Scoville N. Z., Yun M. S., Sanders D. B., Clemens D. P., Waller W. H., 1987, ApJS, 63, 821
Sellwood J. A., Binney J. J., 2002, MNRAS, 336, 785
Sellwood J. A., Carlberg R. G., 2014, ApJ, 785, 137
Shaviv N. J., 2002, Phys. Rev. Lett., 89, 051102
Shaviv N. J., 2003, New A, 8, 39
Shaviv N. J., Prokoph A., Veizer J., 2014, SciRep, 4, Article ID 6150
Spitoni E., Matteucci F., Sozzetti A., 2014, MNRAS, 440, 2588
Springel V., Di Matteo T., Hernquist L., 2005, MNRAS, 361, 776
Sørensen M., Svensmark H., Jørgensen U. G., 2017, MNRAS, 14, 1
Tanaka H. K. M., 2006, Atmosph. Sol.Terrestr. Phys, 68, 1396
Thomas B. C. et al., 2005, ApJ, 634, 509
Tremaine S., 1993, in Phillips J. A., Thorsett S. E., Kulkarni S. R., eds, ASP Conf. Ser. Vol. 36, Planets Around Pulsars, Astron. Soc. Pac., San Francisco, p. 335
Urquhart J. S. et al., 2018, MNRAS, 473, 1059
Vallée J. P., 2017, Ap&SS, 362, 79
Vallini L., Ferrara A., Pallottini A., Gallerani S., Pichat B., Bologna I., 2016, MNRAS, 4, 1
van Dokkum P. G. et al., 2013, ApJ, 771, L35
Vukotić B., Steinhauser D., Martinez-Aviles G., Ćirković M. M., Micic M., Schindler S., 2016, MNRAS, 459, 3512
Wallner A. et al., 2016, Nature, 532, 69
Wienen M. et al., 2015, A&A, 579, A91
Williams J. P., McKee C. F., 1997, ApJ, 476, 166
Yeghikyan A., Fahr H., 2006, in Frisch P. C., ed., Astrophysics and Space Science Library Vol. 338, Solar Journey: The Significance of our Galactic Environment for the Heliosphere and Earth. Springer-Verlag, Berlin, p. 317
Yu J., Liu C., 2018, MNRAS, 475, 1093
Zapartas E. et al., 2017, A&A, 601, A29

This paper has been typeset from a TEX/LATEX file prepared by the author.

Paper II

Paper II:Resilient habitability of nearby exoplanet systems

G. Kokaia, M.B. Davies, A.J. Mustill (2020)
Monthly Notices of the Royal Astronomical Society, Volume 492, Issue 1, p. 352-368

My contribution:

The work in this paper was largely built upon the work done by one of MBD's previous PhD-students (Carrera 2016). After reading a series of papers written by a former student at the department (Agnew et al. 2017, 2018) GK thought that they could apply the methodology developed in Carrera (2016) to further the analysis in those papers. This meant that the numerical setup was already well understood by MBD and replicating the methods Carrera (2016) became quite easy. The work of GK consisted of looking through exoplanet databases and papers to find systems to simulate, performing the simulations, writing the code for and doing the analysis of the output. GK's co-supervisor, Alexander Mustill (AM), provided help with the analysis towards the end of the paper that deals with resonances and secular theory. He also performed the simulations for the scattering experiment described in the beginning of the paper and wrote two sub-sections. The paper writing process was very similar to that of the first paper, with AM providing feedback for revisions in the same manner. The key difference being that both MBD and AM did a round with direct edits, with AM writing a couple of paragraphs, before submission.

Monthly Notices
of the
ROYAL ASTRONOMICAL SOCIETY

MNRAS **492,** 352–368 (2020)
Advance Access publication 2019 December 9

doi:10.1093/mnras/stz3408

Resilient habitability of nearby exoplanet systems

Giorgi Kokaia,★ Melvyn B. Davies and Alexander J. Mustill

Lund Observatory, Department of Astronomy and Theoretical Physics, Lund University, Box 43, SE-221 00 Lund, Sweden

Accepted 2019 November 30. Received 2019 November 29; in original form 2019 October 16

ABSTRACT

We investigate the possibility of finding Earth-like planets in the habitable zone of 34 nearby FGK-dwarfs, each known to host one giant planet exterior to their habitable zone detected by RV. First we simulate the dynamics of the planetary systems in their present day configurations and determine the fraction of stable planetary orbits within their habitable zones. Then, we postulate that the eccentricity of the giant planet is a result of an instability in their past during which one or more other planets were ejected from the system. We simulate these scenarios and investigate whether planets orbiting in the habitable zone survive the instability. Explicitly we determine the fraction of test particles, originally found in the habitable zone, which remain in the habitable zone today. We label this fraction the *resilient habitability* of a system. We find that for most systems the probability of planets existing [or surviving] on stable orbits in the habitable zone becomes significantly smaller when we include a phase of instability in their history. We present a list of candidate systems with high resilient habitability for future observations. These are: HD 95872, HD 154345, HD 102843, HD 25015, GJ 328, HD 6718, and HD 150706. The known planets in the last two systems have large observational uncertainties on their eccentricities, which propagate into large uncertainties on their resilient habitability. Further observational constraints of these two eccentricities will allow us to better constrain the survivability of Earth-like planets in these systems.

Key words: planets and satellites: dynamical evolution and stability – planets and satellites: general – planetary systems.

1 INTRODUCTION

One of the key goals for exoplanet science is to observe an Earth-like planet located in the habitable zone (HZ) of a Sun-like star, where the HZ is defined as the spherical shell at a distance that permits liquid water to exist on the planet's surface.

Detecting Earth-mass (i.e. low-mass) planets has been technologically limited, however new instruments such as ESPRESSO (currently operational with the sensitivity slowly increasing (Pepe et al. 2010; Leite et al. 2018), space missions like PLATO (Rauer et al. 2014), and future large telescopes such as E-ELT and TMT (Gilmozzi & Spyromilio 2007; Skidmore et al. 2015) offer the prospect for the discovery of Earth-like planets in the near future.

Discovering Earth-like planets will, however, be difficult even with the next generation of instruments. One must focus attention on a relatively small number of stars (or planetary systems). A natural question is then: *which systems do we select for further detailed study?* In this paper we will consider local stars possessing one observed (massive) planet located beyond the HZ. Through numerical modelling of their dynamical past, we select the subset having the best prospects for possessing a habitable low-mass planet. Considering systems containing a Jupiter-mass planet further out makes sense for a number of reasons:

(i) Recent work has shown that the presence of Jupiter was instrumental in shaping the inner parts of the Solar System by clearing out or preventing the delivery of a large fraction of the solids in the early inner disc. This might be a requirement for systems such as the Solar System to form (Batygin & Laughlin 2015; Childs et al. 2019; Lambrechts et al. 2019), rather than the systems commonly found by *Kepler* which consist of super-Earths and mini-Neptunes on tightly packed orbits within 0.5 au (Mullally et al. 2015).

(ii) Until relatively recently there was commonly held belief that Jupiter protected the Earth from impacts (see e.g. Ward, Brownlee & Krauss 2000). This belief has come under scrutiny as the effect of Jupiter on impact rates has been looked at more closely through numerical simulations (Laakso, Rantala & Kaasalainen 2006). Jupiter actually appears to cause a slight enhancement in impacts from bodies originating in the asteroid and Kuiper belt (Horner & Jones 2008, 2009) whilst reducing the impact rate of long-period comets (Horner, Jones & Chambers 2010). Regardless, giant planets appear to have been instrumental in delivering water and other volatiles to the inner parts of the system, whether it happened

★ E-mail: giorgi@astro.lu.se

after formation (Chyba 1990; Morbidelli et al. 2000; Abramov & Mojzsis 2009; Carter-Bond, O'Brien & Raymond 2014; Grazier 2016) or during formation (Raymond, Mandell & Sigurdsson 2006; Raymond & Izidoro 2017; O'Brien et al. 2018).

(iii) Systems with gas giants are very likely to also host low-mass planets. Recent studies have shown that ∼40 per cent of systems that have low-mass planets (in this case 'low-mass' implies $\lesssim 10\,M_\oplus$) also host an external gas giant (Zhu & Wu 2018; Bryan et al. 2019). Further, Zhu & Wu (2018) invert this occurrence rate using overall occurrence rates for each type of planet and conclude that ∼90 per cent of gas giant systems should have interior, lower mass planets. The correlations found are not strictly for the Earth-like planets that we consider in this work. However, one could argue that if there were data to consider these planets then the correlation might be even stronger, given the fact that a gas giant might be required to even be able to have Earth-like planets. For comparison, Burke et al. (2015) determined the occurrence rate for Earth-like planets around GK-dwarfs given by extrapolation from *Kepler* systems to be $\sim 6 \pm 3$ per cent for planets with radii between 0.75 and 1.75 Earth radii and 300–700 d orbits. By instead considering *Kepler* non-detections, Hsu et al. (2019) determined an upper bound (84th percentile) of 27 per cent on the occurrence rate of planets with radii between 0.75 and 1.5 Earth radii on periods of 237–500 d. They caution however that the bound is likely overestimated by up to a factor of two due to contamination by false alarms.

(iv) The RV-signal strength from a planet is proportional to $M_\mathrm{p} \sin I_\mathrm{p}$ where I_p is the inclination of the orbital plane with respect to the plane of the sky, with the observer at $I_\mathrm{p} = 90^\circ$. For nearby giant planets, *Gaia* will be able to constrain the orbital plane (Sozzetti et al. 2008; Perryman et al. 2014; Ranalli, Hobbs & Lindegren 2018). Given that planetary systems seem to typically have low mutual inclinations (Lissauer et al. 2011; Johansen et al. 2012), we can further constrain which systems to observe by picking out those in which the giant planet has $I_\mathrm{p} \approx 90^\circ$. This gives a strong prior for the amplitude of the RV signal from the Earth-like planet being observed to be close to its maximum possible value.

However, a gas giant may destabilize certain orbits including those within the HZ of a planetary system (Jones, Sleep & Chambers 2001; Menou & Tabachnik 2003; Veras & Armitage 2005; Matsumura, Ida & Nagasawa 2013; Agnew et al. 2017; Agnew, Maddison & Horner 2018; Georgakarakos, Eggl & Dobbs-Dixon 2018). In this paper we will not only re-examine the present day habitability of systems containing giant planets, but also determine the fraction of test particles remaining within HZs when one accounts for the past dynamical evolution of particular systems. We term this fraction the *resilient habitability* (Carrera, Davies & Johansen 2016) of these systems.

The resilient habitability of a system is determined by assuming that the system initially consisted of multiple planets and that the eccentricity of the observed planet is the result of one or more other planets' being ejected when the system became unstable. The idea is that changes to the orbits and ejection of planets during the instability will do considerably more damage to Earth-like planets in the HZ than the system as seen today with its post-instability architecture. In summary, from our simulations we determine two types of habitability for each of the observed systems we study:

Present-day habitability: The fraction of test particles that remain in the HZ when the system is simulated in its present day configuration. We denote this as $f_{\mathrm{hab,\,1P}}$.

Resilient habitability: The fraction of test particles that remain in the HZ when the past dynamical evolution of the system is simulated. We denote this as f_{rhab}.

This paper is arranged as follows. In Section 2 we discuss how scattering between two planets can lead to the ejection of one with the other becoming more bound and eccentric. We show how the eccentricity reached is a function of the mass ratio of the two planets. In Section 3 we present the known planet-hosting systems we have selected to investigate, each of which has a single giant planet exterior to the HZ. Section 4 describes our calculations of both the present day and resilient habitability of these systems. The results of these calculations are presented in Section 5. The implications of our results are discussed in Section 6. In Section 7 we list the systems which in our view represent the best candidates for further searches for Earth-like planets. We summarize the paper in Section 8.

2 GIANT PLANET SCATTERING

We know from observations (Buchhave et al. 2018), and suspect from simulations (Thommes, Matsumura & Rasio 2008; Mordasini, Alibert & Benz 2009), that giant planets rarely form alone. Furthermore, it has been shown that giant planets form on circular or nearly circular orbits (Bitsch et al. 2013; Ragusa et al. 2018) which are later made more eccentric, whereas the observed exoplanet eccentricity distribution is consistent with most of them having been made eccentric through planet–planet scattering (Ford & Rasio 2008; Jurić & Tremaine 2008).

In this section we consider scattering between massive planets within two-planet systems. When two planets are placed on sufficiently close, low-eccentricity orbits, they will become unstable, leading to the two orbits crossing which then leads to a series of strong planet–planet scattering events, with one planet being ejected whilst one remains on a more bound, and eccentric, orbit. For a review on the dynamical evolution of planetary systems see Davies et al. (2014).

Here, we model two systems orbiting around a Solar-mass star: one containing two Jupiter-mass planets and one containing one Jupiter-mass planet and one Saturn-mass planet, in order to investigate how the eccentricity distribution of the planets left behind (once one planet is ejected) depends on the mass ratio of the two planets. We place one Jupiter at 5.2 au and place a second either Jupiter- or Saturn-mass planet in the range [5.2,7.6] au. This setup eventually leads to planet–planet scattering during which either of the Jupiter-mass planets can be ejected in the first case and the Saturn-mass planet is ejected in the second case. Fig. 1 shows the semimajor axis and eccentricity of the remaining planet for the two systems. The distribution of eccentricities is clearly a function of the mass ratio of the two planets. In ejecting a second Jupiter, the remaining Jupiter-mass planet has to give up more energy and angular momentum, thus making it more bound and more eccentric than when the inner Jupiter ejects a Saturn-mass planet.

We will make use of the mass ratio dependence of eccentricity when we consider the dynamical histories of our selected observed systems. For example, if the observed planet in a system has a eccentricity below about 0.3, we can then expect the planet to have ejected (only) Saturn-mass planets in the past, whereas for larger eccentricities, the planet is more likely to have ejected one (or more) planets of equal mass.

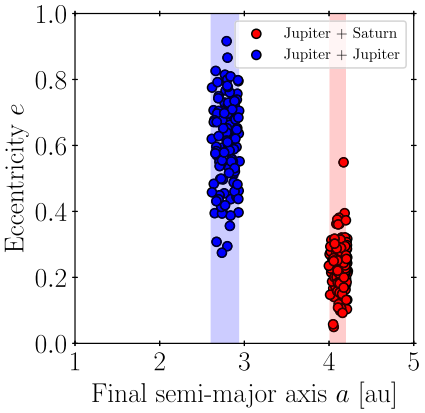

Figure 1. The figure shows the a and e of a surviving Jupiter-mass planet after having ejected a second planet in an unstable two-planet system. The shaded region shows the range of semimajor axes permitted based on a simple energy consideration. The two colours show two different mass combinations: Jupiter plus Jupiter, and Jupiter plus Saturn.

Table 1. Parameters used in equation (2) for determining the boundaries of the habitable zone as given by Kopparapu et al. (2014).

Parameter	Inner edge Runaway greenhouse	Outer edge Maximum greenhouse
$S_{\rm eff\odot}$	1.107	0.356
a	1.332×10^{-4}	6.171×10^{-5}
b	1.58×10^{-8}	1.698×10^{-9}
c	-8.308×10^{-12}	-3.198×10^{-12}
d	-1.931×10^{-15}	-5.575×10^{-16}

3 SYSTEM SELECTION

We select systems from the exoplanet archive[1] with a single gas giant ($0.3\,{\rm M_J} < M_{\rm p}\sin I_{\rm p} < 8\,{\rm M_J}$, where $\rm M_J$ is the mass of Jupiter) orbiting an FGK-dwarf star ($1.4\,{\rm M_\odot} \gtrsim {\rm M_\star} \gtrsim 0.65\,{\rm M_\odot}$, ${\rm R_\star} < 2R_\odot$) beyond its HZ.

The HZ is defined as a shell at a distance from a star with a given luminosity (L) and effective temperature ($T_{\rm eff}$) in which a planet can have liquid water on its surface. The boundaries of the HZ for each system are determined using the formula derived by Kopparapu et al. (2014), shown below:

$$d = \left(\frac{\rm L/L_\odot}{S_{\rm eff}}\right)^{0.5} {\rm AU}, \quad (1)$$

where $\rm L_\odot$ is the Solar luminosity and

$$S_{\rm eff} = S_{\rm eff\odot} + aT_\star + bT_\star^2 + cT_\star^3 + dT_\star^4 \quad (2)$$

is a measure of the flux received by the planet and $T_\star = T_{\rm eff} - T_\odot$ ($T_\odot = 5780$ K). The values for the parameters are given in Table 1. The inner edge of the HZ is set using the model parameters for runaway greenhouse habitability, the limit at which the temperature of the planet, under any realistic atmospheric conditions, inevitably becomes too high. The outer edge is set using the maximum greenhouse parameters, which is the limit at which an optimally constructed atmosphere to maximize the greenhouse effect can no longer prevent all the water from freezing.

To further limit the number of systems we simulate, we impose another criterion; the pericentre calculated using an eccentricity one standard deviation lower than the mean observed value must lie exterior to the HZ.

The criteria leave us with 34 systems as listed in Table 2. We include in this table the stellar parameters used to determine the HZ. They are plotted and highlighted in Fig. 2 along with every other known single planet RV system that matches our criterion for planetary mass and stellar type. Half of these systems can be found on the short-list of Agnew et al. (2017, 2018) who investigated the present day stability of orbits in the HZ. For the remaining half, some planets were considered by Agnew et al. (2017, 2018) to be so distant that the orbits of test particles in the HZ would be unaffected by the planet, and therefore were not investigated. We also include some high eccentricity systems with limited stability that did not make their cut and some systems discovered subsequent to their work.

4 SETUP OF THE NUMERICAL EXPERIMENTS

We perform all our N-body simulations using the Bulirsch–Stoer integrator of the MERCURY package (Chambers 1999), with an accuracy parameter of 10^{-12} resulting in a relative energy error of less than 10^{-5} for all runs.

4.1 Present-day habitability

As a first step we simulate all the planetary systems in their present day configuration to determine the present-day habitability, i.e. the fraction of test particle orbits which keep their semimajor axis in the HZ despite the presence of a nearby giant planet. We refer to this value as $f_{\rm hab,\,1P}$.

We place 100 test particles in the HZ with their semimajor axes distributed uniformly from inner to outer edge. We place them on circular orbits and make them coplanar with the planet. We randomly pick the three Keplerian angles (argument of perihelion, ω; longitude of ascending node, Ω, and mean anomaly, M) between 0° and 360° and then integrate the systems for 10^7 yr. For each system we check if 10 Myr was sufficient for it to relax, i.e. if after 10 Myr particles are still being lost. If any test particle was lost within the last Myr we run the system for another Myr and check again repeating the process until no more test particles are lost. We find that for most systems 10 Myr is sufficient. For each system we do three simulations. One simulation using the reported eccentricity of the giant planets and two using the $\pm 1\sigma$ eccentricity values shown in Table 2.

The systems we simulate are shown in Fig. 3. They are split into three groups:

Group 1: Systems where the planet has a considerably larger semimajor axis than the outer edge of the HZ and a low eccentricity, or has a moderate eccentricity with a much larger semimajor axis.

Group 2: Systems where the planet has a semimajor axis just outside the outer edge of the HZ with a low to moderate eccentricity or at larger semimajor axis with a sufficiently high eccentricity to bring the pericentre very close to the HZ.

[1] https://exoplanetarchive.ipac.caltech.edu/

Table 2. The stellar parameters used to determine the habitable zone using the runaway greenhouse and maximum greenhouse parameters from Kopparapu et al. (2014) and the planetary orbits. The effective temperatures, parallaxes, and luminosities are all from *Gaia* DR2 (Gaia Collaboration 2018); the planetary parameters and stellar mass are determined in the references below. The table is ordered by the distance to the midpoint of the habitable zone.

System	Stellar Mass ($M_\odot$)	$T_{\rm eff}$ (K)	Luminosity ($L_\odot$)	Stellar Parallax (mas)	HZ mid-point (AU)	Planet Mass ($M_J \sin I$)	Semi-major axis (AU)	Eccentricity
[1]HD 114613	1.36	5709	4.44	49.3	2.79	0.48	5.16	0.25 ± 0.08
[2]HD 222155	1.21	5720	3.22	19.7	2.37	2.12	5.14	0.16 ± 0.22
[2]HD 72659	1.43	5898	2.38	19.2	2.01	3.85	4.75	0.22 ± 0.03
[3]ψ^1 Dra B	1.19	6213	2.11	43.9	1.85	1.53	4.43	0.4 ± 0.05
[4]HD 25171	1.09	6127	2.00	18.0	1.81	0.95	3.02	0.08 ± 0.06
[2]HD 24040	1.11	5805	1.89	21.4	1.80	3.86	4.92	0.04 ± 0.12
[2]HD 13931	1.30	5837	1.74	21.1	1.72	2.20	5.15	0.02 ± 0.04
[5]HD 220689	1.04	5944	1.50	21.3	1.59	1.06	3.36	0.16 ± 0.20
[2]HD 89307	1.27	5955	1.36	31.2	1.51	2.11	3.27	0.2 ± 0.05
[2]HD 86226	1.06	5924	1.23	21.9	1.44	0.92	2.84	0.15 ± 0.18
[6]HD 68402	1.12	5950	1.20	12.7	1.42	0.81	2.18	0.03 ± 0.06
[2]HD 27631	0.94	5732	1.10	19.9	1.38	1.45	3.25	0.12 ± 0.12
[7]HD 150706	1.17	5920	1.07	35.3	1.35	2.71	6.70	0.38 ± 0.3
[6]HD 152079	1.10	5722	1.04	11.3	1.34	2.18	3.98	0.52 ± 0.02
[2]HD 70642	0.96	5667	1.02	34.1	1.34	1.85	3.18	0.03 ± 0.08
[8]HD 32963	0.94	5746	1.01	26.2	1.32	0.70	3.41	0.07 ± 0.04
[5]HD 6718	1.08	5730	0.96	18.2	1.29	1.68	3.55	0.10 ± 0.08
[5]HD 142022	0.90	5487	0.89	29.1	1.27	4.44	2.93	0.53 ± 0.20
[9]HD 171238	0.81	5440	0.96	22.3	1.22	2.72	2.57	0.23 ± 0.03
[2]14 Her	0.90	5282	0.71	55.7	1.15	4.66	2.93	0.37 ± 0.01
[10]HD 102843	0.72	5346	0.72	15.9	1.15	0.36	4.07	0.11 ± 0.07
[4]HD 30669	0.92	5386	0.71	17.5	1.14	0.47	2.70	0.18 ± 0.30
[2]HD 290327	0.84	5545	0.73	17.7	1.14	2.43	3.43	0.08 ± 0.10
[9]HD 98736	0.92	5312	0.65	30.8	1.10	2.33	1.86	0.22 ± 0.064
[2]HD 95872	0.70	5180	0.57	132.2	1.04	3.74	5.15	0.06 ± 0.04
[2]HD 154345	0.71	5468	0.60	54.7	1.04	3.07	4.21	0.04 ± 0.05
[11]HD 42012	0.83	5342	0.54	27.1	1.00	1.60	1.67	0.07 ± 0.07†
[12]HD 25015	0.86	5079	0.41	26.7	0.89	4.48	6.19	0.39 ± 0.08
[13]ϵ Eri	0.83	4975	0.38	312.3	0.86	1.55	3.39	0.7 ± 0.04
[5]HD 166724	0.81	5101	0.39	22.1	0.86	3.53	5.42	0.73 ± 0.04
[2]HD 87883	0.67	4964	0.34	54.6	0.81	1.54	3.58	0.53 ± 0.12
[14]HD 164604	0.80	4684	0.26	25.4	0.73	2.7	1.3	0.24 ± 0.14
[2]BD-17 63	0.72	4669	0.22	29.0	0.67	2.85	2.85	0.54 ± 0.01
[15]GJ 328	0.69	3989	0.10	48.7	0.48	2.30	4.50	0.37 ± 0.05

Notes. [1]Wittenmyer et al. (2014), [2]Stassun, Collins & Gaudi (2017), [3]Endl et al. (2016), [4]Moutou et al. (2011), [5]Marmier et al. (2013), [6]Jenkins et al. (2017),[7]Boisse et al. (2012), [8]Rowan et al. (2016), [9]Ment et al. (2018), [10]Feng et al. (2019) [11]Rey et al. (2017), [12]Rickman et al. (2019), [13]Benedict et al. (2006) [14]Robertson et al. (2013),
†Note: HD 42012 is given with a 3σ upper bound of 0.2. We reformulate it as in the table to make consistent with the rest of the systems.

Group 3: Systems that could fit in either Group 1 or 2, due to the planets' having large uncertainties in their eccentricities.

4.2 Resilient habitability

4.2.1 Planets

To determine the resilient habitability we need to perform simulations that can represent the past dynamical evolution of an observed system. We postulate that any simulation of the system's past that ends with a massive planet having an eccentricity consistent with observations can be used to represent the system's history.

Fig. 1 shows that the outcomes of planet–planet scattering between planets of two different mass ratios (1:1 and 3:10) covers the entire range of observed eccentricities. We take these two mass ratios and construct two sets of initial conditions that contain planets with those ratios plus additional ones in order to capture secular effects during and after scattering. We call them 3E and 4H and they are set up as follows:

3E: This set contains three equal-mass planets, all with a mass equal to the $M_{\rm p}\sin I_{\rm p}$ of the observed planet.

4H: This set contains four planets with hierarchical masses, following the Solar System giants, with the innermost planet having a mass equal to the $M_{\rm p}\sin I_{\rm p}$ of the observed planet. We will refer to planets in this set as [lower case] jupiter, saturn, uranus, neptune.

We randomly pick the three Keplerian angles uniformly between 0 and 360° and draw random initial eccentricities uniformly from 0 to 0.01. The initial inclinations are drawn randomly between 0° and 5° which results in mutual inclinations between 0° and 10° with an average around 2°–3°: this is consistent with observations of Kepler multiple systems (Lissauer et al. 2011; Johansen et al. 2012). The planet radius is set following Bashi et al. (2017). Planets below $0.39 M_{\rm J}$ follow a relation of $R \propto M^{0.55}$ and planets with masses above it follow $R \propto M^{0.01}$ with the breakpoint radius being $1.1 R_{\rm J}$.

For each set in each system we place the innermost planet at two times the observed semimajor axis and initial separation between

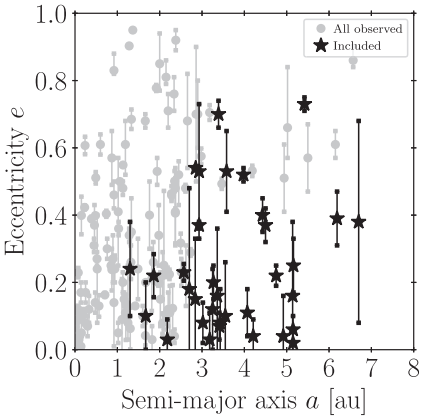

Figure 2. All of the known single-planet RV systems that meet our selection criteria for planet mass, and for stellar mass and radius. The black stars in the plot show the systems in Table 2; the grey markers are systems which meet the selection criteria but where the planet has an orbit that enters, is inside or interior to the habitable zone.

the planets is set to 3 mutual Hill radii in the 3E runs and 3.5 mutual hill radii for the 4H runs. The mutual Hill radius of two planets with masses M_1 and M_2 orbiting a star with mass $M_\star$ at semimajor axes of a_1 and a_2 is defined as:

$$R_{\rm MHill} = \left(\frac{M_1 + M_2}{3M_\star}\right)^{1/3} \frac{a_1 + a_2}{2}. \quad (3)$$

This small spacing is chosen in order to trigger the instability on a short time-scale, and to be computationally efficient. The time until the instability is triggered does not affect the duration of the scattering phase, as that is set by the orbital time-scale of the planets (Malmberg, Davies & Heggie 2011). Nor does it affect broadly the properties of the systems once they have stabilized following the ejection of one or more planets.

4.2.2 *Test particles*

In two-planet scattering one can narrowly constrain the expected range of final semimajor axes of the surviving planet by considering energy conservation (as seen in Fig. 1). When more planets are added, the final energy of the planets becomes less predictable and the expected range of semimajor axes is widened. Given that we are modelling a system where the planet has a specific semimajor axis we need to circumvent this. We do this by utilizing the fact that planetary dynamics are essentially scale free; i.e. if one takes a system and doubles all the semimajor axes it would almost always have the same exact dynamical outcome. The one exception is the probability of collisions, which decreases with increasing semimajor axis (Ford & Rasio 2008). We find them to be rare in our simulations (< 3 per cent) so this is not a concern. Given this,

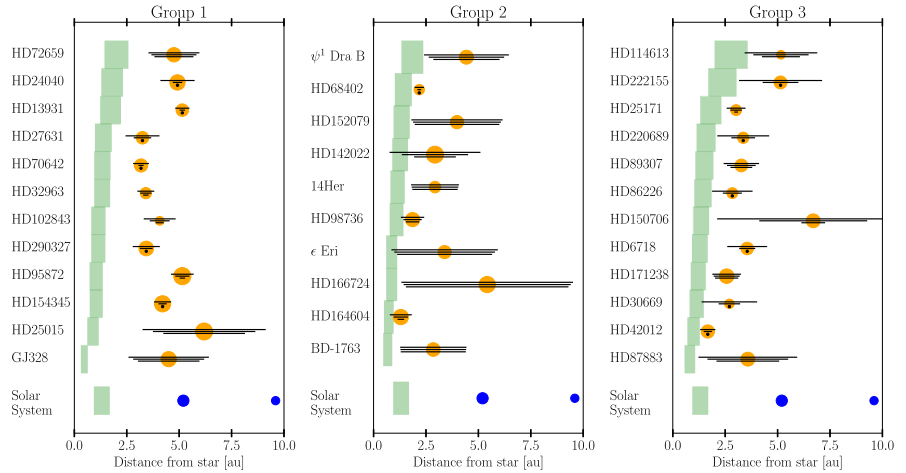

Figure 3. The planetary systems studied in our simulations. The planet is shown as an orange circle, where the area of the circle is proportional to $\sqrt{M_{\rm p}/M_\star}$. The black lines show the peri- and apocentre range of the orbit using the reported and $\pm 1\sigma$ values of the eccentricity. If the lower limit is consistent with zero, this is instead represented by a black dot. The green shaded area is the habitable zone calculated according to the formula from Kopparapu et al. (2014) (equations 1 and 2 of this paper). The systems are split into three categories, from left to right: Group 1 comprises systems with planets on distant orbits and/or with low eccentricity; Group 2 comprises systems with planets on nearby orbits and/or with high eccentricity; and Group 3 comprises systems where the planetary orbits have uncertain eccentricities that could place the systems in either Group 1 or Group 2. The Solar System is shown for scale at the bottom of each panel.

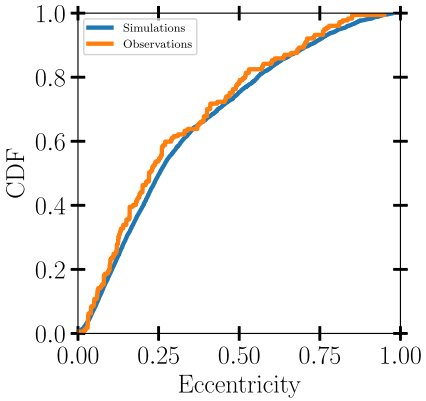

Figure 4. The cumulative distribution of exoplanet eccentricities. The observed RV sample is shown in orange. In blue we show the distribution arising from a 1:1 blend of the results of our two sets of simulations, 3E and 4H. For the 3E simulations we use the eccentricity of the innermost planet, while for the 4H simulations we use the eccentricity of jupiter which in ~ 97 per cent of the cases is also the innermost planet.

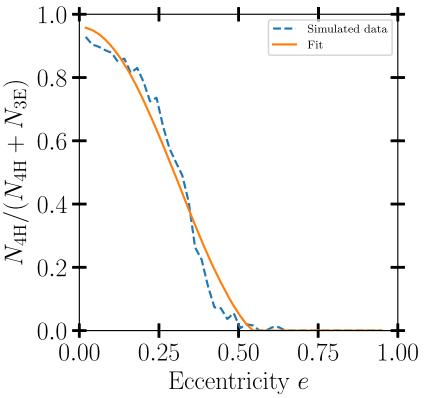

Figure 5. Here we show the fraction of initially 4H systems as a function of final eccentricity, when using the 1:1 global blend shown in Fig. 4. The blue dashed line shows the results from the simulations, while the solid orange line shows a polynomial fit.

we can rescale the semimajor axes of the remaining planets and the location of HZ according to the semimajor axis of the planet in the system we are modelling.

The post facto rescaling means that a larger range of test particles has to be included in the simulation. We place approximately 450 test particles (circular, coplanar, and randomly phased) between 0.8 times the inner edge of the HZ to 2.5 times the outer edge. The exact number is determined so the spacing between them is the same as in the previous experiment. Any realization (run) that ends with the rescaled location of the HZ outside where initially there were test particles is discarded.

Two changes are made to the simulation to ensure efficiency. First, the ejection distance is set to 250 au which ensures that test particles which clearly are not going to be habitable are removed in a timely fashion. Secondly, we remove any test particles that pass within 0.05 au of the host star. This removes highly eccentric test particles that would significantly slow down the integration during their pericentre passages.

We then run the simulations for 10^7 yr. Our initial conditions trigger the instability in less than 10^5 yr in all systems and the scattering phase rarely lasts more than 10^6 yr. This means that 10^7 yr is usually more than enough for the system to evolve and the phase of scattering to end. However, if there are test particles being ejected in the last Myr we run the simulation until there has been a Myr with no ejections.

The resilient habitability for each run is calculated by rescaling the location of the HZ by $a_{\rm final}/a_{\rm obs}$, checking which particles started with their semimajor axes in it and then seeing what fraction are left at the end.

5 RESULTS

As explained earlier, we considered the dynamical evolution of two kinds of planetary systems: 3E (where we have three planets of the same mass) and 4H (where we have four planets following the same ratio of masses of our own gas giants). For each system we investigated, we ran 100 simulations for each architecture following a phase of instability and planetary scattering: this ejected some planets and left the inner planet on a more eccentric orbit. In Section 2, we showed that scattering of a Jupiter and a Jupiter, and of a Jupiter and a Saturn, can between them span the observed eccentricity range. Therefore, we first consider the question: *what blend of 3E and 4H runs best matches the observed eccentricity distribution of all observed giant exoplanets?*

We determine the weighting by comparing the eccentricity distribution we find for the innermost planets in our simulations with observations. Our observational sample is taken from the exoplanet archive.[2] We select giant planets with masses in the range [0.3, 8]M_J and semimajor axes $a > 1.3$ au orbiting stars with masses [0.65, 1.4] $M_\odot$ resulting in a sample of 177 planets.

We generate 1000 eccentricity distributions for a range of 3E:4H ratios from the simulated eccentricities by randomly sampling them without replacement. We then perform a 2-sample KS-test between the observed eccentricities and our generated distribution. We find that randomly drawn distributions with 3E:4H ratios between 2:3 and 5:4 are consistent with the observations in more than 95 per cent of the cases, and we chose to use a 1:1 ratio. The comparison is shown in Fig. 4, and the resulting fraction of initially 4H systems as a function of eccentricity is shown in Fig. 5. Fig. 5 can also be interpreted as the probability of a system with a given reported eccentricity to initially have been a 4H system.

For each of the systems illustrated in Fig. 3, we modelled dynamical histories using both the 3E (three equal-mass planets) and 4H (four planets following the same ratio of masses of our own gas giants). For each system, we performed 100 runs for each of the 3E and 4H architectures. For further analysis, keeping those where the inner planet's orbital eccentricity matched that of the observed system (within the 1σ uncertainties for eccentricity).

[2] https://exoplanetarchive.ipac.caltech.edu/ as of 2019 February 11

We used the distribution shown in Fig. 5 to weight the 3E and 4H runs for each system to determine its $f_{\rm rhab}$ distribution. Often, the number of 3E and 4H runs that fall within the eccentricity range for a system do not match the expected fraction from fig. 5, given its eccentricity. This is because when determining the expected fraction as a function of the reported eccentricity we use the eccentricities at the end of our simulations ($e_{\rm final}$), whereas we allow for eccentricity oscillations (i.e. angular momentum exchange via secular interactions) when determining the $f_{\rm rhab}$-distribution. We allow for the oscillations because a number of runs would have ended up in the correct eccentricity range if the simulation had been stopped at a different time. After taking this into account we up-sample either the included 3E or 4H runs to give the correct ratio for the reported eccentricity of the observed system. Once we know which runs to use and how to re-sample them we determine the $f_{\rm rhab}$-distribution.

Fig. 6 shows the outcome of a subset of runs simulating HD 72659. The resilient habitability, i.e. the fraction of the test particles originally in the HZ remaining within the HZ at the end of the run, $f_{\rm rhab}$, for each run is shown in the panel on the right. The figure includes a correctly weighted combination of 4H and 3E runs, differentiated by the colour of the HZ where green represents 4H and light blue 3E. All of the runs have eccentricities consistent with the reported eccentricity, when we include secular eccentricity oscillations as described above. We show the configurations of the remaining planets for each of 48 runs, sorted in decreasing $f_{\rm rhab}$. Additionally we show at the top the initial configurations for 3E and 4H. The colour labelling for the initial configuration and the final 48 systems is the same. For each planet, the location of the circle denotes the semimajor axis whilst the error bars denote the maximum and minimum distances from the host star. The light backgrounds show the range of the giant planet semimajor axes (light blue) or positions (light red) over the course of each run, sampled every 10 kyr.

We see a clear difference between the 3E and 4H runs: 4H gives a broad range of $f_{\rm rhab}$ values, even when looking at runs with similar eccentricities: while the upper quartile have $f_{\rm rhab} \approx 0.75$–1, others show much smaller values of $f_{\rm rhab}$. On the other hand, for the 3E runs we see that in most cases $f_{\rm rhab} \approx 0$; we see that the vast majority of the twelve 3E runs shown are located at the bottom of the distribution. Massive planets have directly invaded the HZ in about one half of the 3E runs, leading in all these cases to the essentially complete removal of test particles. However, we see a few examples of 4H runs where the HZ is invaded without equally destructive outcomes. This is because the planet in question was of much lower mass (roughly that of Neptune). In a large fraction of runs we can see that test particles have been ejected even though a planet never entered the HZ. This, along with the gaps seen in the test particle distribution in nearly every run, can be explained by resonances which are pumping up the eccentricities of the test particles. A detailed discussion of the resonances will follow in Section 6.1.

5.1 $f_{\rm rhab}$ and $f_{\rm hab,\,1p}$ distributions for the three groups

As can be seen in Fig. 6, runs for a given system can show a very broad range of values of $f_{\rm rhab}$. Therefore for each system, we plot the range of values of $f_{\rm rhab}$ (the 1σ-equivalent range, i.e. the central 68 per cent of the distribution) in Fig. 7, together with the present-day habitability simulations, $f_{\rm hab,\,1P}$, in black. The systems are separated into the three Groups as shown in Fig. 3. We consider the results of each Group in turn.

5.1.1 Group 1 systems

Group 1 (left-hand panel in Fig. 7) contains systems where the planet has a considerably larger semimajor axis than the outer edge of the HZ and a low eccentricity, or has a moderate eccentricity with a much larger semimajor axis. All of the systems show high values of $f_{\rm hab,\,1P}$: usually essentially unity. In all cases the mean value of $f_{\rm rhab}$ is lower and the distribution shows a broader range of values.

For the three systems with higher eccentricities (HD 72659, GJ 328, and HD 25015) the width of the distribution can be understood by considering Figs 5 and 6. The higher the observed eccentricity, the larger the fraction of 3E runs contributing to the $f_{\rm rhab}$ distribution. We have seen that 3E runs tend to be a lot more disruptive to test particle orbits. However, GJ 328 and HD 25015 differ from all the other Group 1 systems in that the giant is considerably more distant from the HZ, resulting in nearly all of the 4H runs along with a significant fraction of the 3E runs giving $f_{\rm rhab} \approx 0.9$.

The other systems in Group 1 are all at low eccentricities and the $f_{\rm rhab}$ distribution is therefore dominated by 4H runs. The width of the 1σ-range comes from the diversity of outcomes of the 4H runs, which can be seen in Fig. 6. More specifically, for the 4H runs we find that 40 per cent of the runs have $f_{\rm rhab} \approx 1$ with the rest of them fairly evenly spread between 0 and 1. Fig. 8 shows the distribution of $e_{\rm final}$ and $f_{\rm rhab}$ for all the runs. We see that low eccentricities have a mix of low and high values of $f_{\rm rhab}$ whilst eccentricities above 0.5 give only very low values of $f_{\rm rhab}$. Some 17 per cent of runs yield $f_{\rm rhab} > 0.9$ whilst 46 per cent of runs result in $f_{\rm rhab} < 0.1$. The distribution for an individual system can often deviate from the average of all runs shown here. The eccentricity at which the peaks appear is set by the underlying eccentricity distribution resulting from the planet–planet scattering. A larger planet/star mass ratio shifts the peaks to higher eccentricities. The relative strength of each peak is set by the distance between the HZ and planet in terms of Hill radii. 4H runs in systems with distant planets such as HD 95872 nearly always have $f_{\rm rhab} > 0.95$ and for the 3E runs such systems (and only those) have a fraction of runs showing high survival. Systems where the planet sits close to the HZ like HD 72659 do the opposite. The 4H runs are distributed fairly evenly between $f_{\rm rhab} = 0$ and $f_{\rm rhab} = 0.95$ and the 3E runs are always fully destructive.

5.1.2 Group 2 systems

Group 2 (middle panel in Fig. 7) contains systems where the planet has a semimajor axis just outside the outer edge of the HZ with a low to moderate eccentricity, or has a larger semimajor axis with a sufficiently high eccentricity to bring the pericentre very close to the HZ. Such planets are more destructive to objects within the HZ. Other than HD 68402 all of the systems have a low $f_{\rm hab,\,1P}$ and even lower $f_{\rm rhab}$. The reason for this can be understood by considering Fig. 8. The high eccentricity systems only include runs from a region in the plot where there are no runs with high $f_{\rm rhab}$, whereas the moderately eccentric ones that sit closer to the HZ have 4H runs that are shifted to significantly lower $f_{\rm rhab}$ values as discussed in the previous subsection for the Group 1 systems.

The outlier, HD 68402, is a low-mass giant sitting very close to the HZ on a nearly circular orbit. In its present day orbit it does very little damage to the HZ; however, during the scattering any eccentricity fluctuations or changes to its semimajor axis easily destabilize test-particle orbits in the HZ. HD 68402 clearly demonstrates how much the history of a system can matter.

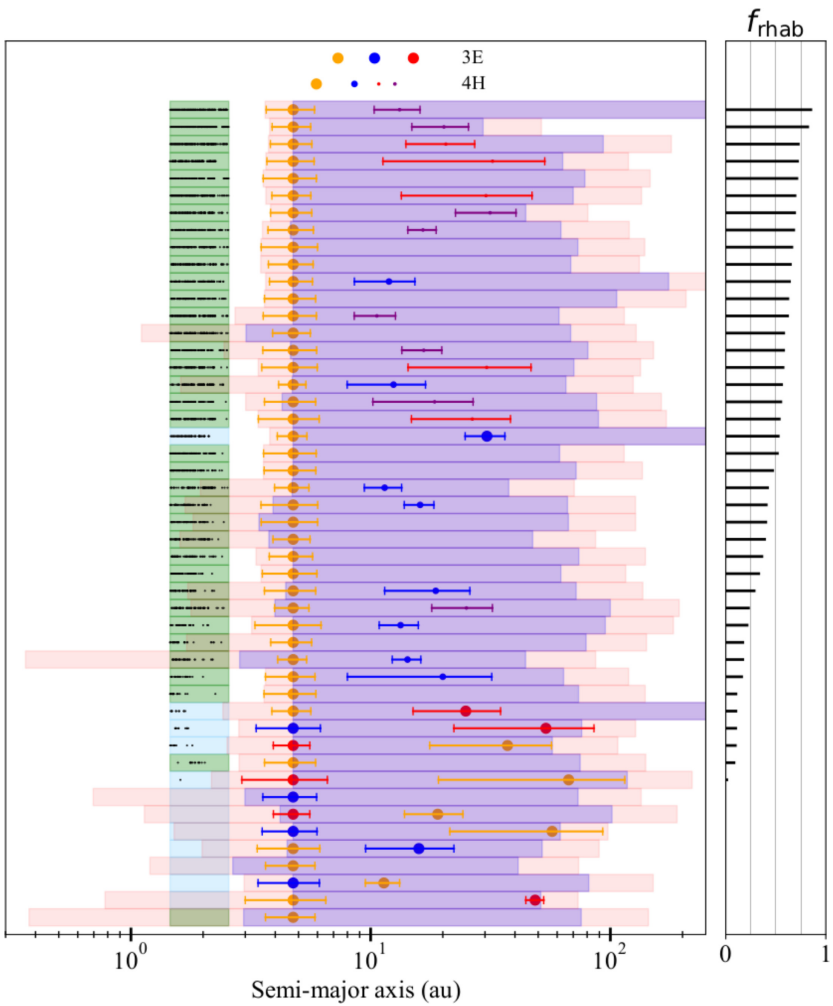

Figure 6. The figure shows the outcome of a set of runs for HD 72659. The habitable zone is shown by the shaded rectangle around 2 au: green for the 4H runs and cyan for the 3E runs. Coloured circles show the final semimajor axes of the planets, with the error bars indicating their pericentre and apocentre values. The planets' initial locations, with the same colouration, are shown at the top of the figure. The final semimajor axes of the test particles are shown as small points, blue for those that contribute to f_{rhab} and grey for those that do not. The shaded blue region shows the range of the planets' semimajor axes during the integration, with output sampled every 10 kyr, and the peach region shows the range of the planets' pericentres and apocentres, also sampled every 10 kyr. Finally, the panel to the right shows the f_{rhab} value for each system.

5.1.3 Group 3 systems

Group 3 contains the systems with a large uncertainty in the reported eccentricity of the planet and could therefore fall in either Group 1 or Group 2. Given that we include runs that are within one standard deviation of the reported eccentricity some time after the final planet ejection occurs, we are including runs from a much wider eccentricity range. We perform a second determination of the f_{rhab} distribution, in which we pick runs close to the reported value of the

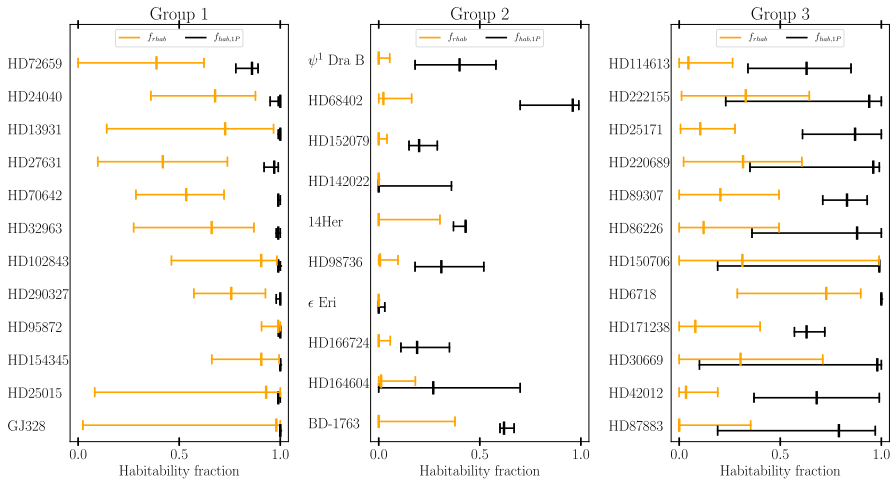

Figure 7. The present day and resilient habitability of all the systems. The black line indicates the present-day habitability of the systems, in the configuration shown in Fig. 3. The mid-point on the line show the survival fraction found when simulating using the reported eccentricity and the endpoints are the result of using $\pm 1\sigma$ values. The orange line shows the median and '1σ range' (i.e. the central 68 per cent of the distribution) of the $f_{\rm rhab}$ distribution for each system, using the blending ratio given by the reported eccentricity (see Fig. 5).

observed eccentricity, and within 0.5σ of the -1σ and $+1\sigma$ values (orange, red, and blue colours in Fig. 9).

The large eccentricity range means that we get a large sample of both 3E and 4H runs which widens the distribution. Not all distributions in Fig. 9 are narrower than the corresponding ones in Fig. 7; however in a subset of them the majority of 3E runs get relegated to the high e distribution (blue line in Fig. 9). This often shifts the other two distributions (orange and red lines) to higher values, in particular for HD 150706. If its actual eccentricity is close to the lower end it is one of the most resilient systems we have looked at. If it is at the high end, the opposite is true.

6 DISCUSSION

6.1 Mechanisms responsible for the removal of particles from the HZ

We have shown that particles orbiting in a star's HZ can themselves be destabilized during an instability among its giant planets. We now look in more detail at the physical mechanisms responsible for removing particles from the HZ. This differs depending on whether the outer system is an equal-mass 3E configuration, or a hierarchical 4H configuration.

The 3E runs frequently give $f_{\rm rhab} \sim 0$ as a $\sim$ Jupiter-mass planet is often scattered into the HZ. This results in most test particles being directly gravitationally scattered and then ejected from the system: around 80 per cent of the test particles removed from the HZ in the 3E runs have a close encounter in the HZ with one or more planets.

In contrast, in the 4H runs jupiter only ever enters the HZ in systems where it is initially located very close to it. However, we still see $f_{\rm rhab} \approx 0$ runs in systems where this is not the case. This happens in one of three ways:

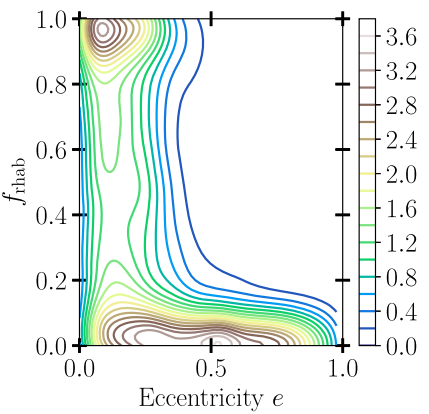

Figure 8. A kernel density estimate showing the resulting $f_{\rm rhab}$ values for all our runs, both 3E and 4H, plotted against the final eccentricity of the planet.

(i) Saturn gets scattered into a HZ crossing orbit and ejects most of the test particles (rare).

(ii) Uranus or neptune gets scattered into a HZ crossing orbit and stays there for some time. This increases the eccentricity of the test particles which are later ejected by jupiter (less rare).

(iii) Resonances from jupiter inside the HZ excite the eccentricities of test particles which are later ejected by jupiter (common).

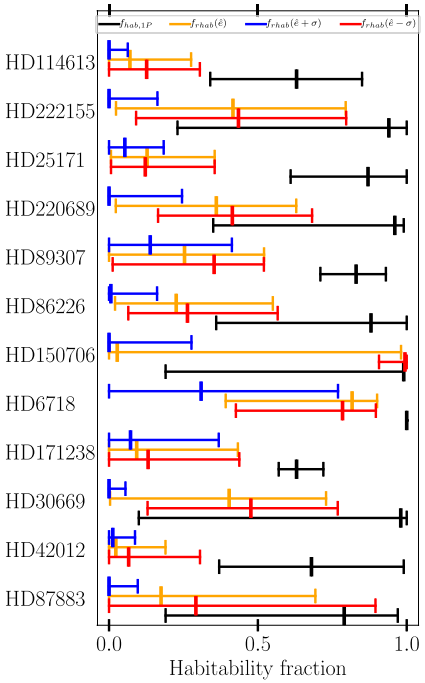

Figure 9. The resilient habitability for systems with large uncertainties in the eccentricity of the gas giant. The three $f_{\rm rhab}$ distributions are generated using runs close to the $-\sigma$ (red), mean (orange), and $+\sigma$ (blue) values of the eccentricity. The black line shows $f_{\rm hab,\ 1P}$, as in Fig. 7.

Examining the close encounter history of the test particles, we find that 60 per cent of all the ejected test particles in the 4H runs never experience a close encounter with a planet that takes places within the HZ. Rather, their eccentricities are excited by orbital resonances with the giant planets, after which they are typically removed by gravitational scattering once their apocentre brings them close to jupiter. Matsumura et al. (2013) and Carrera et al. (2016) identified secular resonances as being of importance in pumping up particle eccentricities during scattering amongst outer giant planets. Here, we show that for our systems mean-motion resonances (MMRs) with jupiter can be more significant. We discuss the effects of secular resonances in Section 6.2.

MMRs occur when the orbital periods of two bodies lie close to a ratio of integers. Here we consider 1: m and 2: m resonances between a test particle in the HZ and the jupiter. These occur where the semimajor axis of the particle in the HZ lies at $a = (1/m)^{2/3}a_{\rm J}$ or $a = (2/m)^{2/3}a_{\rm J}$, where $a_{\rm J}$ is the semimajor axis of the jupiter. Therefore, as the jupiter's semimajor axis moves erratically inwards as it scatters and ejects the outer planets, the mean motion resonances jump through the habitable zone.

We illustrate the effects of the passage of MMRs by comparing two runs from our 4H simulations of HD 72659. One run has a high and one a low $f_{\rm rhab}$. In neither run did a planet enter the HZ, and both end with the jupiter possessing a similar eccentricity.

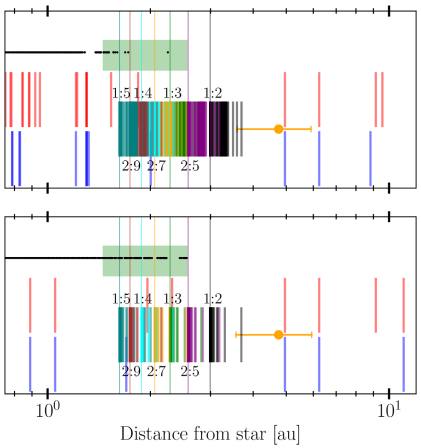

Figure 10. The figures show how the location of orbital resonances changes with time for two different 4H runs of HD 72659. The final location of the planet is shown in amber, the circle marking its semimajor axis and the error bars its pericentre and apocentre; the habitable zone is shown in green, and surviving test particles as small black points. The vertical lines mark the location of orbital resonances, sampled every 10 kyr. The off-axis red and blue lines show the location of the secular eccentricity and inclination resonances. The remaining coloured lines show the 1: m and 2: m mean motion resonances with the long line being placed at the final location of the resonance.

The motion of the resonances in these two runs is shown in Fig. 10. Here the final location of the planet is shown in amber, and the HZ in green. Vertical lines mark the locations of MMRs and secular resonances, sampled every 10 kyr, with the final locations of the MMRs marked as long vertical lines. The final location of each resonance lies at the innermost edge of its range over the integration, as expected from the net inward motion of the jupiter.

In the upper panel of Fig. 10, we illustrate a case where the jupiter moves inwards through a slow, incremental process. The sampled locations of the resonances lie dense in the habitable zone, meaning that particles at most semimajor axes in the HZ have time for their eccentricities to be highly excited by one or more resonances. Indeed, particles are found surviving the simulation at only a few semimajor axes, mostly towards the inner edge of the HZ. In the bottom panel, in contrast, the jupiter moves inwards more rapidly, meaning that a significant fraction of the HZ does not become excited by the passage of MMRs, and many particles survive the integration. These two examples suggest a dependence of a system's resilient habitability $f_{\rm rhab}$ on the nature of the motion of the jupiter.

We have explored a number of different parametrizations to correlate the evolution of jupiter's semimajor axis with $f_{\rm rhab}$. We find that looking at the fractional absolute change in semimajor axis between each output time (10 kyr resolution) shows this dependence best. The fractional absolute change is given in the form

$$\frac{\Delta a}{a} = \sum_i \frac{|a_{i+1} - a_i|}{a_i}, \tag{4}$$

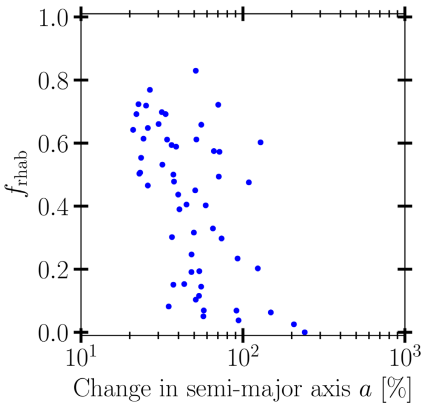

Figure 11. $f_{\rm rhab}$ as a function of the summed up absolute fractional change in semimajor axis for all 65 of the 4H-runs of HD 72659 where no planet enters the HZ. The change in semimajor axis is defined by equation (4).

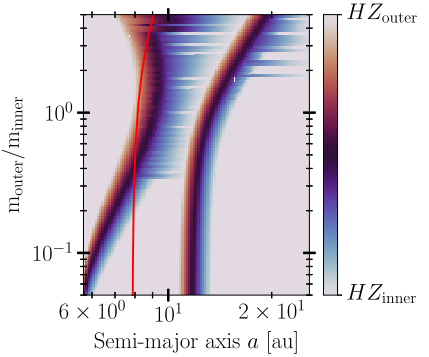

Figure 12. For the system HD 95872 ($a = 4.75$ au) the figure shows at what semimajor axis a planet of a given mass needs to be placed for either of the secular eccentricity resonances to be in the HZ. The colour indicates where in the HZ the resonance appears. The red line shows the Gladman stability limit for circular orbits: systems wider then this cannot experience orbit-crossing.

where a_i is the semimajor axis at the ith output. Thus, a jupiter that attains its final semimajor axis in a few large jumps will have a small $\Delta a/a$, while those that move in many small steps, which often involves temporary reversals of direction, will have a large $\Delta a/a$. We plot in Fig. 11 the resilient habitability for HD 72659 against $\Delta a/a$, for all 4H runs where no planet entered the HZ. As expected, we see an anticorrelation between $f_{\rm rhab}$ and $\Delta a/a$.

Combining the anticorrelation we see in Fig. 11 with the fact that 60 per cent of ejected test particles in 4H runs never have a close encounter inside the HZ, we conclude that the majority of test particles in the 4H case are ejected due to MMRs sweeping over the HZ. The ejection efficiency is correlated with how much the semimajor axis of jupiter changes.

6.2 Secular resonances in the habitable zone during and after an instability

One way through which eccentricities can be forced to high values in the absence of direct scattering is through secular resonances. Secular resonances occur when the precession frequency of one of the particles in the HZ matches one of the secular eigenfrequencies of the giant planets. These resonances occur at specific values of the particles' semimajor axis, and formally the forced eccentricity is infinite at these locations. Because the planetary secular frequencies are dependent on their semimajor axes, the frequencies change during planet–planet scattering, and so the secular resonances also move. This process was identified by Matsumura et al. (2013) and Carrera et al. (2016) as a means of destabilizing terrestrial planets during an instability amongst giant planets.

Returning to Fig. 10, we have plotted the location of the secular resonances (both eccentricity and inclination) in the two runs every 10 kyr. The resonance locations are calculated according to linear Laplace–Lagrange theory (Murray & Dermott 1999, Ch. 7). They move inwards as the planets' semimajor axes change during scattering, similar to the motion of the MMRs, but in contrast to the MMRs they move much further and more rapidly. This is because they depend on the semimajor axes of all planets, not just the jupiter; but the jupiter alone sets the location of the MMRs and itself moves comparatively little. Indeed, the secular resonances pass across the whole HZ in just a few 10s of kyr, insufficient time to significantly affect particles' eccentricities. Typically the secular resonances pass through the HZ in less than 30 kyr, and only in ~ 5 per cent of runs do they spend more than 100 kyr in the HZ. In the upper panel we do, however, see that the secular eccentricity and inclination resonances remain for several 10 s of kyr just interior to the HZ, where they destabilize a few bodies and knock a small hole in the distribution of survivors.

While in principle the final giant planet configuration following scattering could leave a secular resonance in the HZ, this is very rare, occurring in $\lesssim 1$ per cent of our runs. The reason is that the planets must be spaced rather close to each other to place a secular resonance in the HZ. We show in Fig. 12 where the secular eccentricity resonances would lie in the HD 95872 system if it contained a second giant planet, as a function of this planet's mass and semimajor axis. To place a secular resonance in the HZ requires a separation of $\sim$4−7 mutual Hill radii between the planets. These configurations would be stable if the planets' orbits were near-circular, as they satisfy the limit for Hill stability given by Gladman (1993):

$$\frac{a_{\rm outer} - a_{\rm inner}}{R_{\rm MHill}} > 2\sqrt{3}, \tag{5}$$

where $R_{\rm MHill}$ is the mutual Hill radius from equation (3) and $a_{\rm outer}$, $a_{\rm inner}$ are the semimajor axes of the planets. We mark this limit in Fig. 12 as a solid red line. While the circular configurations would be stable, scattering often leaves planets with significant eccentricities, and this significantly increases the separation required for the planets to remain stable after scattering (e.g. Mardling & Aarseth 2001; Mustill & Wyatt 2012; Giuppone, Morais & Correia 2013; Petrovich 2015; Antoniadou & Voyatzis 2016; Hadden & Lithwick 2018).

6.3 Low-eccentricity systems

For the low-eccentricity systems we have to consider whether or not the system has been through a phase of planet–planet scattering,

and in either case, what the value of $f_{\rm rhab}$ will be. If the system has undergone an instability, then the answer is given in Fig. 7. If there has not been any scattering the only way in which $f_{\rm rhab}$ could be significantly different from $f_{\rm hab,\,1P}$ is if there is an additional hitherto undetected planet in the system. This can affect the system either through changing the eccentricity of the observed planet over time, or by giving rise to secular resonances inside the HZ as we have just discussed.

6.3.1 Eccentricity changing with time

Secular interactions lead to eccentricities varying with time. These variations occur on time-scales of thousands of years, therefore the $f_{\rm hab,\,1P}$-simulations do not necessarily capture the full picture. In particular, a planet with a low eccentricity at the present day may be at the low point of a secular cycle, if there is an undetected exterior planet currently on an eccentric orbit.

We test how damaging this can be by determining what we call $f_{\rm hab,\,2P}$: here, we take systems where two planets survive our 4H runs and the jupiter has an eccentricity consistent with the observed system, repopulate the HZ with low-eccentricity test particles, and run the system for 10 Myr. $f_{\rm hab,\,2P}$ is then the fraction of these repopulated test particles that survive the integration. By choosing two-planet systems from among our post-scattering configurations, where the outer planet often has a highly eccentric orbit, we are generating systems where we might expect that a large eccentricity can be passed to the inner planet through secular interactions, and so where $f_{\rm hab,\,2P}$ will be low.

However, what we find is that in most cases the variation of the inner planet's eccentricity is smaller than its observational uncertainty, and that the $f_{\rm hab,\,2P}$ values lie mostly within the range of $f_{\rm hab,\,1P}$ in Fig. 7. $f_{\rm hab,\,2P}$ is lower if the mean eccentricity of the jupiter over its secular cycles is higher than the reported value, and lower if the reverse is true. In a few per cent of cases, the eccentricity of the jupiter at the end of the original integration (the start of the repopulated integration) is close to the minimum or the maximum in its cycle, and in these cases, $f_{\rm hab,\,2P}$ can differ significantly from $f_{\rm hab,\,1P}$.

We now return to the focus of this sub-section: low-eccentricity planets that have not undergone instability. The amplitude of the inner planet's eccentricity oscillations is larger if the outer planet's eccentricity is larger, and so systems that have not undergone instability will usually have values of $f_{\rm hab,\,2P}$ similar to their values of $f_{\rm hab,\,1P}$, since this is usually the case for more dynamically excited systems too.

6.3.2 Placing the secular resonances in the habitable zone

Nevertheless, there is a potential exception to the fact that systems that have never undergone planet–planet scattering will have a high $f_{\rm hab,\,2P}$: this is if they have secular resonances in the HZ. We test the effect that such secular resonances can have by setting up runs for the HD 95872 and HD 72659 systems, adding a planet of equal mass on a circular orbit at a semimajor axis that places a secular resonance in the HZ, populating the HZ with test particles, and integrating the system for 10 Myr, verifying that the two planets are stable.

For HD 95872 we find that $f_{\rm hab,\,2P}$ is as high as $f_{\rm hab,\,1P}$ when we place a secular resonance in the HZ; however, a large fraction of the test particles in the HZ acquire high eccentricities above 0.5. As we discuss in Section 6.4, these high eccentricities are likely detrimental to any planet's habitability. The secular resonance in this system is especially strong because of the large planet mass relative to the star (3.74 M_J versus 0.7 $M_\odot$). In HD 72659, the test particles that have large eccentricities excited eventually get ejected, since the giant planet's pericentre is close to the HZ. HD 95872 and HD 72659 show, respectively, the highest and the lowest values of both $f_{\rm hab,\,1P}$ and $f_{\rm rhab}$, showing that the effects of secular resonances could be significant for many systems.

As discussed above, it is less likely that systems with high-eccentricity planets have secular resonances in the HZ because of the constraints imposed by stability of the gas giants. In answering the question 'how likely is a HZ to be destabilized by a secular resonance?', we therefore have a curious inverse dependence on eccentricity, where the systems with more eccentric giant planets are less likely to have their HZ destabilized by a secular resonance. This does, however, ignore the scattering history of the giant planets, which may have destabilized bodies in the HZ by scattering and the passage of MMRs.

6.4 The effect of eccentricity on habitability

The HZ is defined as the spherical shell around a star at which the flux received allows for liquid water to exist on the surface of the planet under a set of atmospheric conditions. In our simulations we have hitherto considered only whether the semimajor axis remains in the HZ, ignoring any orbital eccentricity the planet may possess.

At some point this approximation breaks down and we have to consider the effects of having large temperature differences between peri- and apocentre. In general, the higher the orbital eccentricity at a given semimajor axis, the higher the orbit-averaged radiation flux from the star: therefore, the HZ is more distant at higher eccentricity. While simple energy-balance arguments give a dependence of the HZ on eccentricity of $a_{\rm HZ} \propto (1 - e^2)^{-1/4}$, more detailed modelling (e.g. Dressing et al. 2010; Spiegel et al. 2010; Linsenmeier, Pascale & Lucarini 2015; Bolmont et al. 2016; Kane & Torres 2017), incorporating the effects of planetary spin rate and obliquity, shows that high eccentricities ($e \gtrsim 0.5$) can have a significantly stronger effect.

As the actual effect of eccentricity depends on other parameters such as the spin rate and obliquity, we explore the number of stable particles that attain a specified value of eccentricity, $e_{\rm lim}$, at any point in the run. We then recalculate the resilient habitability $f_{\rm rhab}$ by excluding the particles that reached a high eccentricity, assuming that they have been rendered uninhabitable. By performing this calculation for a range of $e_{\rm lim}$, we can find how significantly the inclusion of an eccentricity consideration affects $f_{\rm rhab}$, without committing ourselves to a single (model-dependent) eccentricity limit. We then show in Fig. 13 the ratio of $f_{\rm rhab}$ with the eccentricity limit to that without. As expected, this rises from zero at $e_{\rm lim} = 0$ (all particles are considered uninhabitable when they acquire any eccentricity) to unity at $e_{\rm lim} = 1$ (all surviving particles are considered habitable, regardless of eccentricity). For $e_{\rm lim} = 0.5$, about 30 per cent of surviving particles are rendered uninhabitable by acquiring eccentricities above $e_{\rm lim}$. This is a significant reduction in resilient habitability, motivating further studies of the climate of highly eccentric terrestrial planets.

6.5 Additional considerations

6.5.1 Multiple massive terrestrial planets

We have used mass-less test particles to represent terrestrial planets in our simulations. This is computationally efficient as one can simulate many hundreds of test particles within one single run. The

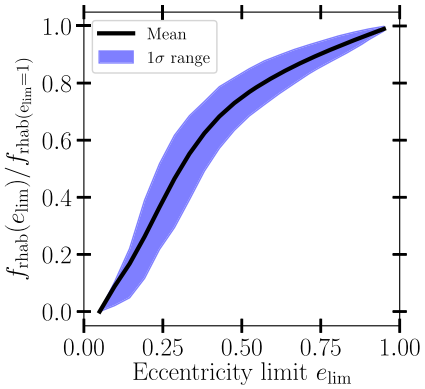

Figure 13. The change in $f_{\rm rhab}$ for all systems when an eccentricity limit is imposed on the habitability. For each value of $e_{\rm lim}$ we recalculate $f_{\rm rhab}$ and do not count any test particle towards it that reaches an eccentricity greater than $e_{\rm lim}$ throughout the run. The 1σ error band shows the standard deviation over all runs of all systems.

total mass of the terrestrial planets is $\lesssim 1$ per cent of that of the giant planets, so using test particles to represent massive terrestrial planets should not be a problem when considering the direct interactions between the particles and the giant planets. However, use of massless non-interacting test particles means that we do not account for any interactions between the habitable planets, should more than one be present.

In principle, if there are multiple terrestrial planets close to each other they can couple to each other and counteract external perturbations. The stabilization by such couplings has been confirmed for both the Solar System (see e.g. Innanen et al. 1997; Batygin & Laughlin 2008; Laskar & Gastineau 2009; Zeebe 2015), and generally for tightly packed systems (see e.g. Malmberg et al. 2011; Kaib, Raymond & Duncan 2011; Hansen 2017; Mustill, Davies & Johansen 2017; Denham et al. 2019). The key factor determining whether the system is stabilized is the time-scale. If the coupling between the planets is on a short time-scale compared to the perturbation the planets will be resistant to it. Thus, we might expect the resilient habitability of systems to increase if the test particles are replaced with a handful of massive planets.

On the other hand, Carrera et al. (2016) investigated the resilient habitability of systems where the HZ was populated either by a swarm of test particles, or by one, two or four massive ($1\,{\rm M}_\oplus$) planets. As expected, the survival rate of the single planets is consistent with that of the test particles, but the survival of HZ planets in the systems of two or four terrestrial planets is in fact lower than that of the test particles. In practice then, multiplanet systems subject to strong scattering from an outer system are slightly more vulnerable and more likely to be destabilized, although in systems with weaker external forcing it is likely that the protective coupling can still stabilize the system.

6.5.2 *The timing of the instability*

It is thought that terrestrial planets usually take $10-100\,{\rm Myr}$ until they are fully formed. This time-scale is typical in simulations of terrestrial planet formation from swarms of planetary embryos (Chambers 2001; O'Brien, Morbidelli & Levison 2006; Hansen 2009; Raymond et al. 2009; Lambrechts et al. 2019), and agrees with radiogenic dating of the Earth and Moon (Jacobsen 2005; Halliday 2008). On the other hand, gas giants must form in a few Myr while the gas disc is still present (Machida et al. 2010; Piso & Youdin 2014; Piso, Youdin & Murray-Clay 2015; Bitsch et al. 2019). The instability amongst the giant planets occurs some time after they have formed. It is a steep function of their orbital separation, and the time-scale of onset at a given separation can vary by an order of magnitude (Chambers, Wetherill & Boss 1996; Shikita, Koyama & Yamada 2010). Therefore, the instability can take place before or after terrestrial planet formation is complete. Indeed, in consistent simulations of formation, migration, and dynamics, Bitsch et al. (2019) found that 5 per cent of the giant planet systems they formed were unstable on time-scales $<10\,{\rm Myr}$.

Thus, depending on the timing of the instability, the terrestrial planets may be fully formed or may still be a swarm of embryos. Whether the test particles in our simulations are considered to represent fully formed planets or planetary embryos leads to two different interpretations.

If the instability happens after terrestrial planet formation has finished, then each particle lost from the simulations represents one of a handful of fully formed planets. Each run can then be interpreted as simulating a large number of different realizations of an inner terrestrial planet subject to the same forcing from the unstable gas giants. Thus, a value of $f_{\rm rhab}$ of 25 per cent simply means that on average one quarter of planets would be retained and three quarters lost. If multiple fully formed terrestrial planets are present in the same system, then their mutual interactions can affect the dynamics: Carrera et al. (2016) showed that this results in a lower fraction of planets surviving.

On the other hand, if the instability occurs before terrestrial planet formation is completed, our test particles can more readily be interpreted as representing the swarm of planetary embryos present in the HZ in one system. Thus, a value of $f_{\rm rhab}$ of 25 per cent now means that the HZ loses three quarters of its embryos. Depending on their distribution and excitation, terrestrial planet formation may not be able to proceed all the way to Earth mass, but may stall at smaller masses as much of the available material can be ejected from the system during the instability. An additional complication concerns the outcome of collisions between embryos: when excited by an instability in the outer system, collision velocities increase and collisions between embryos result in significant mass-loss (Mustill, Davies & Johansen 2018). This can reduce the final size of the terrestrial planets still further, if the ejecta is ground down and removed by radiation pressure before being reaccreted by one of the embryos.

6.5.3 *RV mischaracterization of planet eccentricity*

The signal from a planet with a seemingly eccentric orbit may, in some circumstances, actually be generated by a planet on a circular orbit. There are two ways in which this could happen. The first arises from the fact that eccentricity is a positive-definite quantity: it cannot be negative. Therefore, the fitted eccentricities for planets on circular or low-eccentricity orbits are biased towards higher values (Lucy & Sweeney 1971; Shen & Turner 2008; Zakamska, Pan & Ford 2011; Hara et al. 2019). For example, Zakamska et al. (2011) show that the fraction of low eccentricity systems could be underestimated by as much as a factor of 3. This means that the

true values of the resilient habitability for some of our systems may be higher than we have calculated, as the known planets' eccentricities may be somewhat smaller than the reported literature values.

The second way in which a seemingly eccentric signal can be generated by a planet on a circular orbit is through the presence of an interior, lower mass planet at a 2:1 period ratio. Anglada-Escudé, López-Morales & Chambers (2010) showed that two such planets show a similar and sometimes indistinguishable RV signal as only having the outer, more massive planet on an eccentric orbit. They show that the RV signal from as many as 35 per cent of observed eccentric single planet systems show no statistically significant difference from being two planets in a 2:1 configuration rather than a single eccentric planet. Further, Wittenmyer et al. (2019) sets an upper bound on the possible apparent eccentricity at 0.5.

We first make a simple estimation of the destructive effects on the HZ of a single eccentric planet compared to two planets in a 2:1 configuration. We estimate the mass of the inner companion required to mimic an eccentric orbit from fig. 3 of Kürster et al. (2015), and compare the potential for direct scattering in both configurations, comparing the reach of the Hill radius of the inner planet $a_{\rm in} - r_{\rm H,\,in}$ with that of the seemingly eccentric outer planet at pericentre $a_{\rm out}(1 - e_{\rm out}) - r_{\rm H,\,out}$. We find that the eccentric outer planet will be more effective at direct scattering than the 2:1 two-planet configuration.

We test this with a set of simulations and find that systems with $e < 0.3$ also can be more damaging than their 2:1 equivalent. This occurs if the pericentre distance to the outer edge of the HZ is smaller than the distance from the extra interior planet to the edge in terms of Hill's radii. This is the case for nearly all systems in this range that are fairly close to the HZ, barring the ones where the 2:1 resonance sits inside the HZ which already show low $f_{\rm hab,\,1P}$ and mostly $f_{\rm rhab} = 0$. The most resilient and distant systems such as HD 95872 show no difference when replaced with the 2:1 equivalent.

6.5.4 *Planet masses and multiplicities*

We now consider two complications to our treatment of the planet masses in our simulations. First, we have set the planet masses in the simulations to equal $M\sin I$ of the observed planet, which on average will underestimate the planet mass by a factor of 1.6, and is a strict lower limit on the mass. To explore the effect of the true mass being higher, we have re-run the single-planet simulations (to calculate $f_{\rm hab,\,1P}$) for HD 95872 and HD 72659 with planetary masses increased by factors of 1.4, 1.7, and 2.0. For HD 95872 there is no difference in the outcome. For HD 72659, where the giant's pericentre is closer to the HZ, we find a small reduction in $f_{\rm hab,\,1P}$ of 0.02–0.06. A larger mass is marginally more disruptive if the pericentre is within a few Hill radii of the HZ, but because the Hill radius is a weak function of mass (equation 3) the effect is not very strong.

When considering $f_{\rm rhab}$, we expect that the peak of the eccentricity distribution after scattering will shift to slightly higher values with increasing planet–star mass ratio. However, we also expect that the mass ratio *between* planets in the system is more significant in setting the final eccentricity distribution and the history of scattering. We note here that soon *Gaia* will provide a measure of the true mass of many Jupiter analogues (Sozzetti et al. 2008; Perryman et al. 2014; Ranalli et al. 2018), permitting a refinement to the estimation of $f_{\rm hab,\,1P}$ and $f_{\rm rhab}$ by repeating these simulations with the real planetary masses.

The second complication is that we have reduced the set of planetary mass ratios considered to two choices: strictly equal masses (3E), or a hierarchical Solar System analogue (4H). Although we have shown that this simplification can reproduce the observed eccentricity distribution of the giant exoplanets, in reality mass ratios will fall on a continuum; this greatly increases the parameter space to investigate. Here, we simply note the following: With our dichotomous distribution of mass ratios, for a given eccentricity the distribution of $f_{\rm rhab}$ is bimodal (Fig. 8), having a high-survivability peak from the 4H systems and a low-survivability peak from the 3E systems. We would then expect, for example, a 2:1:1 mass ratio to be intermediate between the 4H and the 3E in destructibility, and with a continuum of mass ratios, we expect the $f_{\rm rhab}$ distribution to be less bimodal.

Finally, the number of planets in our simulations was fixed at either three or four. Adding more planets will likely be more destructive to bodies in the HZ if the planets are comparable in mass to the largest planet, since there will be more possibilities of scattering a large planet on to an orbit with a small pericentre, and also more secular resonances to destabilize the HZ at a distance. However, if the additional planets are smaller (neptune-mass), there should be a weaker effect, as we have shown that the dominant mechanism for destabilizing the HZ is not the entry of neptune-mass planet into it (Section 6.1).

7 FUTURE OBSERVATIONS

Finally, we can make some comments as to which of the systems we have studied provide the best prospects for the detection of planets in the HZ, based on their resilient habitability. All the low-eccentricity systems in Group 1 make good candidates for observations as they all have high median $f_{\rm rhab}$ values. Particularly good are the ones where the lower end of the orange interval in Fig. 7 is high: HD 95872, HD 154345, and HD 102843. These are highlighted in Fig. 14, where we show the resilient habitability for all of the systems we have studied as a function of the giant planet's eccentricity and distance to the HZ. This figure should be compared to fig. 12 of Carrera et al. (2016), which shows the median resilient habitability for a generic system. The broad features are the same – high resilient habitability for low eccentricity and wide orbit planets – but we wish to emphasize two points: the large range in resilient habitability arising from different runs in the same system; and the fact that different systems close to each other in parameter space on this figure can have different values of resilient habitability, in part because we have included the mass of the known planet as a third parameter.

We also highlight in Fig. 14 some other systems that offer good prospects for follow up. HD 6718 and HD 150706 have large uncertainties on their eccentricities, and if the true eccentricities are at the lower end of the allowed ranges then their resilient habitability is high (see Fig. 9). HD 25015 and GJ 328 are of high eccentricity ($e \sim 0.4$) but distant from the HZ. They show strongly bimodal distributions of $f_{\rm rhab}$: if their past history involved ejection of an equal-mass planet then $f_{\rm rhab} \approx 0$, but if they have ejected a lower mass planet then their resilient habitability is high. The $f_{\rm rhab}$ distributions of these seven systems of interest are shown in Fig. 15.

In the introduction we made a point about utilizing *Gaia* to constrain the orbital plane of the giant planets and using that to identify edge-on systems that will also show a strong RV signal from any potential Earth-like planet. The systems we have studied, typically at distances of a few 10 s of pc, will have a good

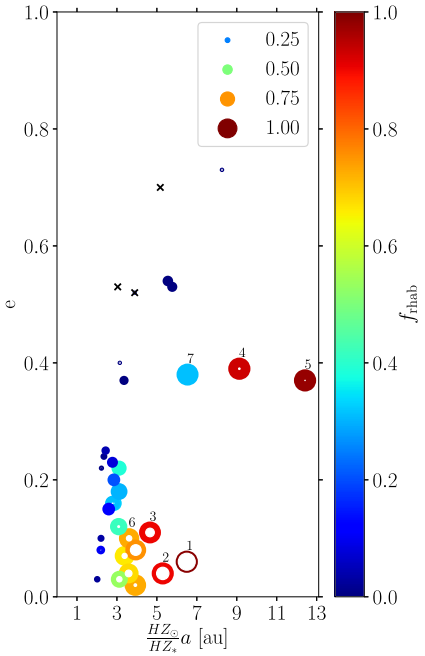

Figure 14. The figure shows the resilient habitability, and its uncertainty, of all the simulated systems. The systems are marked with their planets' semimajor axes rescaled so that the mid-point of the systems' HZ corresponds to the mid-point of the HZ in the Solar System, and with their reported eccentricities. The colour of each symbol is set by the median of $f_{\rm rhab}$ distribution. The inner and outer radii of annular symbols scale linearly with the $\pm 1\sigma$ values of $f_{\rm rhab}$ distribution. The crosses indicate systems where the 1σ upper limit is less than 0.05. Thus, the blue crosses are very bad, small blue dots are bad, the narrow brown/red annuli are good, and the wide annuli give a range of possible outcomes. We have highlighted the best potential systems for follow-up observations; they are as follows: (1) HD 95872 (2) HD 154345 (3) HD 102843 (4) HD 25015 (5) GJ 328 (6) HD 6718 (7) HD 150706.

enough signal-to-noise to detect the astrometric reflex motion of the star from the known Jovian planets (Ranalli et al. 2018, fig. 2). Furthermore, the orbital inclination of the giant planet in these systems will be constrained to $\sigma_{\cos I} \sim 0.1$ (Ranalli et al. 2018, fig. 9 and table 5).

Finally, we consider how the orbit of the stars through the Galaxy may affect the habitability of the systems. Kokaia & Davies (2019) showed how the passage of a star and its planetary system through giant molecular clouds – which may trigger mass extinctions – depends on the star's orbit in the Galaxy. We obtain the positions and velocities of the seven highlighted systems from *Gaia* DR2 (Gaia Collaboration 2018) and integrate them to determine their Galactic orbits (see Kokaia & Davies 2019 for details). We find that for all of the systems, their orbits in the Galaxy lead to excursions of more than 100 pc from the Galactic plane. Comparing to Kokaia & Davies (2019) we find that all of them have encounters with giant molecular clouds at a similar rate to the Sun: between once every 500 Myr and 3 Gyr.

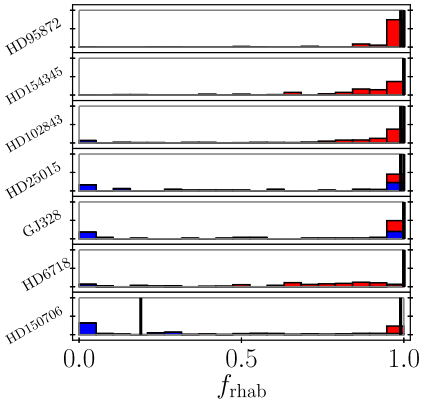

Figure 15. The binned, resampled data used to produce the $f_{\rm rhab}$ distributions in Fig. 7. The histograms are normalized such that for each system the blue and the red bins together add up to one. The blue bins show the number of 3E runs and the red bins show the 4H runs. The black lines show the bounds of the $f_{\rm hab,\,1P}$ values.

8 SUMMARY

We have selected 34 systems containing a single massive planet orbiting an FGK-dwarf beyond the HZ. We simulated the dynamical history of these systems considering initial multiple-planet systems comprising either three equal-mass planets (3E) or four planets having a mass hierarchy of the four gas giants of our Solar System (4H). These systems pass through a phase of instability where planets are ejected via planet–planet scattering leaving other planets on more bound and more eccentric orbits. One can probe the entire observed eccentricity range with 3E and 4H systems. Low-eccentricity planets are produced mostly by 4H systems, whereas all systems containing a planet with an eccentricity, $e > 0.5$ are derived exclusively from 3E systems.

We select the subset of the runs which give eccentricities of the inner planet matching observations. Our simulations include test particles in the HZ to represent terrestrial planets. We measure the fraction of test particles located within the HZ which survive the dynamical evolution, and term this fraction the resilient habitability, $f_{\rm rhab}$. We also compute the fraction of test particles within the HZ which would be removed from the HZ by the single planet as observed today, and refer to this as the present-day habitability, $f_{\rm hab,\,1P}$.

For the 3E runs, the resulting instability tends to be much more violent resulting in higher eccentricities and planets often entering the HZ and clearing it out. For 4H, on the other hand, the two most massive planets rarely enter the HZ with the most massive one only doing so in systems where the observed planet is very close to the HZ boundary. This leaves the HZ mostly intact as the lower mass planets cannot directly eject the test particles. The systems, shown in Fig. 3, are placed into one of three groups:

Group 1: Systems where the planet has a much larger semimajor axis than the outer edge of the HZ and/or has a low eccentricity. These systems all have high values of $f_{\rm hab,\,1P}$ and the median values of the $f_{\rm rhab}$ distribution also tend to be high. However, some of the systems in the group have distributions of $f_{\rm rhab}$ that go down to much lower values as can be seen in Fig. 7. In all cases, $f_{\rm rhab}$ tends to be lower than $f_{\rm hab,\,1P}$. In other words, *history matters*: the dynamical past is more damaging than present perturbations of the observed planet.

Group 2: Systems where the planet has a slightly larger semimajor axis than the outer edge of the HZ and/or has a high eccentricity which brings it very close to the HZ. These planets are much more damaging to objects within the HZ. Systems in Group 2 generally show much lower values of $f_{\rm hab,\,1P}$ than seen in Group 1. Values of $f_{\rm rhab}$ are even lower owing to the extra damaging effects of the earlier phase of planet–planet scattering.

Group 3: Systems that could fit in either Group 1 or Group 2, due to the planets having large uncertainties in their eccentricities which leads to a large range of possible $f_{\rm hab,\,1P}$ and $f_{\rm rhab}$ values. For these systems we recalculate the $f_{\rm rhab}$ distribution by considering three narrower ranges of eccentricities centred around the mean and $+/-1\sigma$ values of the observed eccentricities as shown in Fig. 9. We see two systems that show very large differences between the distribution of $f_{\rm rhab}$ if the eccentricity is high, and that if it is low; these are HD 6718 and HD 150706, and therefore better determination of these eccentricities is needed.

Even in the 4H runs where the most-massive planet does not enter the HZ, the planet can do significant damage to the HZ when its semimajor axis changes during the scattering phase, as then MMRs can sweep over the HZ and pump up the eccentricity of the test particles until they have a close encounter with the gas giant and get ejected or until the test particle hits the star. This is consistent with models for the depletion of the asteroid belt in the Solar System (Izidoro et al. 2016; Clement, Raymond & Kaib 2019).

In contrast to the MMRs, the secular resonances very rarely do any damage to the HZ. This is because for most systems, having the secular resonances inside the HZ requires the two planets to be 4–7 mutual hill radii apart. Whilst this is a stable configuration for circular coplanar orbits, it is rarely stable after an instability. The planets can in principle end up at the right semimajor axes but they will have eccentric orbits which generally leads to either one of them eventually getting ejected or a reconfiguration such that the secular resonances move away from the HZ.

We provide a list of systems containing at least one known giant planet most likely to be able to host an Earth-like planet: HD 95872, HD 154345, HD 102843, HD 25015, GJ 328, HD 6718, and HD 150706. HD 95872 is the clearly best candidate as can be seen in Fig. 14.

ACKNOWLEDGEMENTS

The authors are supported by the project grant 2014.0017 'IMPACT' from the Knut and Alice Wallenberg Foundation. The simulations were performed on resources provided by the Swedish National Infrastructure for Computing (SNIC) at Lunarc, which we can contribute thanks to grants from The Royal Physiographic Society of Lund. We thank Ross P. Church for comments on the manuscript. We also thank the referee for their feedback which helped improve the paper.

REFERENCES

Abramov O., Mojzsis S. J., 2009, Nature, 459, 419
Agnew M. T., Maddison S. T., Horner J., 2018, MNRAS, 477, 3646
Agnew M. T., Maddison S. T., Thilliez E., Horner J., 2017, MNRAS, 471, 4494
Anglada-Escudé G., López-Morales M., Chambers J. E., 2010, ApJ, 709, 168
Antoniadou K. I., Voyatzis G., 2016, MNRAS, 461, 3822
Bashi D., Helled R., Zucker S., Mordasini C., 2017, A&A, 604, A83
Batygin K., Laughlin G., 2008, ApJ, 683, 1207
Batygin K., Laughlin G., 2015, Proc. Natl. Acad. Sci., 112, 4214
Benedict G. F. et al., 2006, AJ, 132, 2206
Bitsch B., Crida A., Libert A. S., Lega E., 2013, A&A, 555, A124
Bitsch B., Izidoro A., Johansen A., Raymond S. N., Morbidelli A., Lambrechts M., Jacobson S. A., 2019, A&A, 623, A88
Boisse I. et al., 2012, A&A, 545, A55
Bolmont E., Libert A.-S., Leconte J., Selsis F., 2016, A&A, 591, A106
Bryan M. L., Knutson H. A., Lee E. J., Fulton B. J., Batygin K., Ngo H., Meshkat T., 2019, AJ, 157, 52
Buchhave L. A., Bitsch B., Johansen A., Latham D. W., Bizzarro M., Bieryla A., Kipping D. M., 2018, ApJ, 856, 37
Burke C. J. et al., 2015, ApJ, 809, 8
Carrera D., Davies M. B., Johansen A., 2016, MNRAS, 463, 3226
Carter-Bond J. C., O'Brien D. P., Raymond S. N., 2014, in Haghighipour N., ed., Proc. IAU Symp. 293, Formation, Detection, and Characterization of Extrasolar Habitable Planets. Cambridge University Press, Cambridge, UK, p. 229
Chambers J. E., 1999, MNRAS, 304, 793
Chambers J. E., 2001, Icarus, 152, 205
Chambers J. E., Wetherill G. W., Boss A. P., 1996, Icarus, 119, 261
Childs A. C., Quintana E., Barclay T., Steffen J. H., 2019, MNRAS, 485, 541
Chyba C. F., 1990, Nature, 343, 129
Clement M. S., Raymond S. N., Kaib N. A., 2019, AJ, 157, 38
Davies M. B., Adams F. C., Armitage P., Chambers J., Ford E., Morbidelli A., Raymond S. N., Veras D., 2014, in Beuther H., Klessen R. S., Dullemond C. P., Henning T., eds, Protostars and Planets VI. University of Arizona Press, Tucson, AZ, p. 787
Denham P., Naoz S., Hoang B.-M., Stephan A. P., Farr W. M., 2019, MNRAS, 482, 4146
Dressing C. D., Spiegel D. S., Scharf C. A., Menou K., Raymond S. N., 2010, ApJ, 721, 1295
Endl M. et al., 2016, ApJ, 818, 34
Feng F. et al., 2019, ApJS, 242, 25
Ford E. B., Rasio F. A., 2008, ApJ, 686, 621
Gaia Collaboration 2018, A&A, 616, A1
Georgakarakos N., Eggl S., Dobbs-Dixon I., 2018, ApJ, 856, 155
Gilmozzi R., Spyromilio J., 2007, Messenger, 127, 11
Giuppone C. A., Morais M. H. M., Correia A. C. M., 2013, MNRAS, 436, 3547
Gladman B., 1993, Icarus, 106, 247
Grazier K. R., 2016, Astrobiology, 16, 23
Hadden S., Lithwick Y., 2018, AJ, 156, 95
Halliday A. N., 2008, Phil. Trans. R. Soc. A, 366, 4163
Hansen B. M. S., 2009, ApJ, 703, 1131
Hansen B. M. S., 2017, MNRAS, 467, 1531
Hara N. C., Boué G., Laskar J., Delisle J. B., Unger N., 2019, MNRAS, 489, 738
Horner J., Jones B. W., 2008, Int. J. Astrobiol., 7, 251
Horner J., Jones B. W., 2009, Int. J. Astrobiol., 8, 75
Horner J., Jones B. W., Chambers J., 2010, Int. J. Astrobiol., 9, 1
Hsu D. C., Ford E. B., Ragozzine D., Ashby K., 2019, AJ, 158, 109
Innanen K. A., Zheng J. Q., Mikkola S., Valtonen M. J., 1997, AJ, 113, 1915
Izidoro A., Raymond S. N., Pierens A., Morbidelli A., Winter O. C., Nesvorny' D., 2016, ApJ, 833, 40
Jacobsen S. B., 2005, Annu. Rev. Earth Planet. Sci., 33, 531
Jenkins J. S. et al., 2017, MNRAS, 466, 443

Johansen A., Davies M. B., Church R. P., Holmelin V., 2012, ApJ, 758, 39
Jones B. W., Sleep P. N., Chambers J. E., 2001, A&A, 366, 254
Jurić M., Tremaine S., 2008, ApJ, 686, 603
Kaib N. A., Raymond S. N., Duncan M. J., 2011, ApJ, 742, L24
Kane S. R., Torres S. M., 2017, AJ, 154, 204
Kokaia G., Davies M. B., 2019, MNRAS, 945, 5165
Kopparapu R. K., Ramirez R. M., SchottelKotte J., Kasting J. F., Domagal-Goldman S., Eymet V., 2014, ApJ, 787, L29
Kürster M., Trifonov T., Reffert S., Kostogryz N. M., Rodler F., 2015, A&A, 577, A103
Laakso T., Rantala J., Kaasalainen M., 2006, A&A, 456, 373
Lambrechts M., Morbidelli A., Jacobson S. A., Johansen A., Bitsch B., Izidoro A., Raymond S. N., 2019, A&A, 627, A83
Laskar J., Gastineau M., 2009, Nature, 459, 817
Leite A. C. O., Martins C. J. A. P., Molaro P., Monai S., Alves C. S., Silva T. A., the ESPRESSO Science Team, 2018, preprint (arXiv:1812.06796)
Linsenmeier M., Pascale S., Lucarini V., 2015, Planet. Space Sci., 105, 43
Lissauer J. J. et al., 2011, ApJS, 197, 8
Lucy L. B., Sweeney M. A., 1971, AJ, 76, 544
Machida M. N., Kokubo E., Inutsuka S.-I., Matsumoto T., 2010, MNRAS, 405, 1227
Malmberg D., Davies M. B., Heggie D. C., 2011, MNRAS, 411, 859
Mardling R. A., Aarseth S. J., 2001, MNRAS, 321, 398
Marmier M. et al., 2013, A&A, 551, A90
Matsumura S., Ida S., Nagasawa M., 2013, ApJ, 767, 129
Menou K., Tabachnik S., 2003, ApJ, 583, 473
Ment K., Fischer D. A., Bakos G., Howard A. W., Isaacson H., 2018, AJ, 156, 213
Morbidelli A., Chambers J., Lunine J. I., Petit J. M., Robert F., Valsecchi G. B., Cyr K. E., 2000, Meteor. Planet. Sci., 35, 1309
Mordasini C., Alibert Y., Benz W., 2009, A&A, 501, 1139
Moutou C. et al., 2011, A&A, 527, A63
Mullally F. et al., 2015, ApJS, 217, 31
Murray C. D., Dermott S. F., 1999, Solar System Dynamics. Cambridge University Press, Cambridge, UK.
Mustill A. J., Davies M. B., Johansen A., 2017, MNRAS, 468, 3000
Mustill A. J., Davies M. B., Johansen A., 2018, MNRAS, 478, 2896
Mustill A. J., Wyatt M. C., 2012, MNRAS, 419, 3074
O'Brien D. P., Izidoro A., Jacobson S. A., Raymond S. N., Rubie D. C., 2018, Space Sci. Rev., 214, 47
O'Brien D. P., Morbidelli A., Levison H. F., 2006, Icarus, 184, 39
Pepe F. A. et al., 2010, in McLean I. S., Ramsay S. K., Takami H., eds, Proc. SPIE Conf. Ser. Vol. 7735, Ground-based and Airborne Instrumentation for Astronomy III. SPIE, Bellingham, p. 77350F
Perryman M., Hartman J., Bakos G. Á., Lindegren L., 2014, ApJ, 797, 14
Petrovich C., 2015, ApJ, 808, 120
Piso A.-M. A., Youdin A. N., 2014, ApJ, 786, 21
Piso A.-M. A., Youdin A. N., Murray-Clay R. A., 2015, ApJ, 800, 82
Ragusa E., Rosotti G., Teyssandier J., Booth R., Clarke C. J., Lodato G., 2018, MNRAS, 474, 4460
Ranalli P., Hobbs D., Lindegren L., 2018, A&A, 614, A30
Rauer H. et al., 2014, Exp. Astron., 38, 249
Raymond S. N., Izidoro A., 2017, Icarus, 297, 134
Raymond S. N., Mandell A. M., Sigurdsson S., 2006, Science, 313, 1413
Raymond S. N., O'Brien D. P., Morbidelli A., Kaib N. A., 2009, Icarus, 203, 644
Rey J. et al., 2017, A&A, 601, A9
Rickman E. L. et al., 2019, AAP, 625, A71
Robertson P., Endl M., Cochran W. D., MacQueen P. J., Boss A. P., 2013, ApJ, 774, 147
Rowan D. et al., 2016, ApJ, 817, 104
Shen Y., Turner E. L., 2008, ApJ, 685, 553
Shikita B., Koyama H., Yamada S., 2010, ApJ, 712, 819
Skidmore W., TMT International Science Development Teams, Science Advisory Committee T., 2015, Res. Astron. Astrophys., 15, 1945
Sozzetti A., Casertano S., Lattanzi M. G., Spagna A., Morbidelli R., Pannunzio R., Pourbaix D., Queloz D., 2008, in Jin W. J., Platais I., Perryman M. A. C., eds, Proc. IAU Symp. 248, A Giant Step: from Milli- to Micro-arcsecond Astrometry. Cambridge University Press, Cambridge, UK, p. 256
Spiegel D. S., Raymond S. N., Dressing C. D., Scharf C. A., Mitchell J. L., 2010, ApJ, 721, 1308
Stassun K. G., Collins K. A., Gaudi B. S., 2017, AJ, 153, 136
Thommes E. W., Matsumura S., Rasio F. A., 2008, Science, 321, 814
Veras D., Armitage P. J., 2005, ApJ, 620, L111
Ward P. D., Brownlee D., Krauss L., 2000, Phys. Today, 53, 62
Wittenmyer R. A., Bergmann C., Horner J., Clark J., Kane S. R., 2019, MNRAS, 484, 4230
Wittenmyer R. A. et al., 2014, ApJ, 783, 103
Zakamska N. L., Pan M., Ford E. B., 2011, MNRAS, 410, 1895
Zeebe R. E., 2015, ApJ, 798, 8
Zhu W., Wu Y., 2018, AJ, 156, 92

This paper has been typeset from a TEX/LATEX file prepared by the author.

Paper III

Paper III:
Effects of capturing a wide-orbit planet on planetary systems: system stability and Habitable Zone bombardment rates

G. Kokaia, M.B. Davies, A.J. Mustill (2021)
Monthly Notices of the Royal Astronomical Society (Submitted)

My contribution:

The origin of this paper is an amalgamation of other work. It is in part the first work GK did dubbed 3P+X where he tried to constrain external perturbers on three-planet systems. It is also a follow-up on work done by MBD and AM. It also follows on from work that Alex has done with other students. For this paper, GK performed all of the simulations after Melvyn pointed him to the necessary literature and AM provided guidance in how to best use the computer code Mercury for our purposes. The work then proceeded in the same manner as before with regular discussions between all of them guiding GK forward in how to proceed. GK wrote the paper more independently in this case with final editing input from both MBD and AM.

MNRAS 000, 1–?? (2020) Preprint 2 November 2020 Compiled using MNRAS LATEX style file v3.0

Effects of capturing a wide-orbit planet on planetary systems: system stability and Habitable Zone bombardment rates

Giorgi Kokaia[1]⋆, Melvyn B. Davies[1], Alexander J. Mustill[1]
[1]Lund Observatory, Department of Astronomy and Theoretical Physics, Lund University, Box 43, SE-221 00 Lund, Sweden

2 November 2020

ABSTRACT
A large fraction of stars are formed in dense clusters. In the cluster, close encounters between stars at distances less than 100 au are common. It has been shown that during close encounters planets can transfer between stars. Such captured planets will be on different orbits compared to planets formed in the system, often on very wide, eccentric and inclined orbits. We examine how these captured planets affect Kuiper-belt like asteroid belts in their new systems, and how this affects habitable planets in the system. We show that these captured planets can destabilize the asteroid belt, and we show that the fraction of the asteroid that make it past the giant planets into the system to impact the habitable planet is independent of the captured planets orbital plane, whereas the fraction of the asteroids that are removed and the rate at which they are removed depend strongly on the captured planets pericentre and inclination. We then examine all possible outcomes of planet capture and find that when a Jupiter-mass planet is captured it will in 40% of cases destabilize the planets in the system, in 40% of cases deplete the asteroid belt in a few Myr, i.e. not posing much risk to life on terrestrial planets which would be expected to develop later. In the final 20% of cases the result will be a flux of impactors 5-10 times greater than that on Earth that can persist for several Gyr, quite detrimental to the development of life on the planet.

Key words: planets and satellites: dynamical evolution and stability; planets and satellites: general; celestial mechanics; planetary systems; open clusters and associations: general; Astrophysics - Earth and Planetary Astrophysics

1 INTRODUCTION

The majority of stars form in clusters (Lada & Lada 2003). These clusters have stellar densities of 100–1000 per pc^{-3} (Dias et al. 2002; Lamers et al. 2005), compared to ~ 1 per pc^{-3} in the field (see e.g. Gaia Collaboration et al. 2018), and lifetimes of several tens to hundreds of Myr (Gieles et al. 2007). In such dense clusters 10–20% of Solar-like stars will experience an encounter within 100 au with another star, which is close enough to affect the stability of existing planets (Malmberg et al. 2011).

Given that the giant planets form before gas dispersal in proto-planetary discs, typically within a few Myr after star formation (Machida et al. 2010; Piso & Youdin 2014; Piso et al. 2015; Bitsch et al. 2019), for most of these encounters the stars will have finished forming their giant planets. During these encounters, planets can be transfered between stars (Li et al. 2019). This can result in planets on orbits that are inconsistent with planet formation models. This is a possible explanation for the hypothesised presence of Planet 9 (Batygin & Brown 2016) on its (albeit loosely constrained Brown & Batygin 2016) few hundred au wide orbit (Mustill et al. 2016).

In this paper we will examine how capturing a planet will affect planets in the habitable zone. In particular we consider systems like our own, i.e. a terrestrial planet at ∼1 au, with giant planets beyond it surrounded by a Kuiper-belt like asteroid belt (throughout the paper we refer to this belt simply as the "asteroid belt" and its component bodies as "asteroids"). There are four ways in which the captured planet can affect them:

(i) It can be captured on an orbit that crosses the orbits of planets in the system, meaning it can either directly scatter a planet in the habitable zone or trigger an instability amongst the outer planets. Instabilities amongst the outer planets can destabilize a large fraction of possible orbits in the habitable zone (Carrera et al. 2016; Kokaia et al. 2020).

(ii) The captured planet can induce Kozai oscillations,

⋆ Contact e-mail: giorgi@astro.lu.se

which can destabilize all of the planets without the captured planet ever directly interacting with them. The stability of planetary systems with an external highly inclined companion has been well studied for both stellar and planetary companions by e.g Innanen et al. (1997); Kaib et al. (2011); Malmberg et al. (2011); Mustill et al. (2017); Denham et al. (2019).

(iii) In the absence of an instability the outer planets or a single outer planet can have its eccentricity pumped up putting it on an orbit crossing the habitable zone which will destabilize most if not all possible orbits within it (Jones et al. 2001; Menou & Tabachnik 2003; Matsumura et al. 2013; Agnew et al. 2018; Georgakarakos et al. 2018).

(iv) Asteroids in belts external to the planets such as the ones found in the Kuiper belt (which appears to be fairly common around Sun-like stars Montesinos et al. 2016; Sibthorpe et al. 2018) can be directly scattered or undergo Kozai-oscillations and end up crossing the orbits of the giant planets in the system. They can then be scattered further inwards and end up on orbits crossing the habitable zone. This can then lead to a large number of asteroid-impacts on any planets in the habitable zone.

The main focus of the paper will be outcome iv), with outcome i) discussed briefly. In section 2 we will discuss the theoretical framework of the Kozai mechanism and also show the results of an exploratory experiment comparing the theory with our simulation setup. This setup will be discussed in section 3 and the findings from it will be presented in section 4. In section 5 we discuss the implications of said findings and also explore the impact of having different setups.

2 THE KOZAI MECHANISM

The Kozai mechanism (Kozai 1962; Lidov 1962) is a secular three-body effect which can produce very large oscillations in eccentricity and inclination. Here follows a brief description of the process: Consider an inner body (A) and an outer companion (C) orbiting a central body ($\star$). A particularly simple case of Kozai cycles occurs when the three conditions below are met (Innanen et al. 1997; Malmberg et al. 2007a).

- $a_C \gg a_A$: The semi-major axis of C needs to be much larger than the semi-major axis of A.
- $m_C \gg m_A$: The mass of C needs to be much larger than the mass of A.
- $180^\circ - i_{\rm crit} > i > i_{\rm crit}$: The mutual inclination (i) between A and C need be between the the critical angle $i_{\rm crit}$ and $180^\circ - i_{\rm crit}$ where $i_{\rm crit} = \arcsin\sqrt{2/5} \approx 39.23^\circ$.

Cycles in eccentricity and inclination will still happen if either of the first two conditions are not met. However, the formalism that follows will be less and less accurate as the mass and semi-major axis ratios approach unity (Katz et al. 2011; Naoz et al. 2013b,a; Antognini 2015).

The set of differential equations (as given in Valtonen & Karttunen 2006, which is taken from Innanen et al. 1997 but correcting a sign error in the differential equation describing the inclination) describing the evolution of the Keplerian orbital elements [i: inclination, e: eccentricity, ω: argument of pericentre, Ω: longitude of ascending node] of the body undergoing the oscillations is shown below:

$$\begin{aligned}
\frac{di}{d\tau} &= -\frac{15}{8}\frac{e^2}{\sqrt{1-e^2}}\sin 2\omega \sin i \cos i, \\
\frac{de}{d\tau} &= \frac{15}{8} e\sqrt{1-e^2}\sin 2\omega \sin^2 i, \\
\frac{d\omega}{d\tau} &= \frac{3}{4}\frac{1}{\sqrt{1-e^2}}\left[2(1-e^2) + 5\sin^2\omega(e^2 - \sin^2 i)\right], \\
\frac{d\Omega}{d\tau} &= -\frac{\cos i}{4\sqrt{1-e^2}}(3 + 12e^2 - 15e^2\cos^2\omega).
\end{aligned} \tag{1}$$

with l,

$$l = \sqrt{1-e^2}\cos i, \tag{2}$$

as a conserved quantity, which is a measure of how much angular momentum can be redistributed in the system. Here i is the mutual inclination between A and C, τ is a re-scaling of the time, which for C with semi-minor axis $b_{\rm C}$ is given as:

$$\tau = \frac{a_{\rm A}^{1.5}}{b_{\rm C}^2}\frac{m_{\rm A}}{\sqrt{GM_\star}}t, \tag{3}$$

where G is the gravitational constant and $M_\star$ the stellar mass. From this we can determine the Kozai time-scale as a function of the period of A ($P_{\rm A}$) as:

$$T_{\rm Kozai} \sim P_{\rm A}\left(\frac{a_{\rm C}}{a_{\rm A}}\right)^3\left(\frac{M_\star}{m_C}\right)(1-e_{\rm C}^2)^{3/2} \tag{4}$$

We integrate the equations and show the evolution of eccentricity and inclination in figure 1, where we see the oscillations as a function of the time parameter τ. Given the conserved quantity, l, we see that as expected A reaches its maximum eccentricity when it is at its minimum inclination. We can determine the maximum eccentricity by setting $\cos i_A = \cos i_{\rm crit}$ in equation 2.

$$e_{\rm max} = \sqrt{1 - (5/3)(1-e_0^2)\cos^2 i_0} \tag{5}$$

where e_0 and i_0 are the initial values for the eccentricity of the inner body and mutual inclination between inner and outer body.

2.1 Kozai between planets

The Kozai mechanism described in the previous section details how the system behaves in the test particle limit, i.e. when all the angular momentum is held by the inclined perturber.

The system which has been explored in greatest detail throughout this paper is set up as follows: a central body of one Solar mass, an Earth–mass planet at 1 au, a Jupiter–mass planet on a circular orbit at 10 au and an additional Jupiter–mass planet on a circular but inclined orbit at 100 au. We refer to each body as Sun, Earth, [lower case] jupiter and Companion.

We investigate how the behaviour of this system differs from what we expect from the analytical solution above by running a set of simulations for just these four bodies (SEjC) where we vary the inclination of the Companion (i_C) from 0

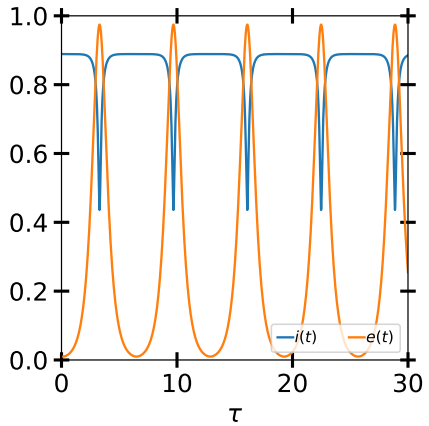

Figure 1. The eccentricity and inclination evolution as given by equation 1 with initial values of $e_0 = 0.01$ and $i_0 = 80°$. The inclination has been re-normalized such that $90° = 1$, the maximum eccentricity reached is $e = 0.97$ and is given by equation 5.

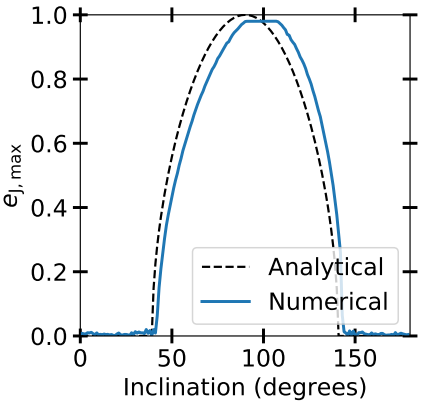

Figure 2. A range of simulations for the SEjC system. The dashed black line shows the theoretical $e_{\max}$ predicted from equation 5, i.e. the test particle limit. The solid blue line shows the maximum eccentricity achieved by the jupiter in the SEjC runs.

to 180[1] degrees, with both the Earth and jupiter in the reference plane. In figure 2 we show the maximum eccentricity reached by jupiter as a function of eccentricity. The black dashed line shows the theoretical expectation, which is symmetric about 90 degrees as expected; given equation 5. The solid blue line which shows the simulated data is no longer symmetric due to the angular momentum of jupiter and the location of the maximum has now shifted from 90 to ∼100 degrees. The flat peak of the blue line is due to the Sun having a radius of 0.2 au in the simulations, i.e. when anything gets within said distance it is removed. This was chosen for computational efficiency in the runs with asteroids later one, but we chose to keep it as such here for consistency.

This means that jupiter reaches an eccentricity of 0.98 for i_C between 90 and 110 degrees, rather than between 81 and 99 degrees indicating an asymmetry between pro and retro-grade orbits. This makes sense because jupiter holds ∼1/3 of the system's angular momentum and thus putting the Companion on a retrograde orbit will not invert the total angular momentum-vector of the system.

2.2 Time-scales

As we will see later, time-scales will prove to be an important aspect of what happens when a planet is captured. This is because a planet on an orbit that is precessing sufficiently fast will not have its eccentricity pumped up by the Kozai mechanism (Kaib et al. 2011; Mustill et al. 2017; Denham et al. 2019). Orbits precess in any non-Keplerian potential (see e.g. Murray & Dermott 1999), i.e. any two bodies orbiting a central more massive body will precess.

This means that if there are multiple planets in the system their orbits can be such that they will not undergo Kozai cycles. For precession to prevent Kozai cycles it needs to happen on shorter time-scales than the Kozai time-scale. The precession time-scale on an orbit exterior to the orbit of $N_{\rm inner}$ number of planets is given by (Mustill et al. 2017):

$$T_{\rm prec} \sim \frac{4}{3} P_{\rm outer} \left(\sum_{i=1}^{N_{\rm inner}} \frac{m_i a_i^2}{M_\star a_{\rm outer}^2} \right)^{-1} . \quad (6)$$

In the setup we are looking at we then find four time-scales: $T_{\rm P,p}$ – the precession time-scale in the planet–planet interaction; $T_{\rm K,a}$, $T_{\rm K,p}$ – the Kozai time-scales of the asteroid belt and planets given by equation 4; and $T_{\rm P,a}$ – the precession time-scale of the planets acting on the asteroid belt. In order to avoid system-wide instability, while allowing for delivery of asteroids to the HZ, these need to satisfy $T_{\rm P,p} < T_{\rm K,p} < T_{\rm K,a} < T_{\rm P,a}$. Given the scaling with semi-major axis in eqs. 4 and 6 we can ignore $T_{\rm K,p}$ as it will always be smaller than $T_{\rm K,a}$ if that is smaller than $T_{\rm P,a}$. That leaves us with the time-scale condition:

$$T_{\rm P,p} < T_{\rm K,a} < T_{\rm P,a} \quad (7)$$

However it should be noted that, for most planetary systems containing more than one planet the first inequality will be satisfied if the second one is.

3 SETUP OF THE MAIN EXPERIMENTS

All the simulations were performed using the MERCURY N-body package (Chambers 1999). We used the Bulirsch-Stoer

[1] Inclinations for the Companion above 90 degrees denote retrograde orbits.

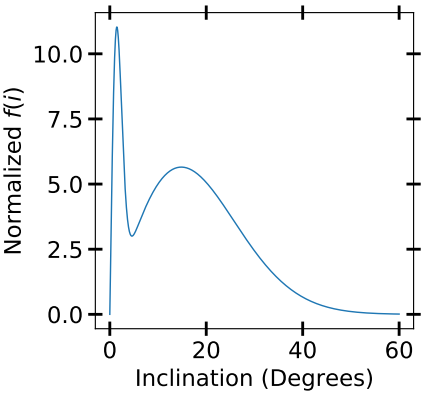

Figure 3. The two-component inclination distribution of the Kuiper-belt, as determined in Volk & Malhotra (2011).

integrator with an accuracy parameter of 10^{-12} resulting in energy errors of $< 10^{-6}$. We set an ejection radius of 1000 au and set a stellar radius of 0.2 au. Both are done to speed up the simulations (reducing the number of bodies simulated and avoiding small pericentre passages). The stellar radius is also motivated physically as the asteroids (test particles) simulated are icy bodies and would likely not survive such a pericentre passage.

In all the simulations containing an Earth we inflated it to 100 Earth radii in order to have some asteroids hitting the body without having to use an unfeasible number of test particles. Throughout the paper we will use a dagger (†) to differentiate hitting the inflated Earth from hitting an actual Earth-sized Earth.

3.1 Asteroid belt

To the SEjC system we now add asteroids and examine how they interact with the Companion and with jupiter. For this we use an asteroid-belt analogous to the Kuiper-belt using the prescription from Volk & Malhotra (2011).

In the prescription the asteroids have a uniform semi-major axis distribution between 40 and 50 au. The eccentricity distribution is a Gaussian with $\mu = 0.15$ and $\sigma = 0.07$ truncated at 0 and 0.3, putting their orbits between 28 and 65 au. The inclination of the asteroids is modelled with a hot and a cold component, the distribution is given below:

$$f(i) = \sin i \left[A \exp\left(\frac{-i^2}{2\sigma_1^2}\right) + (1-A) \exp\left(\frac{-i^2}{2\sigma_2}\right) \right], \tag{8}$$

where $A = 0.95$, $\sigma_1 = 1.4°$ and $\sigma_2 = 15.3°$. This distribution is shown in figure 3.

There is no preferred plane for the Companion to be captured on (Li et al. 2019), which means that its expected inclination follows an isotropic probability distribution. Given the inclination distribution of the asteroids, for every Companion orbit there will be a subset of asteroids that have mutual inclinations greater than $i_{\rm crit}$ that can undergo Kozai oscillations. A subset of these will reach maximum eccentricities such that their pericenters are interior to the orbit of jupiter. We can compute what fraction of asteroids reach this eccentricity by considering:

$$e_{\rm max} \geqslant e_{\rm lim}, \tag{9}$$

where $e_{\rm lim}$ for each asteroid (a) is given by:

$$(1 - e_{\rm lim}) a_{\rm a} \leqslant a_{\rm j}, \tag{10}$$

in which $a_{\rm j}$ is the semi-major axis of jupiter. Equation 5 gives $e_{\rm max}$ for each asteroid with initial eccentricity $e_{0,a}$ and initial mutual inclination with respect to Companion $i_{0,a}$ as:

$$\left(1 - \sqrt{1 - (5/3)(1 - e_{0,a}^2)\cos^2 i_{0,a}}\right) a_a \leqslant a_{\rm j}, \tag{11}$$

i is given by:

$$\cos i = \underline{\hat{J}}_a \cdot \underline{\hat{J}}_C, \tag{12}$$

where $\underline{\hat{J}}_a$ and $\underline{\hat{J}}_C$ are the angular momentum unit vectors of each body. The angular momentum vector, in terms of the Keplerian angles; longitude of ascending node, Ω, and inclination, i, is given as:

$$\underline{\hat{J}} = \begin{bmatrix} \sin\Omega \sin i \\ -\cos\Omega \sin i \\ \cos i \end{bmatrix}. \tag{13}$$

With these limits in place we can integrate over the initial values of $a_{\rm a}$, $e_{\rm a}$, $\Omega_{\rm a}$ and $i_{\rm a}$ and determine the fraction of asteroids that get put on these kinds of orbits as a function of the inclination of the captured planet with respect to the reference plane.

We show this fraction (blue line) for $a_j = 10$ au in figure 4 along with the fraction of asteroids that can undergo Kozai cycles (black dashed line) for any given Companion inclination.

3.2 SEjC

We now go back to the SEjC system and simulate it with asteroids. The planetary system contains a one Solar mass star, the Earth, jupiter and a Companion. We set $a_{\rm j}$=10 au, a_C=100 au, e_C=0 and $m_{\rm j} = m_C = {\rm M_J}$. The inclinations simulated are $i_C = [25, 40, 55, 70, 85]°$. We place Earth at 1 au and set it in the reference plane, whereas we give jupiter a small inclination (0-5 degrees) and a small eccentricity (<0.01). This means that the Earth will have exactly the same mutual inclination w.r.t. the Companion in every realization whereas for jupiter it will vary, mostly between $2-3$ degrees.

We do four different suites of runs, with three containing different subsets of asteroid trajectories as determined in figure 4; the fourth being a retrograde version of the first:

- full – Set where the asteroid trajectories are simply drawn from the distributions described in the previous section – 100 realizations per inclination with 200 asteroids each
- kozai – Set where only such asteroids are drawn as to give Kozai oscillations, we do not do the 70 and 85 inclinations as figure 4 shows the fractions to be nearly identical to close kozai – 100 realizations with 200 asteroids each

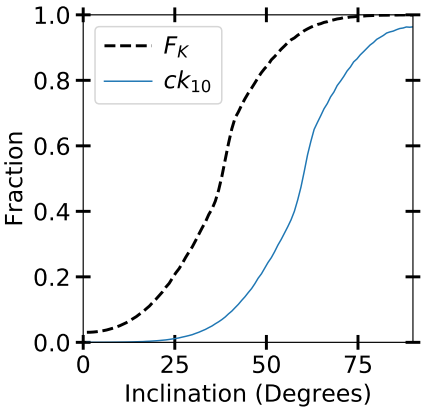

Figure 4. The black dashed line shows the fraction of test particles that can undergo Kozai cycles as a function of the inclination of the captured giant. Whereas the blue line shows the fraction of test particles that achieve a pericentre less than 10 au, i.e. the test particles that satisfy equation 11.

• close kozai – Set where only such asteroids are drawn that give large enough Kozai oscillations to cross the orbit of jupiter – 300 realizations per inclination, with 50 asteroids in the first 150 runs and 200 in the latter half of them.

• full retro – Set where we reuse the initial conditions from the full simulations with only one thing changed, we set the companion on a "mirrored" retrograde orbit. Given the broken symmetry we utilize figure 2 and define a mirrored system such that a system is mirrored if the companion on a retrograde orbit gives the same $e_{\max}$ as its prograde equivalent. The mirrored inclinations are [25,40,55,70,85] → [161,146,136,125,-]. We do not do the 85 degree retrograde run as just as in the prograde run its mirror ends up pushing the planets into the star on a short time-scale, as seen in figure 2 – 100 realizations per inclination with 200 asteroids each.

We will refer to SEjC runs as a1.n where a $\in \{f, k, ck\}$ with f for full, k for kozai and ck for close kozai, and n$\in$\{1,5\} denotes the five different inclinations. All of the simulations run for 10^8 years.

4 RESULTS

4.1 SEjC – Asteroid fates

Before even considering what happens with the asteroids we consider jupiter as it too will undergo Kozai cycles, although it should be noted that the precession from a second giant planet in the system would have blocked the cycles. We can see in figure 2 that jupiter reaches high enough eccentricities (> 0.9) to cross the orbit of the Earth for companion inclinations between 79 and 117 degrees. This means that in 32.4% of cases jupiter will reach sufficient eccentricities to cross the orbit of Earth leading to either a collision or a scattering which can either eject the Earth or send it into the Sun. We do indeed see this in the ck1.5 and f1.5 simulations but we report the behaviour of the asteroids from those simulations regardless as most of the asteroids will undergo several Kozai cycles and have time to reach their end state long before the 20-30 Myr it takes for the jupiter to increase its eccentricity and encounter the Earth.

We now consider what happens to the asteroids that are removed from the asteroid belt. Figure 5 shows a flowchart of what the asteroids do before they hit the Earth†. From left to right we see the steps each asteroid must go through before they hit the Earth with the perpendicular arrows showing how the asteroids can be removed along the way. The flow is as follows: All the asteroids start in the belt, some are then made to cross the orbit of jupiter either purely through Kozai oscillations or through Kozai and additional interactions, a subset of these asteroids end up crossing the orbit of the Earth at which point they can have close encounters with the Earth. Roughly 10% of the bodies that have close encounters end up hitting the Earth†.

There are four ways in which the asteroids are removed from the simulations: ejection, getting within 0.2 au of the star and hitting jupiter or Earth†. We can see how the likelihood of each end state varies with inclination in the ck runs as they have been selected to cross the orbit of jupiter. We show this in figure 6 by looking at CDFs, along with their one sigma error-bars. The biggest differences are seen in the number of asteroids that are removed by ejection and the number removed by getting too close to the star. At high inclinations we see a much larger fraction hitting the star, this is because at higher inclinations the Kozai cycles are faster, allowing asteroids to more easily reach sufficiently high eccentricities to be removed by the star before encountering jupiter. The reason we see more asteroids hitting the star in ck1.4 vs ck1.5 is that jupiter gets to very high eccentricities much faster in ck1.5 allowing it to clear out more asteroids before they are all gone. The spike seen in the jupiter-hits for ck1.5 is due to asteroids having smaller pericentres when encountering jupiter, giving higher ΔV making the encounters more likely to result in a collision.

4.2 SEjC – Earth impacts

To determine the number of asteroids that would actually hit the Earth we look at the number of close encounters the inflated Earth has, which are logged between 100 and 500 Earth radii. We utilize the ck runs as they have the largest number of asteroids having close encounters with the Earth. For each ck run we take the number of close encounters as a cumulative function of the closest approach (in terms of Earth radii) and fit a power law to it, as shown below:

$$F = a \times R^b. \tag{14}$$

We show the data and the fits for the ck runs in in figure 8 with the values of a and b shown in table 1.

To compare the outcomes of the runs at the different inclinations we compare the ratio between the number of expected hits for an Earth-sized body with the number of asteroids that get within 500 Earth radii. We plot these ratios for the different runs in figure 7. We see no clear trend

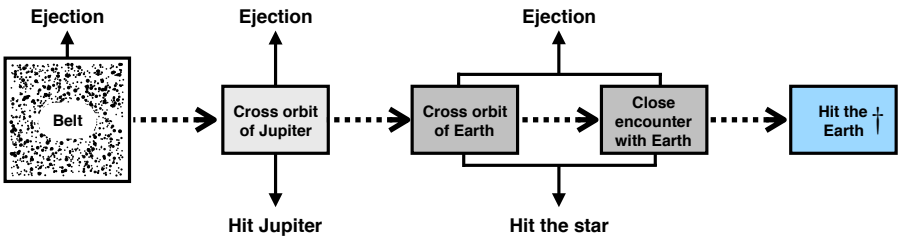

Figure 5. The steps an asteroid must go through in order to hit the earth and with the vertical lines showing the ways in which they can be removed from the simulation. In table 2 we show two ratios: The number of asteroids that go through step 3 divided by the number going through step one, and the ratio of the numbers in step 4 and step 3. Note: We will use the dagger throughout the paper with regards to hitting the Earth to remind the reader that we mean getting within 100 Earth radii.

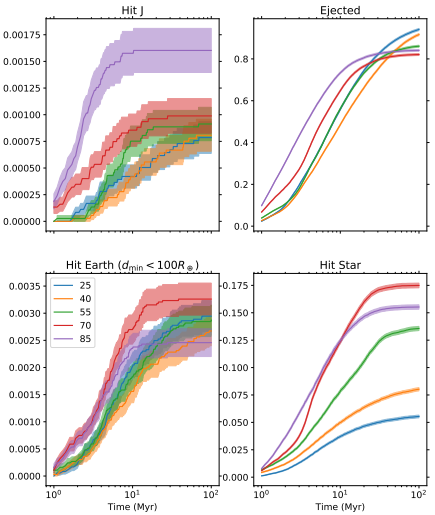

Figure 6. CDFs of the four different asteroid removal mechanisms in the ck runs. Each color represents a different inclination and the shaded area shows their respective one sigma error-bar.

with inclination and conclude that the outcomes at the different inclinations are consistent with each other.

This means that to get the fraction of asteroids in the ck runs that would hit an Earth-sized planet we can stack the data from all the ck runs and compute the fraction. We find the fraction to be $(4.0 \pm 0.5) \times 10^{-6}$. This fraction is interpreted as the fraction of asteroids removed from the asteroid belt that end up hitting the Earth. The number of impacts this corresponds to depends on what fraction of the asteroid belt a given Companion destabilises and the number of bodies in the asteroid belt, this is discussed in more detail in section 5.

Table 1. The parameter values for the fits to the close encounters using equation 14 on the ck runs

Inclination	a	b
25	0.21 ± 0.06	1.36 ± 0.05
40	0.15 ± 0.04	1.42 ± 0.05
55	0.13 ± 0.04	1.46 ± 0.05
70	0.19 ± 0.05	1.43 ± 0.04
85	0.10 ± 0.03	1.51 ± 0.05

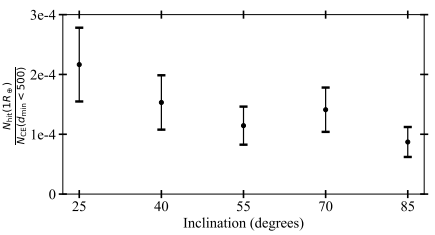

Figure 7. The number of asteroids expected to hit an Earth-sized planet in our simulations divided by the number that get within 500 Earth radii of the Earth.

4.3 SEjC – The effect of jupiter

The ck selection gives asteroids on very different initial orbits, e.g. $i_C = 25°$ gives only the asteroids with largest initial inclination to the reference plane whereas an $i_C = 85°$ will essentially select asteroid orbits randomly. The lack of correlation between the fraction of asteroids hitting the Earth with i_C implies that the asteroids that have a close encounter with jupiter and do not get ejected have their orbit changed to such a degree that their previous orbits do not matter.

This is further exemplified in table 2 where we show two fractions from each system and run. f_{ce} is the fraction of asteroids that cross the orbit of jupiter that get within 500 Earth radii of the Earth and f_{hit} is the fraction of those that get within 500 Earth radii that end up hitting the Earth†. We see in table 2 that ∼3% of asteroids crossing the orbit of jupiter have a close encounter with the Earth and that out of those ∼10% end up hitting the Earth†. This means

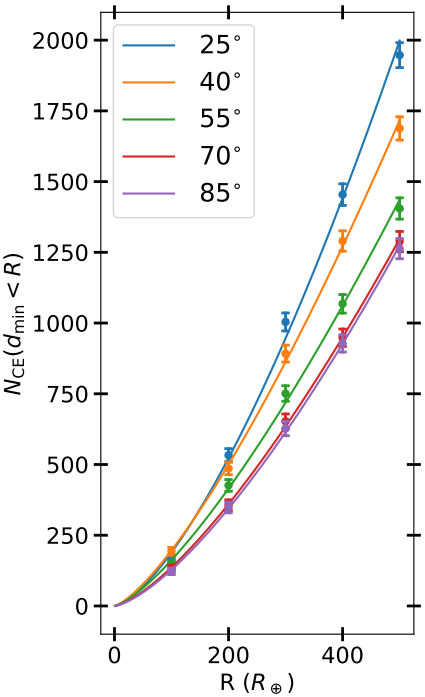

Figure 8. The number of asteroids that have an Earth–asteroid close encounters where the closest approach is less than radius R for the five different inclinations.

that 3 out of 1000 asteroids crossing the orbit of jupiter will hit the Earth† regardless of both their initial orbit and the Companion's orbit.

4.4 SEjC - Asteroid removal from belt

In table 3 we show the outcome of the asteroids in the k and f runs at two different times, 10 and 100 Myrs. We pick 10 Myr because during this time the asteroids undergo multiple cycles whereas jupiter does not have time to increase its eccentricity. If only the subset of asteroids that are simulated in the ck runs end up crossing the orbit of jupiter we would expect the fractions crossing, $f_{\rm cross} = ck_{10}$ for the full runs and $f_{\rm cross} = ck_{10}/F_K$ for the k-runs. The table show that afyer 10 Myr, the fraction of asteroids removed is mostly consistent with the number of asteroids that can cross the orbit of jupiter, whereas at later times significantly more of the asteroids have been removed.

This means that there are two processes removing asteroids from the system. The first and faster one is jupiter removing the asteroids that have their eccentricity pumped up by the Companion. The second process is a combination of asteroids being pushed to higher eccentricities through interactions with the Companion and jupiter eventually putting them on a jupiter-crossing orbit leading to their eventual removal, and asteroids being removed directly by the Companion from the belt. The latter of which can happen because the Companion encounters the asteroids at apocentre giving encounters with very low ΔV during which the Companion can do enough work to unbind the asteroids.

Table 2. $f_{\rm ce}$ and $f_{\rm hit}$ are two fractions, showing the fraction of asteroids that cross the orbit of jupiter that get within 500 Earth radii of the Earth and the fraction of those that get within 500 Earth radii that end up hitting the Earth†.
* Indicates runs where the outcome has <50 asteroids.

System	$f_{\rm ce}$	$f_{\rm hit}$
ck1.1	0.028	0.106
ck1.2	0.028	0.099
ck1.3	0.032	0.092
ck1.4	0.035	0.097
ck1.5	0.031	0.083
k1.1	0.026	0.108*
k1.2	0.032	0.088*
k1.3	0.034	0.080*
f1.1	0.030*	0.034*
f1.2	0.024	0.107*
f1.2r	0.019*	0.093*
f1.3	0.031	0.062*
f1.3r	0.031	0.076*
f1.4	0.036	0.068*
f1.4r	0.036	0.064*
f1.5	0.034	0.093

4.5 Examining longer timescales

We do an extra set of 1 Gyr simulations, in which we remove the Earth for computational efficiency, for runs f1.1, f1.2 and f1.3 to see what fraction of test particles end up being removed. Given the two processes described in the previous section we fit a double exponential to the fraction of asteroids remaining in the asteroid belt as a function of time, on the form shown below:

$$F(t) = a \times \exp\left(-\frac{t}{b}\right) + c \times \exp\left(-\frac{t}{d}\right) + g \qquad (15)$$

The three rates with their respective best fits are shown in figure 9. We see that the depletion is modeled well with the double exponential and that as expected there is one fast process and one slower process.

However, the faster decaying exponential removes a larger fraction of the asteroids than the ck subset. We take this to mean that each exponential captures the removal done by each body, rather than the aforementioned removal processes.

5 DISCUSSION

5.1 Initial impact rates

We showed in section 4.1 that 4 in 10^6 jupiter-crossing asteroids will impact the Earth. We see from table 3 that in the first 10 Myr the number of jupiter-crossing asteroids is well approximated by the ck-fraction shown as a function of

Table 3. The outcomes of the kozai and full runs. $f_{\rm expected}$ is the fraction we expect to cross the orbit of J if only the ck subset were the ones crossing. $f_{\rm cross,10}$ and $f_{\rm cross,100}$ are the fractions of asteroids that end up crossing the orbit of jupiter after 10 and 100 Myr. $f_{\rm removed}$ is the fraction of asteroids removed after 100 Myr, either by being ejected or hitting the star or planets.
Note: the output has a resolution in time of 10 kyr, i.e. if a particle crosses 10 au and is ejected within 10 kyr it will never be logged as having crossed the orbit of jupiter, resulting in an underestimation of $f_{\rm cross}$.

System	$f_{\rm expected}$	$f_{\rm cross,10}$	$f_{\rm cross,100}$	$f_{\rm removed}$
k1.1	0.05	0.06	0.20	0.24
k1.2	0.13	0.11	0.30	0.41
k1.3	0.36	0.36	0.77	0.94
f1.1	0.01	0.01	0.05	0.05
f1.2	0.09	0.08	0.23	0.27
f1.2r	0.04	0.04	0.11	0.14
f1.3	0.33	0.39	0.83	0.91
f1.3r	0.14	0.12	0.47	0.54
f1.4	0.79	0.81	0.95	1.0
f1.4r	0.33	0.38	0.84	0.95
f1.5	0.95	0.91	0.95	1.0

Companion inclination in figure 4. From Schlichting et al. (2012) we can compute the number of > 1 km sized bodies in the present day Kuiper Belt to be $\sim 10^{10}$ with models for the early evolution of the Solar System giving a primordial Kuiper belt 2000-4000 times more massive (see e.g. Gomes et al. 2005, 2018). Given these three things we can compute the average impact rate during the first 10 Myrs following the capture of the Companion. This is shown in figure 10, where we plot the CDF of the average impact rate distribution for > 1 km sized bodies using the present day Kuiper belt. The red line in the figure shows that roughly one third of captures will result in jupiter eventually ejecting the Earth, this however happens on a longer time-scale meaning that we can determine the impact rate before the orbits of the planets cross and for that reason we can include rates above the red line in the figure.

We can compare the rates we find with the inferred present-day impact rate on the Earth.. It should however be noted that the vast majority of Earth-impactors are asteroids originating in the asteroid belt and not the Kuiper belt (Strom et al. 2005). Whilst not very well constrained, the most most recent estimates give a rate of $\sim$1 per Myr for asteroids with a radius of 1 km (Wheeler & Mathias 2019). The average rate following a capture, shown in figure 10, is obviously significantly higher than 1 per Myr. Such a high impact rate would be quite harmful for life developing on Earth, as it also implies a higher impact rate for larger asteroids such as the one that wiped out the dinosaurs. And it would be even more harmful for any developing civilisation as even a km sized body can cause a period of global cooling (Toon et al. 2016) since long term climate stability is critical for the development of agriculture (Bettinger et al. 2009).

However, given that planets are pretty much exclusively captured in the birth clusters of stars the effect of this initial very high impact rate is unlikely to affect any planet hosting life. When we do consider the Sun in its birth cluster with a primordial Kuiper Belt of $20 - 40 M_{\oplus}$, the impact rate following the capture of a planet then would be in line with the rate observed for the Late Heavy Bombardment (Zahnle et al. 2003).

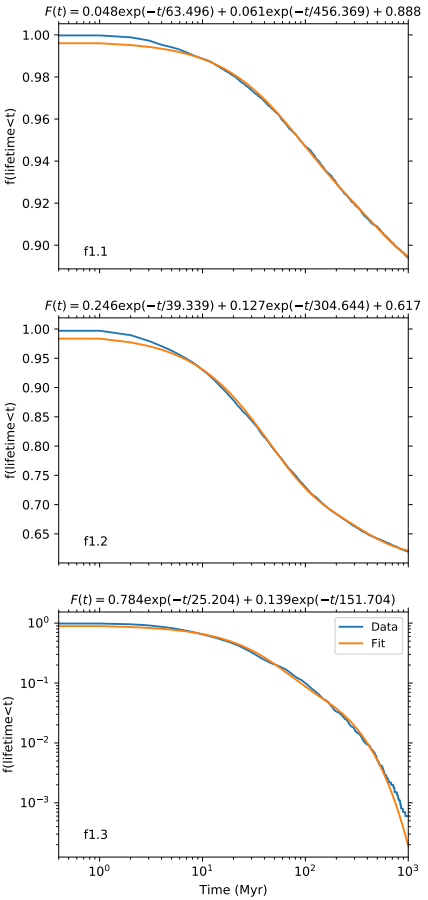

Figure 9. The fraction of asteroids remaining as a function of time for three different 1 Gyr runs with the full asteroid belt. The blue line shows the data with the best fit plotted on top of it. The values for each of the best fits is shown at the top of each panel.
Note: the y-axis changes scale (and from linear to log) between the panels

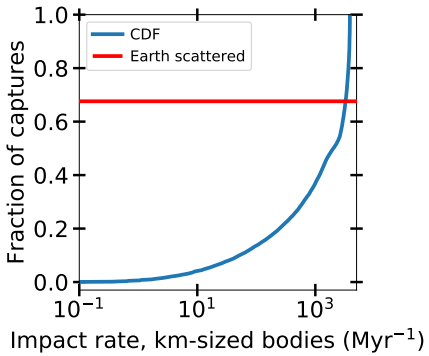

Figure 10. The blue line shows the CDF of the average number of impact per Myr of bodies greater than 1 km as a function in the first 10 Myr following the capture of a planet on isotropically distributed orbit orientations. The numbers are calculated assuming a $0.01M_\oplus$ Kuiper belt. The red line shows the fraction of outcomes in which the Earth either ends up being ejected or scattered and removed from the system.

5.2 Later impact rates

Here we consider the impact rates at later times, rather than the initial surge discussed previously. For this we look at the 1 Gyr runs of f.1-3 without the Earth. We can determine the removal rate of asteroids by differentiating the equations shown in figure 9 and estimating that out of the ones that are removed from the asteroid belt 4 in 10^6 hit the Earth.

1 Gyr after the capture, for the three different inclinations and a $0.01M_\oplus$ Kuiper belt, we find impact rates of > 1 km sized objects per Myr of: [0.60, 0.62, 0.051]. And, it takes [764, 858, 547] Myr for the flux to reach the current flux on Earth of 1 per Myr. This means that a capture on a low inclination might actually be worse for Earth than a high one (assuming it is not so high as to destabilize it). This is because, rather than a short cataclysmic period during which most of the Kuiper belt is depleted, it instead results in an increased rate over a much longer time, giving life on the planet less time to recover and develop between potential extinction events.

5.3 The companion as a transient perturber

Concerning our Solar system, using wide field infra-red data from WISE, Luhman (2014) excludes the possibility of having any planet above the mass of Saturn within 28 000 au and mass of Jupiter within 82 000 au, excluding the possibility of the Sun having a Companion such as the one we have simulated. However, as we have shown, many companions can deplete a large fraction of the the Kuiper-belt in only a few Myr. This means that most of the work could have been done whilst the Sun was still in its birth cluster. Therefore, even if the Companion is removed in a subsequent encounter a couple of Myr after capture it can already have removed a large fraction of the Kuiper Belt. In fact, Malmberg et al. (2007b) finds that stars that have a close encounter in their birth cluster, have a higher probability of having another close encounter than they initially had to have one at all. Given that a captured Companion that affects the Kuiper belt but does not leave a significant dynamical imprint on the inner planets must be on quite a wide orbit, it can be unbound rather easily in subsequent close encounters in the birth cluster. If the Companion is not removed in the birth cluster it cannot later be removed by other stars as sufficiently close encounters only occur once every 10^{11} years or so (Bailer-Jones et al. 2018), but it could have been removed by a giant molecular cloud. From Gustafsson et al. (2016) we see that the tidal field of a massive GMC ($\sim 10^6 M_\odot$) could do enough work on the planet to unbind it as the star passes through the GMC. Such encounters would occur approximately once per Gyr (Kokaia & Davies 2019).

5.4 Water delivery

It has been established by looking at isotope ratios of the Earths' water that a significant fraction of it was delivered from the outer Solar system (see e.g. Wu et al. 2018), which is in line with planet formations models because Earth being inside of the water-ice line makes it very unlikely that the water on the surface of the Earth condensed as the Earth was forming. The Earth's surface holds approximately 10^{21} kg of water, or $0.00023M_\oplus$. This corresponds to $\sim 5 \times 10^{-6}$ of the primordial Kuiper belt or $\sim 10^8$ kilometer-sized asteroids made completely of water-ice.

With jupiter on its own having a throughput of $4 \pm 0.5 \times 10^{-6}$ in the SEjC simulations, it seems unlikely that with the addition of Saturn in our Solar system that enough of the Kuiper belt would make it through to deliver a significant fraction of the water on Earth. Which also means that the water must have been delivered before most of the debris was removed from the Solar system as otherwise not enough of it could have made it past the orbits of Jupiter and Saturn.

5.5 Generalizing farther

We have interpreted that the depletion of the asteroid belt is driven by both the orbit of the jupiter as well as the companion as the depletion is well modelled by a two-component exponential. These processes are however not decoupled from each other as the interaction between belt and jupiter is driven by the Kozai cycles which the Companion induces in the belt, the time-scale and magnitude of which is set by the Companions' orbit as shown in eq. 1. The orbit of the Companion can therefore set three different depletion regimes for the asteroid belt (four if one considers planet stability separately):

(i) The Companion can orbit-cross the asteroid belt disrupting it directly.
(ii) The Companion can pump up the eccentricities of the asteroids with either the Companion itself or jupiter ejecting them later.
(iii) The Companion can pump up the eccentricities of the asteroids and then have them be removed by only jupiter.

Given these differences it becomes impossible to extend our initial semi-analytic analysis farther. To explore the outcome

of companions captured on their possible different orbits we do a suite of low resolution (1000 asteroids per run) simulations. These simulations are shown in figure 11 as black crosses with the different regimes highlighted. In these simulations we move jupiter to 5 au as it increases the precession time by a factor of 4 (equation 6) and increases the region in which the captured Companion gives Kozai oscillations; as shown by the white dashed line in figure 11. The semi-major axes and eccentricities are chosen such that there is a constant pericentre, with pericentre distances of: 50, 65, 83, 100, 125 and 150 au. For each black cross we simulate 6 different companion inclinations, 40, 55 and 70 degrees prograde and also 34, 44 and 55 degrees retrograde, which are the inclinations selected by looking at figure 2 as described in section 3. After performing the simulations we once again fit equation 15 to the depletion and differentiate it to get the removal rate, then working under the assumption that the throughput as depicted in figure 5 remains the same we can also compute the impact rates.

Figure 12 shows for how long each run results in an impact rate higher than that of the Earth. In it we see that the runs in the red regime in figure 11 give a very short enhancement as the whole belt is disrupted very quickly. As the Companion's pericentre moves outwards we see the enhancement time increasing because the depletion rate goes down. This is in part because of the increasing Kozai timescale but more than that it is that the fraction of asteroids that *can* have their orbits disrupted goes down as the Companion's pericentre increases due to moving from regime 2 to 3 which is confirmed by the decreasing number of close encounters for the Companion. We conclude that the scenario described in figure 11 is largely correct, but that the transitions are not as sharp as shown because the asteroids' semi-major axes range between [40,50] so the correct way to view it is to say that each asteroid is in a specific regime with respect to the Companion.

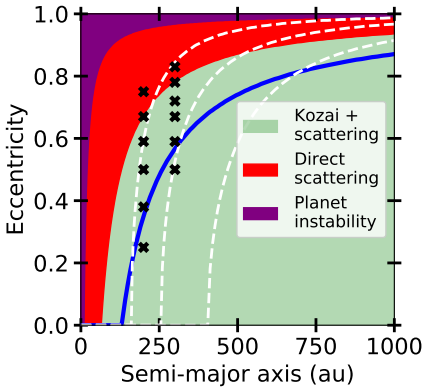

Figure 11. The different effects that are dominant for different a and e for captured planets. Planets captured in the purple region will disrupt the whole system. In the red region they will be orbit-crossing with the asteroid belt and disrupt it. In the green region asteroids need to have their eccentricities increased through Kozai oscillations in order to be scattered by either the planets in the system or the companion, where the blue line is a line of constant pericenter within which the companion can scatter the asteroids. The black crosses show where we have done 1 Gyr long simulations with a Jupiter-mass companion and a Jupiter-mass internal planet at 5 au in order to determine what fraction is depleted. The white lines show where the precession from a Jupiter-mass inner planet with a semi-major axis of (from left to right) 10, 5 and 2.5 au blocks the Kozai cycles of the asteroids.

5.5.1 *Mapping the outcome-space*

For each run we also log the mean enhancement in impact rate and use this to map the outcome-space following Companion capture. We explore the outcome-space by drawing Companions with random eccentricities and inclinations at the two semi-major axes. The eccentricity is drawn from a thermal distribution and the inclination from an isotropic distribution (Li et al. 2019). For each of the 40 000 Companions drawn we interpolate between the points in figure 12 and determine the time during which the impact rate is enhanced to be greater than the impact rate on present Earth and also the mean impact rate during this time-period.

The results of this is shown in figure 13. The first thing to note is that each panel only shows approximately 60% of the outcomes. At both semi-major axes nearly 40% (∼30% due to Companion inclination and ∼10% due to capture on high eccentricity) of captured Companions lead to the system becoming unstable.

For the remaining ∼60% the outcome is more or less evenly divided into three categories:

- High enhancement over a short period of time; companions that cross the asteroid-belt or get near it or have a high inclination but not so high as to destabilize the system.
- Moderate enhancement over a moderate amount of time; companions that have a large pericentre and a low inclination. The weak Kozai-forcing combined with their large separation means that they destabilize their "ck" asteroids over this moderate time-scale and then the depletion slows significantly.
- Low enhancement over a long time: companions that have a moderate inclination and a pericentre greater than 90 or so au. These companions can deplete most if not all of the belt given sufficient time and it results in an enhancement by a factor of 2-10 on a time-scale of hundreds of Myr to Gyrs.

We see here that the type of Companions that we concluded pose the greatest danger for life on a habitable planet when discussing the initial 1 Gyr simulations corresponding to a considerable fraction of possible Companion orbits. That is, the low inclination Companions (25 and 40 degrees but for more distant pericentres also the 50 degree) as they can produce an enhancement that persists for a much longer time.

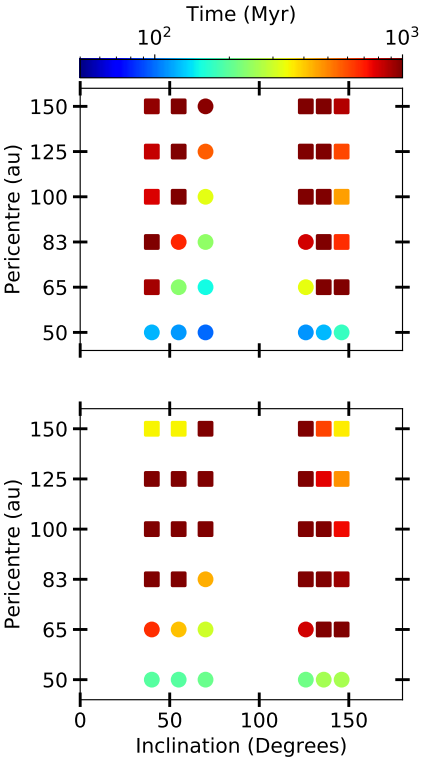

Figure 12. The figure shows for how long a captured companion produces a higher impact rate of > 1km sized objects compared to that of the present day Earth, for each cross in figure 11. For each of those crosses 6 simulations at different inclinations have been performed as shown by the markers in each panel. The square marker indicates that there were asteroids remaining at the end of the run, whereas the circles show runs where all the asteroids were removed. Marker color shows the time until the Earth rate is reached after capture, with 1 Gyr set as an upper limit.
Top panel shows runs with $a = 200$ au and bottom shows runs with $a = 300$ au.

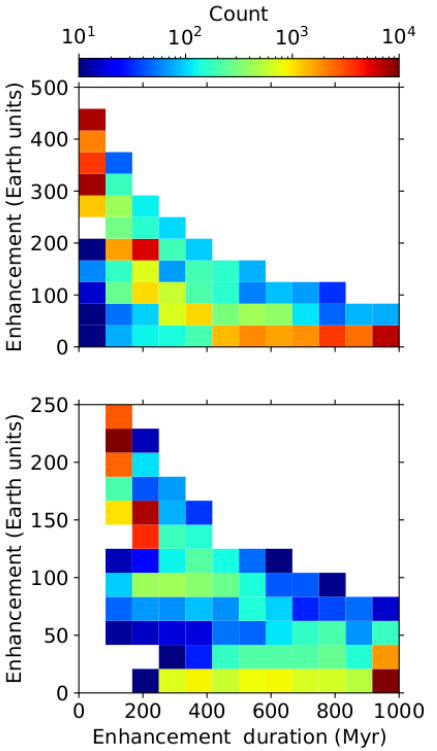

Figure 13. The outcome space of enhancement duration and corresponding mean enhancement for captured companions with semi-major axis of 200 (top) and 300 (bottom). The color shows what number out of the 40 000 random Companions drawn give an outcome in each bin. The figure is generated by drawing eccentricities from a thermal distribution and inclinations from an isotropic distribution and then interpolating in figure 12.

6 CONCLUSIONS

Using a simple model of a planetary system with a planet in its habitable zone, we have studied the impact that capturing a planet on a wide, inclined orbit would have on the habitability of the system by considering the delivery of impactors. From this simple model we then generalized further and considered the possible outcomes of capturing planets. Our key findings are:

- We show that due to the planetary system not being in the test particle limit, the Kozai-oscillations deviate somewhat from the analytic description of the problem (Innanen et al. 1997), as we can see in figure 2. Regardless, we use the theory to determine the fraction of asteroids that cross the orbit of jupiter (figure 3) and show that this is a valid approximation for what happens in the first 10 Myr of the system, for all Companion inclinations; as shown in table 3.
- For the SEjC system (Sun+Earth+Jupiter-mass planet at 10 au + Jupiter-mass Companion at 100 au) we find that for all inclinations roughly 4 out of 10^6 asteroids that are destabilized will hit the Earth (figures 7 and 8), which when considering the current Kuiper belt is equivalent to $\sim 10^4$ km-sized impacts.
- On a 10 Myr time-scale after capture we see very high impact rates for the Earth from the highly inclined captures, thousands of times higher than the present rate (figure 10).

A Companion that was captured in a close encounter in the Sun's birth cluster and unbound by a later encounter could have produced an impact rate equivalent to the Late Heavy Bombardment in the early stages of the Solar system.

- For habitable planets Companions captured on low inclination orbits have worse consequences, as it can give an enhanced impact rate for several Gyr (figure 12), rather than the short cataclysmic event produced by highly inclined captured companion.
- Inclined captured companions are very effective at clearing out the asteroid belt, with Companions that have an inclination greater than 55 degrees (∼60% of an isotropic distribution) and pericentre less than 100 au eventually clearing out the whole belt. This is contingent on the precession from the inner planets on the belt being slower than the Kozai oscillations (compare fig 11 and 12)
- With $e \sim 0.7$ for captured planets as it follows a thermal distribution (see e.g. Li et al. 2019) the pericentres will likely often be small and captured planets will often remove a large fraction of the belts.
- We find that the time-scales on which the belt is cleared out can vary from a couple of tens of Myr to Gyrs (figures 12 and 9).

ACKNOWLEDGMENTS

The authors are supported by the project grant 2014.0017 "IMPACT" from the Knut and Alice Wallenberg Foundation. AJM acknowledges support from the Swedish Research Council (starting grant 2017-04945) and from the Swedish National Space Agency (career grant 120/19C). The computations were enabled by resources provided by the Swedish National Infrastructure for Computing (SNIC) at LUNARC partially funded by the Swedish Research Council through grant agreement no. 2016-07213.

DATA AVAILABILITY

The data underlying this article will be shared on reasonable request to the corresponding author

REFERENCES

Agnew M. T., Maddison S. T., Horner J., 2018, MNRAS, 477, 3646
Antognini J. M. O., 2015, MNRAS, 452, 3610
Bailer-Jones C. A. L., Rybizki J., Andrae R., Fouesneau M., 2018, A&A, 616, A37
Batygin K., Brown M. E., 2016, AJ, 151, 22
Bettinger R., Richerson P., Boyd R., 2009, Current Anthropology, 50, 627
Bitsch B., Izidoro A., Johansen A., Raymond S. N., Morbidelli A., Lambrechts M., Jacobson S. A., 2019, A&A, 623, A88
Brown M. E., Batygin K., 2016, ApJ, 824, L23
Carrera D., Davies M. B., Johansen A., 2016, MNRAS, 463, 3226
Chambers J. E., 1999, MNRAS, 304, 793
Denham P., Naoz S., Hoang B.-M., Stephan A. P., Farr W. M., 2019, MNRAS, 482, 4146
Dias W. S., Alessi B. S., Moitinho A., Lépine J. R. D., 2002, A&A, 389, 871
Gaia Collaboration et al., 2018, Astronomy and Astrophysics, 616, A1
Georgakarakos N., Eggl S., Dobbs-Dixon I., 2018, ApJ, 856, 155
Gieles M., Lamers H. J. G. L. M., Portegies Zwart S. F., 2007, ApJ, 668, 268
Gomes R., Levison H. F., Tsiganis K., Morbidelli A., 2005, Nature, 435, 466
Gomes R., Nesvorný D., Morbidelli A., Deienno R., Nogueira E., 2018, Icarus, 306, 319
Gustafsson B., Church R. P., Davies M. B., Rickman H., 2016, A&A, 593, A85
Innanen K. A., Zheng J. Q., Mikkola S., Valtonen M. J., 1997, AJ, 113, 1915
Jones B. W., Sleep P. N., Chambers J. E., 2001, A&A, 366, 254
Kaib N. A., Raymond S. N., Duncan M. J., 2011, ApJ, 742, L24
Katz B., Dong S., Malhotra R., 2011, Phys. Rev. Lett., 107, 181101
Kokaia G., Davies M. B., 2019, MNRAS, 489, 5165
Kokaia G., Davies M. B., Mustill A. J., 2020, MNRAS, 492, 352
Kozai Y., 1962, AJ, 67, 591
Lada C. J., Lada E. A., 2003, ARA&A, 41, 57
Lamers H. J. G. L. M., Gieles M., Bastian N., Baumgardt H., Kharchenko N. V., Portegies Zwart S., 2005, A&A, 441, 117
Li D., Mustill A. J., Davies M. B., 2019, MNRAS, 488, 1366
Lidov M. L., 1962, Planet. Space Sci., 9, 719
Luhman K. L., 2014, ApJ, 781, 4
Machida M. N., Kokubo E., Inutsuka S.-I., Matsumoto T., 2010, MNRAS, 405, 1227
Malmberg D., Davies M. B., Chambers J. E., 2007a, MNRAS, 377, L1
Malmberg D., de Angeli F., Davies M. B., Church R. P., Mackey D., Wilkinson M. I., 2007b, MNRAS, 378, 1207
Malmberg D., Davies M. B., Heggie D. C., 2011, MNRAS, 411, 859
Matsumura S., Ida S., Nagasawa M., 2013, ApJ, 767, 129
Menou K., Tabachnik S., 2003, ApJ, 583, 473
Montesinos B., et al., 2016, A&A, 593, A51
Murray C. D., Dermott S. F., 1999, Solar system dynamics
Mustill A. J., Raymond S. N., Davies M. B., 2016, MNRAS, 460, L109
Mustill A. J., Davies M. B., Johansen A., 2017, MNRAS, 468, 3000
Naoz S., Farr W. M., Lithwick Y., Rasio F. A., Teyssandier J., 2013a, MNRAS, 431, 2155
Naoz S., Yoshida N., Gnedin N. Y., 2013b, ApJ, 763, 27
Piso A.-M. A., Youdin A. N., 2014, ApJ, 786, 21
Piso A.-M. A., Youdin A. N., Murray-Clay R. A., 2015, ApJ, 800, 82
Schlichting H. E., et al., 2012, ApJ, 761, 150
Sibthorpe B., Kennedy G. M., Wyatt M. C., Lestrade J. F., Greaves J. S., Matthews B. C., Duchêne G., 2018, MNRAS, 475, 3046
Strom R. G., Malhotra R., Ito T., Yoshida F., Kring D. A., 2005, Science, 309, 1847
Toon O. B., Bardeen C., Garcia R., 2016, Atmospheric Chemistry & Physics, 16, 13185
Valtonen M., Karttunen H., 2006, The Three-Body Problem. Cambridge University Press
Volk K., Malhotra R., 2011, ApJ, 736, 11
Wheeler L. F., Mathias D. L., 2019, Icarus, 321, 767
Wu J., Desch S. J., Schaefer L., Elkins-Tanton L. T., Pahlevan K., Buseck P. R., 2018, Journal of Geophysical Research (Planets), 123, 2691
Zahnle K., Schenk P., Levison H., Dones L., 2003, Icarus, 163, 263